

5-1-2019

## Cesium Platinum Iodide Perovskite Synthesis, Development and Application in Photovoltaic Devices

Dakota Schwartz  
dcschwar@gmail.com

Follow this and additional works at: <https://digitalscholarship.unlv.edu/thesesdissertations>



Part of the [Engineering Science and Materials Commons](#), and the [Materials Science and Engineering Commons](#)

---

### Repository Citation

Schwartz, Dakota, "Cesium Platinum Iodide Perovskite Synthesis, Development and Application in Photovoltaic Devices" (2019). *UNLV Theses, Dissertations, Professional Papers, and Capstones*. 3671. <https://digitalscholarship.unlv.edu/thesesdissertations/3671>

This Thesis is protected by copyright and/or related rights. It has been brought to you by Digital Scholarship@UNLV with permission from the rights-holder(s). You are free to use this Thesis in any way that is permitted by the copyright and related rights legislation that applies to your use. For other uses you need to obtain permission from the rights-holder(s) directly, unless additional rights are indicated by a Creative Commons license in the record and/or on the work itself.

This Thesis has been accepted for inclusion in UNLV Theses, Dissertations, Professional Papers, and Capstones by an authorized administrator of Digital Scholarship@UNLV. For more information, please contact [digitalscholarship@unlv.edu](mailto:digitalscholarship@unlv.edu).

CESIUM PLATINUM IODIDE PEROVSKITE SYNTHESIS, DEVELOPMENT AND APPLICATION IN  
PHOTOVOLTAIC DEVICES

By

Dakota C. Schwartz

Bachelor of Science – Mechanical Engineering  
California Polytechnic State University, San Luis Obispo

A thesis submitted in partial fulfillment  
of the requirement for the

Master of Science in Engineering - Mechanical Engineering

Department of Mechanical Engineering  
Howard R. Hughes College of Engineering  
The Graduate College

University of Nevada, Las Vegas  
May 2019

Copyright by Dakota Schwartz

All Rights Reserved



## Thesis Approval

The Graduate College  
The University of Nevada, Las Vegas

April 12, 2019

This thesis prepared by

Dakota C. Schwartz

entitled

Cesium Platinum Iodide Perovskite Synthesis, Development and Application in  
Photovoltaic Devices

is approved in partial fulfillment of the requirements for the degree of

Master of Science in Engineering - Mechanical Engineering  
Department of Mechanical Engineering

Shubhra Bansal, Ph.D.  
*Examination Committee Chair*

Kathryn Hausbeck Korgan, Ph.D.  
*Graduate College Dean*

Hui Zhao, Ph.D.  
*Examination Committee Member*

Thomas Hartmann, Ph.D.  
*Examination Committee Member*

Clemens Heske, Ph.D.  
*Graduate College Faculty Representative*

# ABSTRACT

## CESIUM PLATINUM IODIDE PEROVSKITE SYNTHESIS, DEVELOPMENT AND APPLICATION IN PHOTOVOLTAIC DEVICES

By

Dakota Schwartz

Dr. Shubhra Bansal, Committee Chair  
Assistant Professor of Mechanical Engineering,  
University of Nevada, Las Vegas

Third generation photovoltaics, including perovskites, are essential to improving solar technology for widespread future use. Perovskite solar cells have surpassed 23.7% power conversion efficiency, comparable to traditional silicon photovoltaic panels. However, these perovskites are fabricated using lead-based compounds, posing toxicity issues. Furthermore, existing perovskites have limited thermal and moisture stability in ambient environments. In order to address toxicity and stability concerns, as well as to maximize photon absorption in solar cells through bandgap optimization, this effort focuses on the development of novel lead-free perovskite materials. A cesium platinum iodide composition is selected as a model system due to the theoretical stability and oxidation resistance of platinum.  $\text{CsPtI}_3$  is expected to be metallic, however, 2D perovskite variant  $\text{Cs}_2\text{PtI}_6$  offers promising properties of high absorption coefficient, with high carrier mobility and minority carrier lifetimes. Future work for this

research includes demonstration of bandgap tunability with halide/chalcogen substitution for X anion, optimization of perovskite and charge transport layers, and exploration of Pt replacement with less expensive d-transition elements.

A solution-based process is used to fabricate thin-film samples with variables including solutes, solvents, and solution deposition techniques. Two types of cesium platinum iodide perovskite material have been synthesized with the platinum containing solute as primary process variant. Films prepared from platinum tetra-iodide and cesium iodide are majority  $\text{Cs}_2\text{PtI}_6$  phase with a bandgap of around 1.4 eV and minority carrier lifetime  $\sim 2.7 \mu\text{s}$ . Films composed from platinum di-iodide and cesium iodide consistently have a bandgap of around 1.8-2.0 eV and minority carrier lifetime  $\sim 62 \text{ ns}$ . Both material types also show high absorption coefficient  $> 10^5 \text{ cm}^{-1}$ . Devices fabricated from both material variations show definite diode behavior but no conclusive photo response and need further research. Detail on material synthesis, material characterization, film properties, device functionality, challenges, and commentary of the cost and future study of  $\text{Cs}_2\text{PtI}_6$  and perovskite derived from the  $\text{Cs}_2\text{PtI}_6$  model structure is provided.

## ACKNOWLEDGEMENTS

This experience has helped me recognize and appreciate the expertise and patience of UNLV's academic community as well as the love and endless support of my friends and family. Thank you to everyone who made this possible, particularly Daniel, my parents, and my maternal and paternal grandparents.

I would like to share my appreciation for Dr. Shubrha Bansal, my faculty adviser and thesis committee chair, for her guidance, support and encouragement during my research and thesis writing process. Dr. Bansal is a dedicated professional with endless motivation and enthusiasm for the field of photovoltaics and materials science; I am grateful for the knowledge she has shared with me and the opportunities she has provided for me. This project would not have been possible without her guidance and mentorship.

I would also like to thank my thesis committee members, Dr. Thomas Hartmann, Dr. Hui Zhao and Dr. Clemens Heske, for taking the time to support my efforts, provide critical feedback, and lookout for my well-being for the duration of this project. I am so grateful for the time and patience of the many UNLV faculty members and graduate students, including Thomas Hartman, Mingua Ren, Dan Koury, Andrew Swift and Curtis Walkons who taught me how to use many of the analysis methods in this effort. A number of people from outside UNLV were crucial to providing materials, completing testing, and understanding results including Benedikt Ursprung (PL/TRPL measurements), Ivano Castelli (first principle calculations), Sina Soltanmohammad (SIMS and Raman measurements), Jim Sites and Ramesh Pandey (CdS-Coated Tec10 substrates), and David Albin (carbon paste).

Additional thanks are in order to all the members of Dr. Bansal's research group including Vanesa, who was of immense help for the duration of this process, and Rubaiya, Mohsen, and Curtis who gave invaluable content and presentation recommendations. Thank you to all who assisted with this effort.



## DEDICATION

To my grandma, Diane Schwartz

A woman whose deep thought, Ph. D. in Applied Mathematics and appreciation of literature  
continue to make anything possible.

## TABLE OF CONTENTS

ABSTRACT .....	iii
ACKNOWLEDGEMENTS .....	v
DEDICATION .....	vii
LIST OF TABLES .....	xi
LIST OF FIGURES .....	xiii
LIST OF EQUATIONS.....	xix
CHAPTER 1: INTRODUCTION.....	1
1.1 Background .....	1
1.2 Methodology.....	8
CHAPTER 2: RESULTS AND ANALYSIS.....	33
2.1 Platinum Tetra Iodide and Cesium Iodide Derived Perovskite Synthesis.....	33
2.2 Platinum Di-iodide and Cesium Platinum Iodide Derived Perovskites Synthesis...	52
2.3 Cesium Platinum Iodide Photovoltaic Device Fabrication and Performance .....	76
CHAPTER 3: LABORATORY FABRICATION COSTS OF LEAD AND LEAD FREE PEROVSKITES.....	90
3.1 Costs Associated with Solute Used .....	91
3.2 Costs Associated with Solvent Used .....	96

3.3	Total Costs Associated with Solution Preparation .....	99
3.4	Practical Applications of Cost Analysis.....	100
CHAPTER 4: CONCLUSIONS AND FUTURE RESEARCH .....		104
4.1	Conclusions .....	104
4.2	Future Research .....	108
APPENDIX A: TESTING AND ANALYSIS PROCEDURES .....		110
A.1	UV-Visible Light Testing and Analysis Procedure .....	110
A.2	Powder X-Ray Diffraction Testing and Analysis Procedure .....	113
A.3	Scanning Electron Microscopy Testing and Analysis Procedure .....	116
A.4	Energy Dispersive Spectroscopy.....	118
A.5	Current-Voltage Testing and Analysis Procedure .....	119
APPENDIX B: MOLARITY CALCULATIONS.....		125
B.1	Version 1: Cs <sub>2</sub> PtI <sub>6</sub> with PtI <sub>4</sub> and CsI.....	125
B.2	Version 2: Cs <sub>2</sub> PtI <sub>6</sub> with PtI <sub>2</sub> and CsI.....	126
APPENDIX C: POWDER XRD TOPAS REPORTS .....		129

C.1 Powder XRD Pattern for cesium platinum iodide derived from solution processed PtI <sub>4</sub> and CsI.....	129
C.2 Powder XRD Pattern for cesium platinum iodide derived from solution processed PtI <sub>2</sub> and CsI.....	132
C.3 Powder XRD Pattern for spin coated cesium platinum iodide derived from solution processed PtI <sub>2</sub> and CsI.....	135
APPENDIX D: RAW EDS DATA.....	139
APPENDIX E: SOLUTE COSTS.....	143
REFERENCES .....	144
CURRICULUM VITAE.....	148

## LIST OF TABLES

Table 1: Summary of solutes and solvents used in the cesium platinum iodide solution processing process. ....	9
Table 2: Equipment used for materials characterization and device testing. ....	18
Table 3: Statistics for four samples from different batches indicate low variation with a standard deviation of under 0.02 eV between measurements. ....	39
Table 4: Chemistry data from EDS testing methods computed using INCA software for PtI <sub>4</sub> +CsI material. No chlorine source was present during processing or storage and may be an error. ...	45
Table 5: Statistics for four samples from different batches indicate some variation with a standard deviation of under 0.04 eV between measurements. ....	58
Table 6: Chemistry data from EDS testing methods computed using INCA software for PtI <sub>2</sub> +CsI material. ....	66
Table 7: EDS data from the sample pictures in Figure 28. The cubic crystal information corresponds to site B, while the dendritic information corresponds to site C. ....	70
Table 8: Device type summary with layer composition. ....	77
Table 9: Device diode factor, series resistance, shunt resistance, and diode current density estimates. ....	78
Table 10: Published molecular mass and density, as used to calculate the resulting moles of perovskite product per cubic centimeter. The required mMol refers to the moles of product perovskite in a cubic centimeter. ....	92
Table 11: Ideal chemical formulas for perovskites. ....	93

Table 12: Amount of solutes required to produce 1 cubic centimeter of perovskite product.  
Conversion between moles and grams of solutes and solute cost can be found in Appendix E. 94

Table 13: Common perovskite processing solvents with cost information from Sigma–Aldrich.  
Cost is highly dependent on amount. Costs were selected using purchase prices for as close to 1 liter as possible. GBL is a List 1 controlled chemical in the United States and similarly regulated in many countries; it can be less convenient and timely to obtain larger volumes resulting in higher costs than the cost used in this analysis. .... 97

Table 14: Thickness and cost ratios of MAPbI<sub>3</sub> to cesium platinum iodide perovskites..... 103

Table 15: Solute costs as used in Chapter 3. Determined February 2019. .... 143

## LIST OF FIGURES

Figure 1: Computational estimates of cubic and tetragonal bandgaps with the likelihood of perovskite formation presented using the prediction method reported in Science Advances in February 2019 [35]. This method is reported to be 91% accurate for iodide perovskites [35]. .....	5
Figure 2: Crystal structure of cubic (a) CsGeI <sub>3</sub> and (b) Cs <sub>2</sub> PtI <sub>6</sub> generated using ICDD entry number 04-90-6679 and 04-01101068 respectively. No computational patterns are available for CsPtI <sub>3</sub> .....	7
Figure 3: The following element to color associations are oxygen-red, carbon - black, nitrogen - blue, hydrogen -white and sulfur-yellow. A) DMF molecule B) DMSO molecule C) GBL molecule. Images generated in Accelrys DS Visualizer. Ben Mills, public domain. ....	11
Figure 4: Solution processing summary for cesium platinum iodide films in atmospheric conditions.....	13
Figure 5: Nitrogen filled glovebox used for sample storage.....	16
Figure 6: (a) Shimadzu UV-2600 UV-Vis Spectrometer used for UV-Vis measurements. (b) Schematic of UV/Vis/NIR spectrophotometer, optical mirrors. Image credit: UV-2600 operating manual [40]. ....	20
Figure 7: Spectrometer interior with the Transmittance clip labeled “T” and the reflectance holder labeled “R”. ....	22
Figure 8: A) D8 Bruker X-Ray Diffractometer located in SEB 1138. ....	24
Figure 9: JEOL scanning electron microscope model JSM-5610. Image provided by the UNLV Department of Geoscience website ( <a href="http://emil.sites.unlv.edu/sem.htm">http://emil.sites.unlv.edu/sem.htm</a> ). ....	27
Figure 10: A) The ABET silicon calibration cell used to calibrate the solar simulator prior to each test run. B) The Keithley SourceMeter used to apply voltage and measure current output. C) The Abet Solar Simulator used to supply light to test devices for light JV testing. ....	29

Figure 11: An example of an annealed film composed of  $\text{PbI}_2$  and CsI solutes dissolved in DMF/DMSO solvents. The resulting layer is black in color..... 34

Figure 12: Measured transmittance and reflectance with calculated absorbance taken using UV-Vis spectroscopy for  $\text{PbI}_2$  and CsI derived perovskite..... 35

Figure 13: Absorption coefficient for perovskite derived from  $\text{PbI}_2$  and CsI for light with wavelengths ranging from 300 nm to 1400 nm..... 36

Figure 14: Tauc plot of film samples composed of  $\text{PbI}_2$  and CsI solution processed perovskite with A) the indirect Tauc plot and the B) direct Tauc plot. The dotted line indicates the Tauc plot slope change; the x-axis intercept is the estimated bandgap. .... 38

Figure 15: Photoluminescence measurements completed at Berkeley Lab’s Molecular Foundry. The orange curve is the film of interest, synthesized using  $\text{PbI}_2$  and CsI solutes; the peak at corresponding to 1.4 eV indicates a bandgap near to this value. The blue curve is a separate sample discussed in a different section..... 40

Figure 16: Time-resolved photoluminescence measurements indicating the minority carrier lifetime for the  $2\text{CsI}/\text{PbI}_2$  material. Source of data anomaly at 450 ns remains unknown. .... 41

Figure 17: Powder XRD pattern for a solution processed sample containing  $\text{PbI}_2$  and CsI solutes with DMF/DMSO solvents. The y-axis of both plots is the square root of intensity to allow smaller peaks to be visible. A) A plot of two raw sample patterns with  $\text{Cs}_2\text{PbI}_6$  hkl’s provided in the callouts. Peaks without callouts are not  $\text{Cs}_2\text{PbI}_6$  phase. B) A plot showing a computational refinement done using Topas..... 44

Figure 18: The formation of cubic grains up to 20  $\mu\text{m}$  can be found in  $\text{Cs}_2\text{PbI}_6$  films. The films pictured were deposited using a doctor blade method and annealed for 1 hour at 100°C. Some artifacts of charging by the electron beam are present in the image. A) A top down image of the surface with grain sizes of around 2  $\mu\text{m}$  to 20  $\mu\text{m}$ . B) A cross section of the same sample with similar grain sizes. .... 48



Figure 19: DSC measurements from a 27.3 mg  $\text{PbI}_2$  CsI sample measured at 10K/min up to 600°C using an  $\text{Al}_2\text{O}_3$  sample holder. The sample holder was heated to 1200°C to clean and a baseline correction with identical parameters was completed prior to the measurement. .... 50

Figure 20: An example of an annealed film composed of  $\text{PbI}_2$  CsI solutes dissolved in DMF/DMSO solvents. The resulting layer is red in color and adhered well to the substrate. .... 53

Figure 21: Measured transmittance and reflectance with calculated absorbance taken using UV-Vis spectroscopy for  $\text{PbI}_2$  and CsI derived perovskite. .... 54

Figure 22: Absorbance coefficient for Perovskite derived from  $\text{PbI}_2$  and CsI for light with wavelengths ranging from 300 nm to 1400 nm. .... 55

Figure 23: Tauc plot of  $\text{PbI}_2$  and CsI solution processed perovskite assuming a direct bandgap. The dotted line indicates the Tauc plot slope change; the x-axis intercept is the estimated bandgap. .... 57

Figure 24: Photoluminescence measurements completed at Berkeley Lab’s Molecular Foundry. The blue curve is the film of interest, synthesized using  $\text{PbI}_2$  and CsI solutes; the peak at corresponding to 1.9 eV indicates a bandgap near to this value. The orange curve is a separate sample discussed in a different section. This figure is identical to Figure 15. .... 59

Figure 25: Time-resolved photoluminescence measurements indicating the minority carrier lifetime for the  $2\text{CsI}+2\text{PbI}_2$  material. Source of data anomaly at 42 ns is unknown. .... 60

Figure 26: Powder x-ray diffraction from a sample composed of  $\text{PbI}_2$  and CsI in a DMF/DMSO solution. A) A typical  $\text{PbI}_2$ +CsI pattern fit in Topas with cubic and tetragonal computational patterns. B) Two separate  $\text{PbI}_2$ +CsI sample patterns with cubic and tetragonal computational patterns. .... 64

Figure 27: SEM images of a  $\text{PtI}_2 + \text{CsI}$  sample at various magnifications. A) Uneven surface at 1000X, B) Depicts a 50  $\mu\text{m}$  sample cross section. Note two distinct layers are present with grain growth visible on the superstrate surface. C) Uneven surface at 7000X. .... 67

Figure 28: Backscatter images depicting morphology including crystal formation in  $\text{PtI}_2 + \text{CsI}$  perovskite materials. A) A crystal at the lowest SEM magnification. This is visible to the human eye. B) Steps form on the crystal surface. C) The area of the film around the crystal has a dendritic structure and different chemistry. .... 69

Figure 29: The color difference between a doctor blade sample (thicker) and a spin coated sample (thinner). These are real samples images taken with a phone camera. .... 71

Figure 30: SEM images of a  $\text{PtI}_2 + \text{CsI}$  sample deposited using spin coating methods. .... 72

Figure 31: Spin coated  $\text{PtI}_2 \text{CsI}$  films have an increased bandgap from blade processed films. This figure shows a blade processed film with a bandgap of 2.1 eV and a spin coated film with an increased bandgap of 2.6 eV using Tauc methods to determine the bandgap. .... 72

Figure 32: A comparison of powder XRD patterns for blade processed and spin coated samples. .... 73

Figure 33: Device layers, not to scale. \*not present in all devices. .... 77

Figure 34: Dark current voltage measurements for a device fabricated with a  $\text{Cs}_2\text{PtI}_6$  absorber layer (from  $\text{PtI}_4$  and  $\text{CsI}$ ) on a FTO coated superstrate. The resulting curve indicates diode behavior with a current of  $12 \mu\text{A}\cdot\text{cm}^{-2}$  at 2.0 V. .... 79

Figure 35: Dark current voltage measurements for a device fabricated with a  $\text{Cs}_2\text{PtI}_6$  absorber layer (from  $\text{PtI}_4$  and  $\text{CsI}$ ) on a Cods and FTO coated superstrate. The resulting curve indicates diode behavior with a current of  $1.2 \mu\text{A}\cdot\text{cm}^{-2}$  at 2.0 V. .... 81

Figure 36: Dark current voltage measurements for a device fabricated with a Cs<sub>2</sub>PtI<sub>6</sub> absorber layer (from PtI<sub>4</sub> and CsI) on a FTO coated superstrate. The resulting curve indicates only resistive behavior with a current of 1.5 mA\*cm<sup>-2</sup> at 2.0 V. .... 82

Figure 37: Dark current voltage measurements for a device fabricated with a Cs<sub>2</sub>PtI<sub>6</sub> absorber layer (from PtI<sub>4</sub> and CsI) on a FTO coated superstrate. The resulting curve indicates diode behavior with a current of 1.8 mA\*cm<sup>-2</sup> at 2.0 V..... 83

Figure 38: Dark current voltage measurements for a device fabricated with a Cs<sub>2</sub>PtI<sub>6</sub> absorber layer (from PtI<sub>4</sub> and CsI) on a FTO coated superstrate. The resulting curve indicates diode behavior with a current of 3.6 μA\*cm<sup>-2</sup> at 2.0 V..... 84

Figure 39: Dark current voltage measurements for a device fabricated with a Cs<sub>2</sub>PtI<sub>6</sub> absorber layer (from PtI<sub>4</sub> and CsI) on a FTO coated superstrate. The resulting curve indicates only resistive behavior with a current of 1.5 mA\*cm<sup>-2</sup> at 2.0 V. .... 85

Figure 40: Indicates the cost, in USD, of a cubic centimeter of product and the cost of a 1 cm<sup>2</sup>, 1 μm thick perovskite layer. The B-cation containing solute is much more expensive than the A-cation containing solute and is the main contributor to the total cost, with the exception of MAI. .... 95

Figure 41: A) Cost of solvent dependent on molarity for various solvents and B) Proportion of solvent contributions to the total solution materials cost. Solutions with less expensive solutes, such as MAPbI<sub>3</sub> and Cs<sub>2</sub>TeI<sub>6</sub> have slightly higher proportional costs, but the overall costs for solvents for all perovskite materials will be very similar..... 98

Figure 42: Total solution cost comparison. All solutions are assumed to be 0.5M; deviations in molarity will have a small effect on the overall cost for the solvents used in this analysis. A) Shows the estimated cost for a single cm<sup>2</sup>by 1 micron perovskite layer and the cost by cubic centimeter for each perovskite material. B) Shows the costs of each perovskite material as a

proportion of traditional lead-based MAPbI<sub>3</sub> perovskites, further indicated at 1.0 but the dotted line..... 99

Figure 43: Absorbance coefficients determined experimentally from MAPbI<sub>3</sub> (Ju, 2018) and from cesium platinum iodide perovskites created in lab. .... 102

Figure 44: Energy Dispersive X-Ray Spectroscopy (EDS) raw data INCA report for PTI<sub>4</sub>+CsI film sample. Sample number 144. No Peaks omitted. .... 139

Figure 45: Energy Dispersive X-Ray Spectroscopy (EDS) raw data INCA report for PTI<sub>2</sub>+CsI film sample. Sample number 121. No Peaks omitted. .... 140

Figure 46: Energy Dispersive X-Ray Spectroscopy (EDS) raw data INCA report for PTI<sub>2</sub>+CsI film sample with crystal (on crystal). Sample number 189. No Peaks omitted..... 141

Figure 47: Energy Dispersive X-Ray Spectroscopy (EDS) raw data INCA report for PTI<sub>2</sub>+CsI film sample with crystal (off crystal). Sample number 189. No Peaks omitted. .... 142

## LIST OF EQUATIONS

Equation 1: A tolerance factor proposed by Bartel et al. [35]. A factor of under 4.18 is predictive of perovskite formation with a reported 92% for all perovskite types.....	4
Equation 2: Ideal reactions for cesium platinum iodide perovskites using two solute combinations.....	9
Equation 3: Intensity of radiation. ....	21
Equation 4: Relation of transmission, reflection and absorption. ....	21
Equation 5: Relation of transmission, reflectance and absorption for high absorption materials. ....	21
Equation 6: Bragg law for 1 <sup>st</sup> order diffraction.....	25
Equation 7: General quadratic form for a cubic system of Bragg law for the relation between the diffraction angle, lattice planes and the lattice parameter. ....	25
Equation 8: The Skoplanki model is one of many models used to determine cell temperature. It is relatively simple and accounts for irradiance, ambient temperature and wind speed. This model is used to demonstrate the difference between cell temperature and ambient temperature.....	49
Equation 9: Moles of perovskite by volume as a function of density and molar mass.....	91
Equation 10: The solvent cost depends upon the volume of solvent used and the cost of the solvent. The volume required is dependent upon the molarity and amount of solute used.....	98
Equation 11: The ratio of absorbance coefficients (denoted by $\alpha$ ) will be related to the ratio of material thickness (denoted by $x$ ) for the same intensity ratio.....	101

Equation 12: Assuming no losses, light is absorbed, transmitted and/or reflected as it encounters a new medium. ....	112
Equation 13: Relation of normalized transmittance and normalized absorbance assuming no losses and identical surface interfaces.....	112
Equation 14: Absorbance coefficient assuming no losses and identical surface interfaces. ....	112
Equation 15: Tauc equation, developed in 1968 by J. Tauc for determining the bandgaps of semiconductor materials. ....	112
Equation 16: P-n junction diode current-voltage characteristics.....	121
Equation 17: P-n junction diode current-voltage characteristics with photo-generated current density. ....	122
Equation 18: Open circuit voltage of a p-n junction diode.....	123
Equation 19: J-V characteristics of a photovoltaic device under illumination with photo-generated current and series resistance. ....	123
Equation 20: The relation for the determination of the shunt resistance. ....	124
Equation 21: Simplified version of Equation 20 for dark measurements.....	124

# CHAPTER 1: INTRODUCTION

## 1.1 Background

The United States generated around 4.2 TWh of electricity in 2018 with the vast majority produced using coal, natural gas, and petroleum products. Less than 2% was generated by photovoltaic and thermal solar sources[1]. Advances in solar photovoltaic technology are essential to meet the electricity needs of an expanding world population with increased grid access. Demand for clean energy sources increases annually, yet barriers to the widespread adoption of photovoltaic technology, such as efficiency and cost, persist[2].

Development of non-silicon materials, often paired with thin-film and multijunction photovoltaic methods, is an avenue for photovoltaic advances[3]–[5]. Perovskite<sup>i</sup> structures became an emerging sub-field of photovoltaics in the late 2000s [6]; interest and study has expanded drastically since. Organic-inorganic hybrid halide perovskite solar cells (HPSCs) have attracted immense attention because of excellent optoelectronic properties and record power conversion efficiency (PCE) has surpassed 23.7% within a few years[7]. Organic-inorganic halide perovskites have emerged as promising materials for single junction and tandem solar cells, delivering 22.8% solar cell conversion efficiencies [8]. Perovskite tandem solar cells have shown efficiencies above 25% with silicon, and 17.8% with CIGS bottom cells, respectively [9]–[11]. Despite the very high efficiency already attained by HPSCs ( $ABX_3$ ; A = MA, FA, Cs; B = Pb,

---

<sup>i</sup> The term “perovskite” is used to describe a class of materials with a similar crystal structure to  $CaTiO_3$ , generalized as  $ABX_3$  where the A and B cations are bonded to an X anions which is usually a halide or oxygen. Perovskites are as varied in elemental makeup as in potential uses and are studied in numerous materials science disciplines.

Sn; X=I, Br, Cl) resulting from high absorption coefficient and electron-hole diffusion lengths, toxicity of Pb and stability of these materials are veritable issues [12]–[20]. MAPbI<sub>3</sub> is hydrophilic and volatile, resulting in poor stability under humidity, heat and UV exposure [16]. Therefore, significant effort is required to design novel protective coatings in conjunction with developing more stable perovskite compositions, such as Pb-free perovskites with more stable Rb<sup>+</sup> and Cs<sup>+</sup> cations [21]–[25].

Research exists on lead-free perovskite materials for photovoltaics with greater than 10<sup>4</sup> combinations of ABX<sub>3</sub>, A<sub>2</sub>BX<sub>6</sub> and other perovskites theoretically possible. However, there is a lack of systematic understanding of effect of defects, materials processing, crystal structures on bandgap and other opto-electronic properties [26]. Replacement of Pb<sup>2+</sup> with Sn<sup>2+</sup> seems to be a logical solution for addressing the toxicity issues (e.g. CsSnI<sub>3</sub>). However, a major challenge for Pb-free perovskites is poor power conversion efficiencies as divalent Sn<sup>2+</sup> and Ge<sup>2+</sup> tend to oxidize into 4+ oxidation state, generating excessive defects (Sn and Ge vacancies), and result in short carrier diffusion lengths [27]. Further replacing MA<sup>+</sup> and FA<sup>+</sup> with Cs<sup>+</sup> has been shown to enhance the stability of hybrid perovskite solar cells against thermal degradation [28]. A<sub>2</sub>BX<sub>6</sub> structure perovskites where half the B cations in the (111) plane are removed. Recently, A<sub>2</sub>BX<sub>6</sub> compounds with B = Sn, Te, Ti, Pd have been reported with tunable bandgaps and the ability to absorb light from the visible to infrared (IR) region [29]–[31].

The inorganic variant CsSnI<sub>3</sub> has received attention as a more stable alternative to CsSnI<sub>3</sub> based halide-perovskites for photovoltaic applications. Stability of CsSnI<sub>3</sub> can be attributed to 4+ oxidation state based on a simple ionic model; on the other hand, density-functional



calculations implicate the reason for stability to be the strong covalency of Sn-I bonds in the  $[SnI_6]^{2-}$  octahedral [32]. However, CsSnI<sub>3</sub> has found to exhibit deep defects that can be detrimental to performance of solar cells. Replacement of Sn with transition metals has also been explored with Cs<sub>2</sub>PdBr<sub>6</sub> with bandgap of 1.6 eV, however, working devices have yet to be demonstrated [31]. The A<sub>2</sub>BX<sub>6</sub> perovskite structure has also been demonstrated as Cs<sub>2</sub>TiI<sub>x</sub>Br<sub>6-x</sub> with a tunable bandgap in the range of 1.38-1.78 eV with an enhanced stability demonstrated as compared to MAPbI<sub>3</sub> [29].

A large number ( $> 10^4$  combinations) perovskite combinations exist considering variations in elements, alloys and modified perovskite structures. Experimental realization and concentrated study exist for relatively few combinations. Computational methods exist to evaluate perovskites formation probability, stability, bandgap and other material properties. Following the success of CsSnI<sub>3</sub>, computational studies were published evaluating other A<sub>2</sub>BX<sub>6</sub>, or “defect variant perovskites”. One such study considered density functional theory and/or hybrid functional for eighty-one known and unknown halide perovskites to identify the influences of the cations and anions on the direct bandgap and other properties [26].

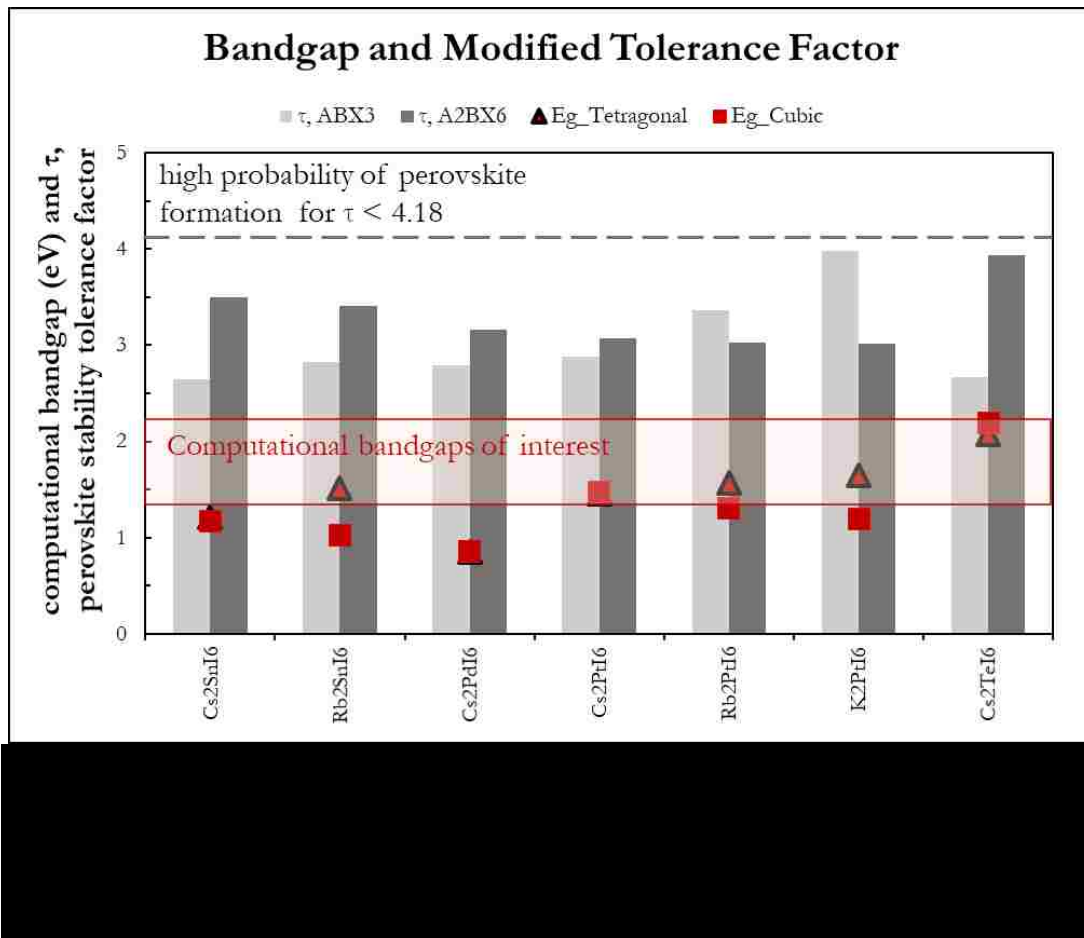
While many of the computational perovskites discussed have been experimentally proven, few lack thorough study for photovoltaic applications and may not be feasible using low temperature solution processing methods. In order to predict phase stability, a tolerance factor developed by Bartel et al. for halide and oxide perovskites as shown in Equation 1, was applied [33]. Results from this tolerance factor, along with the previously discussed computational bandgaps, can be found in Figure 1.

**Equation 1: A tolerance factor proposed by Bartel et al. [35]. A factor of under 4.18 is predictive of perovskite formation with a reported 92% for all perovskite types.**

$$\tau = \frac{r_X}{r_B} - n_A \left( n_A - \frac{r_A/r_B}{\ln \frac{r_a}{r_b}} \right)$$

Where “n” is the oxidation state and “r” denotes the atomic radius and the subscripts, “a”, “b”, or “x”, denote the cation or anion of the ABX<sub>3</sub> or A<sub>2</sub>BX<sub>6</sub> structure.

Unlike the more common Goldschmidt Tolerance Factor, the new tolerance factor accounts for the oxidation state of the A cation, increasing the predictive accuracy and probabilistic behavior [34][33]. This method, as well as other published methods, is specific to ABX<sub>3</sub> perovskites, with a 91% predictive accuracy reported for iodide-type perovskites[33]. However, it is reported that this predictive method can be used for modified perovskites (A<sub>2</sub>BB'X<sub>6</sub>) by taking the average atomic radius; thus the average atomic radius of an A<sub>2</sub>BX<sub>6</sub> perovskite will be half the atomic radius of the B cation. No predictive accuracy is available for this method.



From the figure, it is determined that all included elemental combinations might be stable in the ABX<sub>3</sub> or A<sub>2</sub>BX<sub>6</sub> perovskite phases with many of these materials being suitable for either single junction or wide bandgap top-cell for a tandem solar cells. Cs<sub>2</sub>PtI<sub>6</sub> is chosen as a model system for the A<sub>2</sub>BX<sub>6</sub> perovskites due to Pt being a noble metal, as well as Pt exhibits spin orbit coupling which makes it an ideal replacement for Pb. There is little existing experimental

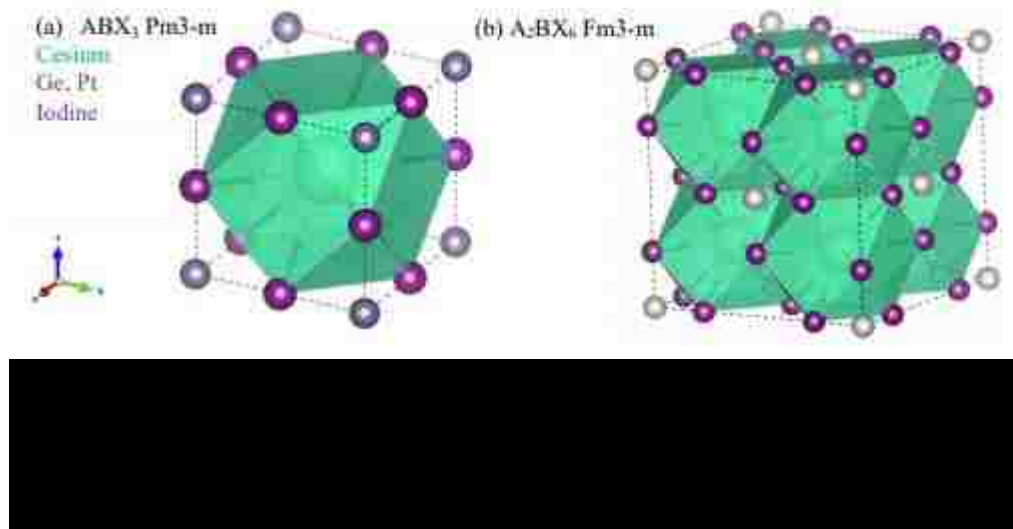
research on  $\text{Cs}_2\text{PtI}_6$  and only one computational paper (see Cai et al., [26]). Additionally, the substitution of platinum for tin was hypothesized to alleviate some of the oxidation and stability issues associated with cesium tin or germanium iodide perovskites. The current research provides first experimental evidence of  $\text{Cs}_2\text{PtI}_6$  crystals processed via precursor based solution deposition methods; tunability of bandgap through solvent and solute engineering with incorporation of Cl, and chalcogens (O and S); absorption coefficients of  $1.9 \times 10^5 \text{ cm}^{-1}$  at 1.7 eV with high majority carrier mobility and minority carrier lifetimes.

In this work, thin films of crystalline  $\text{A}_2\text{BX}_6$  ( $\text{A} = \text{Cs}$ ,  $\text{B} = \text{Pt}$ ,  $\text{X} = \text{I}$ ) cubic and tetragonal phases as well as an oxygen containing phase (not indexed yet) have been synthesized reproducibly via atmospheric solution processing. The crystal structure of the  $\text{Cs}_2\text{PtI}_6$  can be derived from the  $\text{ABX}_3$  ( $\text{CsPtI}_3$ ) by removing alternate Pt layer along  $\langle 111 \rangle$  direction resulting in a cubic structure as shown in Figure 2. The platinum iodide octahedra with a 2- charge ( $[\text{PtI}_6]^{2-}$ ) forms a cage around the  $\text{Cs}^+$  ions, resulting in a unit cell of space group  $\text{Fm}\bar{3}\text{m}$  and a lattice parameter of 11.36 Å. The following sections demonstrate these Pb-free, cesium platinum iodide wide bandgap semiconductors will be well-suited for single junction and tandem photovoltaics. Being a noble metal Pt is considered cost-prohibitive for low cost photovoltaic applications, however, we

---

ii The first report, published in 1966, mentions  $\text{Cs}_2\text{PtI}_6$  as having a tetragonal lattice and provides little discussion [47]. The second report of  $\text{Cs}_2\text{PtI}_6$ , published in 1982, suggests a dark-red color and a lattice parameter of 11.361 Å, which was used in a computational pattern published in 1992 and agrees with the results of this experimental effort [42].  $\text{Cs}_2\text{PtI}_6$  is not the main topic of either report and information provided is very limited.

estimate that due to high absorption coefficient of  $\text{Cs}_2\text{PtI}_6$ , minimal materials cost will be added over  $\text{MAPbI}_3$ .



## 1.2 Methodology

The following section describes the methods used during perovskite synthesis, device fabrication and material and device testing. All material synthesis was done using low temperature solution-based processing, a method common in perovskite synthesis.

### 1.2.1 Solution Processing

The cesium platinum iodide perovskites synthesized during this research effort are entirely solution processed in mostly atmospheric conditions. This processing method is inexpensive, requires limited equipment and is adaptable for other perovskite type processes. However, solution processing is imprecise as compared to other processing methods. Processing in atmospheric conditions, as opposed to processing in an inert gas glove box, inevitably affect the perovskite formation. The description below is a general description of the process used to synthesize cesium platinum iodide perovskite films and devices. Certain variables are discussed in detail in the results section of this document.

### Materials Used

In order to synthesize  $\text{Cs}_2\text{PtI}_6$  using solution processing, solutes and solvents are combined to make an intermediate phase within a solution and then annealed on a superstrate, ideally resulting in a perovskite phase. Two solute combinations are used, described below in Equation

2. A summary of solvents and solutes used in processing is provided in Table 1 with further details in the following section.

**Equation 2: Ideal reactions for cesium platinum iodide perovskites using two solute combinations.**

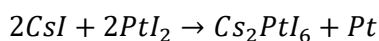
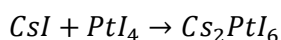


**Table 1: Summary of solutes and solvents used in the cesium platinum iodide solution processing process.**

<b>Chemical</b>	<b>Molecular Formula</b>	<b>Molar Mass [g/mol]</b>	<b>Hazards</b>
<b>Cesium Iodide</b>	CsI	259.809	Skin irritant, eye irritant, respiratory irritant, aquatic toxicity
<b>Platinum(II) Iodide</b>	PtI <sub>2</sub>	448.893	Skin irritant, eye irritant, respiratory irritant
<b>Platinum(IV) Iodide</b>	PtI <sub>4</sub>	702.702	Skin burns, eye damage
<b>N-Dimethylformamide (DMF)</b>	C <sub>3</sub> H <sub>7</sub> NO	73.095	Skin irritant, eye irritant, respiratory irritant
<b>dimethyl sulfoxide (DMSO)</b>	(CH <sub>3</sub> ) <sub>2</sub> SO	78.130	Skin irritant, eye irritant, respiratory irritant
<b>γ-Butyrolactone (GBL)</b>	C <sub>4</sub> H <sub>6</sub> O <sub>2</sub>	86.089	Skin irritant, eye irritant, respiratory irritant

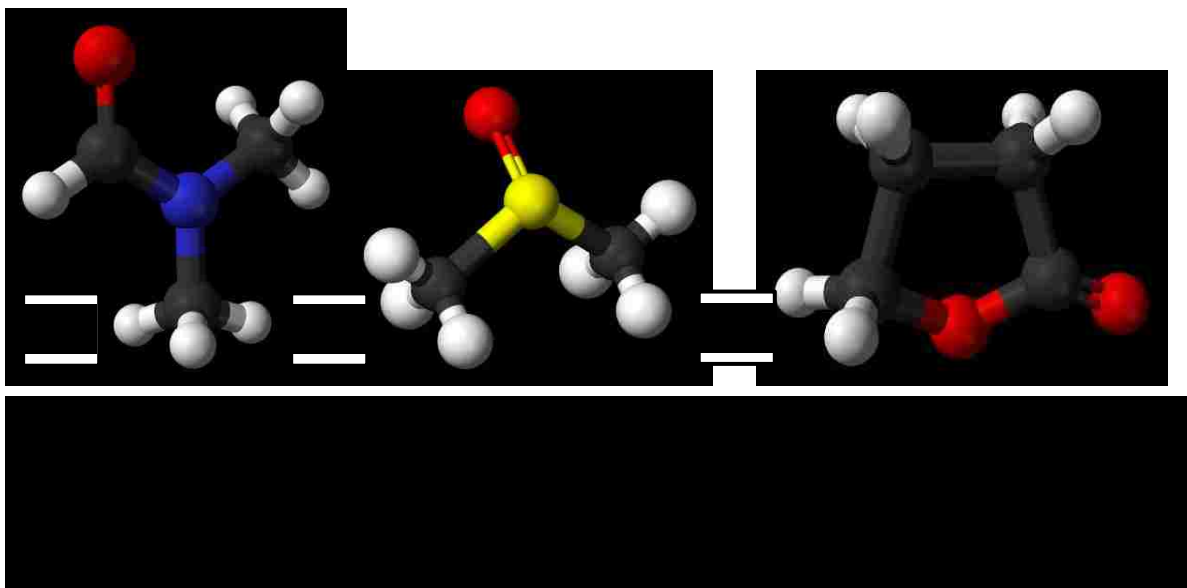
**Solutes:**

Cesium iodide, platinum(II) iodide, and platinum(IV) iodide are used for cesium platinum iodide perovskite processing. The choice of these chemicals was necessitated by the desired result of  $\text{Cs}_2\text{Ptl}_6$ . These solutes are all purchased in a powder form through Sigma Aldrich and/or Alpha Aesar with a >98% purity. These chemicals are stored in a nitrogen filled glove-box.

**Solvents:**

Three solvents are used within this processing method. Solvents and solute interactions are important in solution based processing. It is not completely understood why some solvents/solvent combinations reliably result in perovskite formation and others do not. The three solvents experimented with in cesium platinum iodide processing are common in perovskite processing and have common properties such as a high boiling point and limited toxicity. Molecular images of each solvent type can be found in Figure 3. Solvents used were purchased through Sigma Aldrich. Solvents are stored in a nitrogen filled glove box. Further information about each solvent is provided below.





**DMF:** DMF (N-Dimethylformamide) is a relatively common solvent in perovskite and industrial processes. DMF's highly miscible nature are beneficial for processes where it may be mixed with other solvents[35]. It is colorless and odorless when pure with a boiling point of 153°C. It is flammable and should be kept in a well ventilated area when above 58°C. Multiple toxicity concerns are associated with DMF including: liver damage, alcohol intolerance, reproductive issues and skin irritation. All processing using DMF occurs within a fume hood.

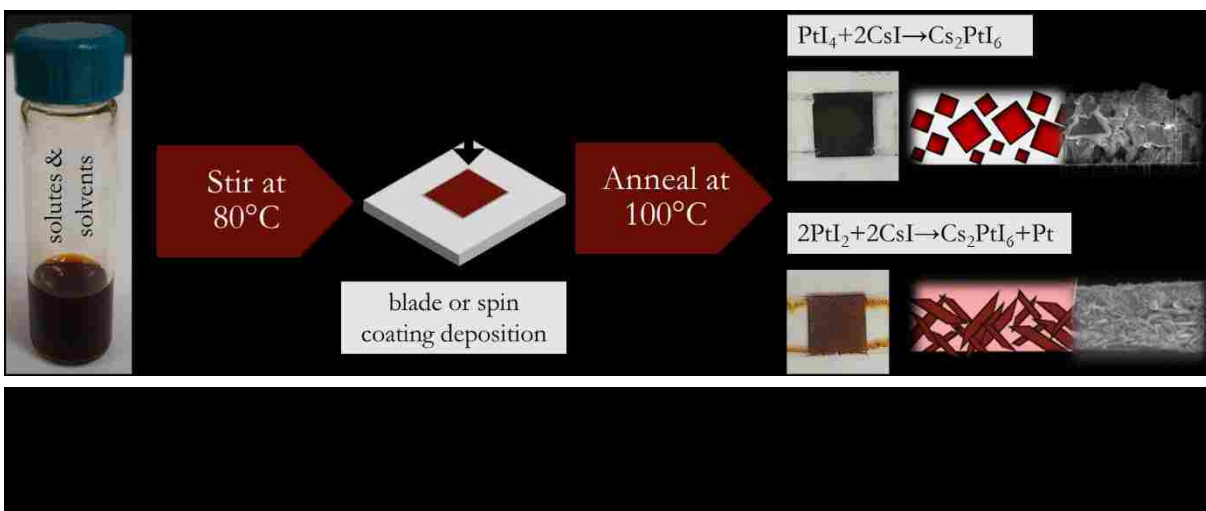
**DMSO:** DMSO (dimethyl sulfoxide) is another relatively common in perovskite and industrial processes including pharmaceuticals. DMSO is highly polar highly miscible[36]. It is colorless and odorless when pure with a boiling point of 189°C. It is flammable and should be kept in a well ventilated area when above 87°C. DMSO has fewer toxicity concerns than DMF but contact with skin should be avoided. DMSO is unique in ability to penetrate body membranes without damaging membranes; it can potentially carry harmful chemicals through body membranes.

All processing using DMSO occurs within a fume hood. If gloves are contaminated by a DMSO-containing solution, they should be immediately replaced to reduce risk of skin absorption.

**GBL :** GBL (gamma-Butyrolactone) is relatively common solvent in perovskite and is industrially used as to produce other chemicals, including methyl-2-pyrrolidone (NMP)[37]. It is colorless, has a boiling point of 204°C and it is flammable and should be kept in a well ventilated area when above 98°C[37]. GBL has the least toxicity concerns of the three solvents used but is a skin and eye irritant. All processing using GBL occurs within a fume hood. GBL is a List 1 controlled substance in the United States as it can be used to make  $\gamma$ -hydroxybutyric acid (GHB), a club drug. GBL can be expensive and more difficult to obtain for lab use.

## ■ Perovskite Film Synthesis and Device Fabrication Process

An advantage to solution processing for perovskite synthesis includes a relatively straightforward process: the solutes and solvents are measured, mixed on a hotplate, and annealed in a vacuum oven. A visual summary of the process can be found in Figure 4. A complete procedure follows.



The general process used is as follows:

1. Pre-heat the vacuum oven to 100°C (dial at 4.6) for at least two hours.
  - Turn the vacuum oven dial to 4.6 (UNLV specific)
2. Measure solvent using plastic pipette and pre-heat in a small, capped vial on a hot plate at 75°C for 15 minutes. Place a magnetic stirrer in the vial and set the hotplate rotation to 250 rpm to enhance heat transfer and solubility after the solute is added to the solvent.
  - Solvent volume is usually 1-2 mL
  - DMF, DMSO, GBL, or a combination of these solvents is used
3. Weigh the chemical reactants to within  $\pm 0.001$  g of the desired amount in individual weight boats.
  - Reactant chemicals used are PtI<sub>4</sub>, PtI<sub>2</sub>, and CsI
  - A product molarity of 0.2 to 0.4 is used to determine solute weight
  - See APPENDIX B for detailed molarity calculations

4. Combine solutes with solution and stirred on a hotplate at 75°C for 2 hours.
  - To reduce unreacted solute on the side of the vial, pipet solvent out of vial prior to adding solute, add solute, and pipet the solvent back into the vial, allowing the solvent to dislodge stuck solute from the vial sides
5. Prepare superstrate with 5 mm<sup>2</sup> or 1 cm<sup>2</sup> area.
  - Microscope slides are generally used for perovskite film
  - ITO (indium tin oxide), FTO (fluorine doped tin oxide), CdS (cadmium sulfide), and ZnO,S (zinc oxi-sulfide) layers may be present in devices
  - Use kapton tape to designate a 5mm<sup>2</sup> or 1 cm<sup>2</sup> film area
6. Preheat the superstrate on a hotplate at 75°C for at least thirty minutes.
7. Deposition of films:
  - Blade process:
    - i. Pipette 50 µL of solution onto the exposed substrate area. Use a blade to smooth out film in one motion
    - ii. Anneal in the vacuum oven for 60 minutes at -15 inHg
  - Spin coating process:
    - i. Drop 10-50 µL of solution onto film while spin coater is spinning at 250-1000 rpm
    - ii. Immediately transfer to vacuum oven and anneal for 15 minutes at -15 inHg (50 kPa).
8. Remove from oven and remove Kapton tape

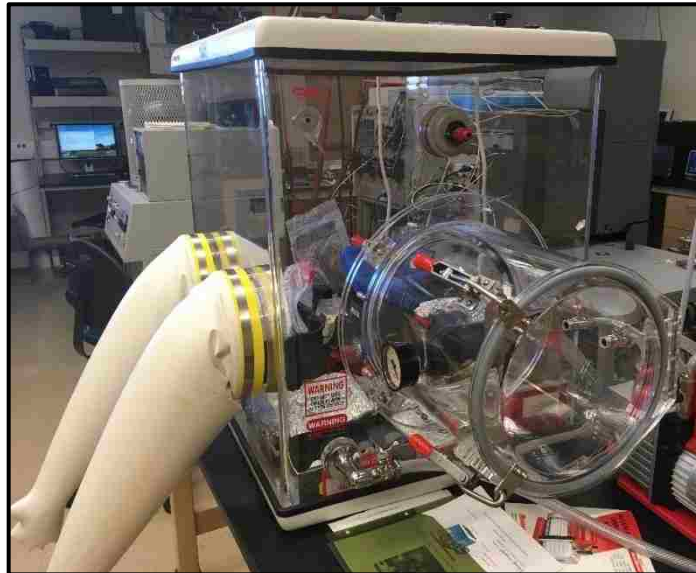
9. **For films:** Place films in clear plastic boxes and transfer to the nitrogen filled glovebox while not testing. Further steps concern only device fabrication.
10. **For devices:** Re-tape around the perovskite area, slightly overlapping the perovskite film. Allow tape to extend over superstrate edges to reduce the risk of shorting the device.
11. Use conductive graphite paste to create a positive and negative lead contacts on the film and superstrate surfaces.
12. Place conductive tape leads (copper or aluminum coated tin) carefully on the positive and negative contacts.
13. Test immediately.
14. Transfer annealed film to the nitrogen filled glovebox while not testing.

## ■ Degradation Mitigation

In order to decrease the risk of material decomposition and prolong sample lifetime, the following procedures were strictly adhered to.

1. Immediately following annealing, cells were placed in clear plastic cell cases to prevent foreign objects from damaging the sample surface.
2. Samples were transferred to the nitrogen filled glovebox seen in Figure 5. All items placed into the glovebox are vacuumed to -20 inHg (70 kPa) and flooded with nitrogen twice in order to reduce the amount of oxygen in the glovebox. The samples are

annealed under a similar vacuum; negative pressure in this step is not believed to damage samples further.



3. Samples are removed from the glove box for testing. The effects of testing on sample composition are not yet fully understood.
  - a. For samples to be tested outside of the UNLV's Center for Energy Research Photovoltaic and Material Laboratory, some amount of testing on samples from the same batch is completed to ensure quality samples are sent out. The samples being sent are not tested upon.
4. Samples are placed back into the glove box after testing if required for further testing
5. Sample testing is generally complete within two weeks of fabrication

6. Samples that are sent to other laboratory's or otherwise need to be outside the glovebox for a prolong duration while not being tested are vacuum packed and sealed to reduce oxygen content. Shipped samples are taped to the sample case to protect it during the transportation process.

### **1.2.2 Measurement and Testing Methods**

Materials testing is a significant component of this project; prior to testing, the material and material properties are unknown. Furthermore, the processing methods used generally result in variability among materials synthesized. In order to characterize materials and understand the application to solar photovoltaics, testing is completed by the author, other groups at UNLV and outside universities and laboratories. A description of the testing done is given below.

### **1.2.3 Material Characterization and Device Testing Completed at UNLV's Photovoltaics and Materials Laboratory**

The testing methods in this section describe material characterization methods used by the author. An equipment overview, method description and summary of use procedure is provided for each characterization method. An overview of each method can be found in Table 2.

**Table 2: Equipment used for materials characterization and device testing.**

<b>Method</b>	<b>Make</b>	<b>Model</b>	<b>Purpose</b>	<b>UNLV Contact</b>
<b>UV/Vis/NIR</b>	Shimadzu	UV-2600	bandgap and absorption coefficient	CER, PML
<b>XRD (powder)</b>	Bruker	D8 Advance	phase identification, lattice parameter	Radiochemistry
<b>SEM</b>	JEOL	JSM-5610	Morphology, film thickness, grain size, crystal size	EMIL
<b>EDS</b>	JEOL	JSM-5610	chemical composition	EMIL
<b>JV</b>	ABET/Kiethly	100/2410 SourceMeter	diode curve, determination of built-in voltage, dark saturation current, diode ideality factor	CER, PML
<b>CV</b>	Solartron	SI 1260	Determination of built-in voltage, depletion width, doping density.	CER, PML
<b>XPS</b>	-	-	Composition	Evans Analytical
<b>ToFSIMS</b>	-	-	Composition	Colorado School of Mines
<b>PL and TRPL</b>	-	-	Bandgap, minority carrier lifetime	Molecular Foundry

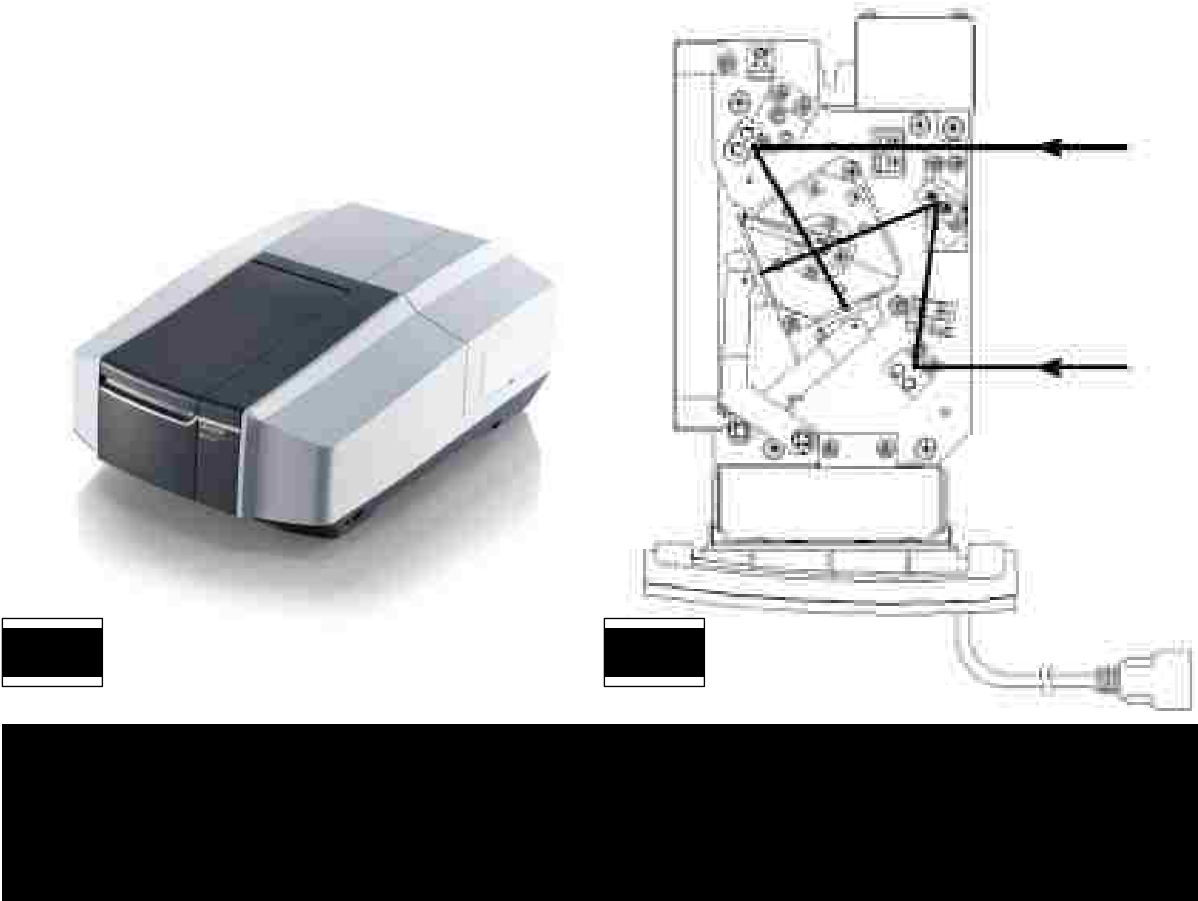


## ■ Ultraviolet/Visible/Near IR Spectroscopy (UV/Vis/NIR)

### **Method:**

The Shimadzu UV-2600 spectrometer (or “spectrophotometer”) used includes optical mirrors, a light source, monochromator and choppers, an integrating sphere, filter wheel, and software to record Transmission and Reflection data. Light, which is produced at the source, travels through the filter wheel and monochromator to split the light before it enters the chopper. The chopper separates the light into two paths for transmission and reflection measurements. A schematic can be found in Figure 6.

For transmission measurements, sample, with film facing away from the integrating sphere, is placed in beam path in front of integrating sphere at the transmittance clip “T” location as marked in Figure 7. The film faces the integrating sphere during reflection measurements, and is located at the reflectance holder “R”, also marked in Figure 7. The use of integrating sphere allows us to measure “diffuse” reflection from rough surfaces for characterization of our thin-film samples. Ultraviolet-Visible Spectroscopy (UV-Vis) uses monochromatic visible and near visible light wavelengths (300-1400 nm in this case) to determine the reflectance and transmittance of a film sample. This measurement is performed under atmospheric conditions. Total measuring time for transmittance and reflectance totals to about six minutes. However, samples are generally measured in batches and are out of the glove box for 1-2 hours.



The film's absorption coefficient and bandgap, as well as material qualities such as the refraction index, extinction coefficient, and sample thickness can be determined from transmission and reflection data resulting from this method. In this research, transmission and absorption measurements are used to determine absorption coefficient ( $\alpha$ ) and subsequently the bandgap ( $E_g$ ).

Incident photons that have wavelengths less than the bandgap wavelength,  $\lambda_g$ , are absorbed throughout the thickness of the semiconductor material. The light intensity (proportional to the

amount of photons), experiences decay with the distance traveled through the semiconductor.

The relationship between light intensity,  $I$ , and the distance from the material surface,  $x$ , is given by Equation 3.

**Equation 3: Intensity of radiation.**

$$I(x) = I_0 \exp(-\alpha x)$$

Where  $I_0$  is the intensity of the incident radiation and  $\alpha$  is the absorption coefficient that depends on the photon energy or wavelength,  $\lambda$ . The absorption coefficient  $\alpha$  is a material property defining penetration depth  $1/\alpha$  as the distance over which 63% of photon absorption occurs. The absorption coefficient is related to reflection and transmission measurements as described in Equation 4:

**Equation 4: Relation of transmission, reflection and absorption.**

$$T = \frac{(1 - R)^2 \exp(-ad)}{[1 - R^2 \exp(-2ad)]}$$

For materials with high absorption, appropriate for the cesium platinum perovskite material analyzed here), the product of the material thickness and absorption coefficient becomes much greater than unity, or  $ad \gg 1$ . As the denominator approaches unity, above equation can be approximated as in Equation 5.

**Equation 5: Relation of transmission, reflectance and absorption for high absorption materials.**

$$T \approx (1 - R)^2 \exp(-ad)$$

## Results:

From the reflectance and transmittance measurements, absorbance, absorption coefficient, and the Tauc relation can be determined. This allows for the determination of material bandgap and some amount of characterization. UV-Vis is performed on most film samples and is a check in sample regularity before more time intensive testing is completed. The Shimadzu UV-2600 spectrophotometer used with interior schematic of the optical pathways can be found in Figure 6 [38]. An image of the spectrophotometer interior can be found in Figure 7. A complete description of testing and analysis methods can be found in APPENDIX A.



## ■ Powder X-Ray Diffraction (XRD)

### **Method:**

Powder X-ray diffraction, or XRD, has been invaluable to this research for phase identification and quantifying the difference between two material types with unknown phases. The powder diffractometer used in the effort is the Bruker D8 Advance XRD used is located in SEB 1138, seen in Figure 8 and contains a vacuum tube X-ray source, goniometer, slits, Johansson-type germanium monochromator, and detector to produce, filter and detect the x-rays used. The instrument utilized has a Bragg-Brentano or  $\theta - 2\theta$  focusing geometry configuration.

The X-ray source used includes a tungsten filament for cathode (under high voltage) and copper anode within a vacuum tube. The cathode emits electrons, which are the accelerated toward the anode; the anode becomes excited and emits X-rays, which then exit the tube. The water cooled throughout this process to prevent overheating. After the X-rays exit the tube, they enter goniometer through the “Soller slit” and “Divergent slit”. These slits make the incoming X-ray beams parallel and further control the spreading of the X-rays prior to sample impact. As the X-rays interact with the sample, they are diffracted and again made parallel before it hitting the monochromator, which separates the X-rays by on wavelength, thus minimizing or

eliminating background radiation such as fluorescence,  $CuK\alpha_2$ , or  $CuK\beta$ , enabling  $CuK\alpha_1$  as the only X-ray emission line.



As the sample and detector increase in  $2\theta$ , constructive interference resulting from specific  $d_{hkl}$  can be observed at specific  $2\theta$  values, as represented by Bragg's Law as in Equation 6. From this equation, it is apparent the resulting  $d$  to  $2\theta$  relationship is dependent upon the wavelength of radiation used. More complex structures can be similarly predicted so long as the crystal structure and lattice parameters are known. Once phases are determined, quantitative phase analysis is done by Rietveld structure refinement methods. Modern diffraction data analysis is done with the assistance of databases of experimental and computational patterns and software to match the user's data with patterns; Rietveld structure refinement is made much simpler and faster with the use of analytical software intended for Powder XRD phase analysis.

**Equation 6: Bragg law for 1<sup>st</sup> order diffraction**

$$d_{hkl} = \frac{\lambda}{2 \sin \theta}$$

**Equation 7: General quadratic form for a cubic system of Bragg law for the relation between the diffraction angle, lattice planes and the lattice parameter.**

$$\sin^2 \theta = \frac{\lambda^2}{4a^2} [h^2 + k^2 + l^2]$$

**Results:**

XRD can be used to determine a samples crystal structure, phase composition, lattice parameters, and lattice strain and crystal size. More information can be determined with the aid of software analysis. XRD is a powerful method for phase identification but is limited by sample quality. For samples with multiple unknown phases present, quantification becomes much more difficult. Additionally, phase identification through software databases are limited by available crystal information files (CIF) in within the databases. Machine and sample set-up has an effect on pattern output; while correction methods are available using software, a complete correction is difficult without the use of a standard within the sample. Powder diffraction patterns for variations to the Cs<sub>2</sub>PtI<sub>6</sub> perovskite such as CsPtI<sub>3</sub> and O or S containing phases are not available; further research is needed to index these peaks.

## ■ Scanning Electron Microscopy

### **Method:**

Scanning electron microscopy, or SEM, is an imaging technique that produces an image using a beam of electrons to scan the surface of a sample. Secondary electrons emitted from the sample are collected by a detector and used to create an image of the sample. By reducing the raster area (area scanned), the image can be magnified up to 500,000 times. The JEOL scanning electron microscope model JSM-5610 used at UNLV as seen in Figure 9 can produce quality images at a magnification of up to 10,000x depending on the last time serviced, settings, and the subjective definition of quality.





## Results:

SEM is used to see surface morphology (including structures, grain size, distribution, and orientation), identify defects (such as pin holes) and check surface uniformity. Additionally, a sample cross sectional thickness can be determined.

## Energy Dispersive Spectroscopy

### Method:

Energy Dispersive Spectroscopy (EDS) is a chemical analysis technique that detects x-rays emitted from a sample. The equipment used for EDS is the same as for SEM (see Figure 9) with the addition of an EDS x-ray detector. As the sample is hit by an electron beam, the surface

atom electrons are ejected; the resulting vacancies are filled by higher state electrons, causing the emission of an x-ray characteristic to the element. The elemental composition is determined by the energy at which x-rays are emitted and the relative intensity, or counts, of the x-ray emissions. Mathematical methods are then used to determine the elemental composition of a sample point of interest.

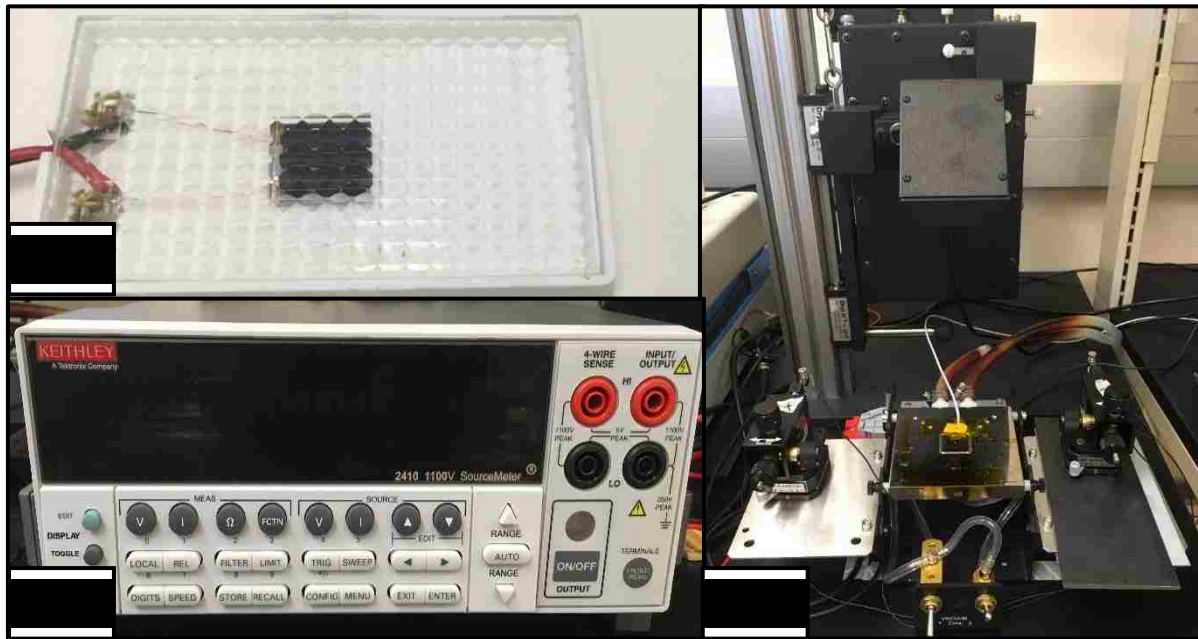
### **Results:**

The characteristic energy of x-rays and intensity of emissions result from EDS analysis. Using EDS specific analytical software, this information results in an elemental composition. The information can be processed without the aid of software but is generally not done in the modern use of EDS. Using EDS an estimate of the elemental composition of a sample can be determined with accuracy dependent upon the atomic number. EDS is unable to detect elements with atomic numbers below an atomic number of five and limited in the quantification of common elements with lower atomic numbers such as oxygen and carbon. EDS may detect substrate surface or surroundings for thin film materials, especially during cross sectional measurements. For best results a sample should be smoothed and polished; however, smoothing and polishing may damage thin film materials and is not recommended. All elemental composition measurements should be considered estimates and should be confirmed using alternate methods if accuracy is required.

## Current Voltage Measurements

### Method:

Current Voltage (J-V) measurements allow the determination of J-V behavior including short circuit current ( $J_{sc}$ ), open circuit voltage ( $V_{oc}$ ), fill factor (FF), efficiency ( $\eta$ ) and confirm photovoltaic behavior. These measurements are done using a combination of equipment including an ABET Solar Simulator (supplies light at  $100 \text{ mW/cm}^2$ ) and a Keithley 2410 SourceMeter paired with Lab View software to record measurements, shown in Figure 10. A device is biased to a certain range of voltages and the resulting current is recorded.



**Results:**

Light and dark sweeps can be made using this method. A dark sweep can confirm diode behavior. A light sweep can result in a J-V curves used to determine device performance including short circuit current ( $J_{sc}$ ), open circuit voltage ( $V_{oc}$ ), fill factor (FF) and efficiency ( $\eta$ ). The shape of the curves can provide some information about series resistance and other non-optimal device issues.

**Limitations:**

Dark tests do not occur in a dark room. A light reducing cloth is used to shield devices from ambient light but it may have some effect on measurements. Although the solar simulator is calibrated before each use, the cell position influences the power received so the cell must be well centered. Additionally, the lamp shutter must be opened prior to the beginning of the JV sweep.

**1.2.4 Testing Methods Not Completed By the Author**

The following testing methods are reported on within this document but were not completed by the author. A brief summary of the testing technique is provided along with the testing location.

## ■ Timed-Resolved Photoluminescence

Timed-Resolved Photoluminescence (TRPL) is a method in which free charge carrier lifetimes may be determined. This is done by measuring the time it takes for electron-hole pairs to decay to a lower energy state following a short pulse of light, then recombine and emit light [39].

TRPL measurements are conducted at Lawrence Berkeley National Laboratory's Molecular Foundry through a User Agreement.

The setup was built around a Nikon Eclipse Ti-U microscope with 0.3NA objective. For one photon excitation a 405 nm nanosecond pulsed laser system (Thorlabs NPL41B, 6ns pulse width, 1MHz repetition rate) was used. PL was filtered with a 540 nm and a 532 nm long-pass filters. TRPL data were collected with a photon counting detector (Micro Photon Devices, PDM Series) and a time correlated single-photon counting (TCSPC) module (PicoQuant, PicoHarp300). An Andor Kymera 328i spectrometer with 50 grooves/mm grating (blazing angle of 600nm) and an Andor iXon electron-multiplied CCD were used to collect spectra.

## ■ Differential Scanning Calorimetry

Differential Scanning Calorimetry (DSC) is used to detect phase transitions by measuring the heat flux (power) to the sample is monitored against time and/or temperature as compared to a known reference ( $\text{Al}_2\text{O}_3$  for our measurements). During DSC measurements, a sample of known

mass is heated (or cooled) and the changes in the heat capacity of the sample are measured as changes in the heat flux. This allows to detections of transitions such as melting, glass transition temperature, phase or structural changes, and curing of materials. It is a very widely used tool for thermal analysis in pharmaceuticals, food, paper, manufacturing, semiconductors and electronics. To determine the phase stability of these novel perovskite materials, DSC is a useful technique to determine the decomposition temperature of inorganic phase and organic solvent losses. For the purpose of novel perovskite synthesis, DSC measurements can help determine the temperature at which a perovskite material will decompose and cease to function as a photovoltaic material[40]. Although a thermogravimetric analysis (TGA) coupled with DSC is more accurate in determination of transition temperatures, preliminary results from DSC measurements show encouraging information. DSC data and analysis was performed in collaboration with UNLV's Radiochemistry Department.

## CHAPTER 2: RESULTS AND ANALYSIS

In this chapter, the results and analysis of perovskite material synthesis and device performance will be presented. Significantly different film characteristics are found when using different solute and solvent combinations; each solute combination and material result warrants an individual sub-section. The effect of solvent use on material synthesis is discussed along with detailed results of material characterization and properties for two cesium platinum iodide materials. A final sub-section details the results of film fabrication from the two materials previously detailed.

### 2.1 Platinum Tetra Iodide and Cesium Iodide Derived Perovskite Synthesis

Perovskite materials made using platinum(IV) iodide and cesium iodide follow the process procedure provided in the methodology section. It was determined these solutes dissolve best in a 50/50 combination by volume of the solvents DMSO and DMF. The reasons for this can be determined in further work. Combinations including GBL alone, DMF alone and combinations of GBL and DMF resulted in a very loose powder with poor adhesion; while some amount of this result is identified to be  $\text{Cs}_2\text{PtI}_6$  from preliminary XRD analysis, these samples were very difficult to analyze and were not studied in detail. Further work with other solvents may yield interesting results; only results from DMF/DMSO with  $\text{PtI}_4$  and CsI are discussed in this section.

The  $\text{PtI}_4$  and CsI solute combination processed in 0.25M DMF/DMSO solution and deposited on a glass or coated superstrate using doctor blade methods. Spin coating was done and is discussed but doctor blade methods yielded consistent results and was found to be more reliable for film characterization methods. An example of an annealed film can be found in Figure 11. Films made from  $\text{PtI}_4$  and CsI in DMF/DMSO solvent are consistently black in color. 100% of samples made using this method were observably similar to the figure image.

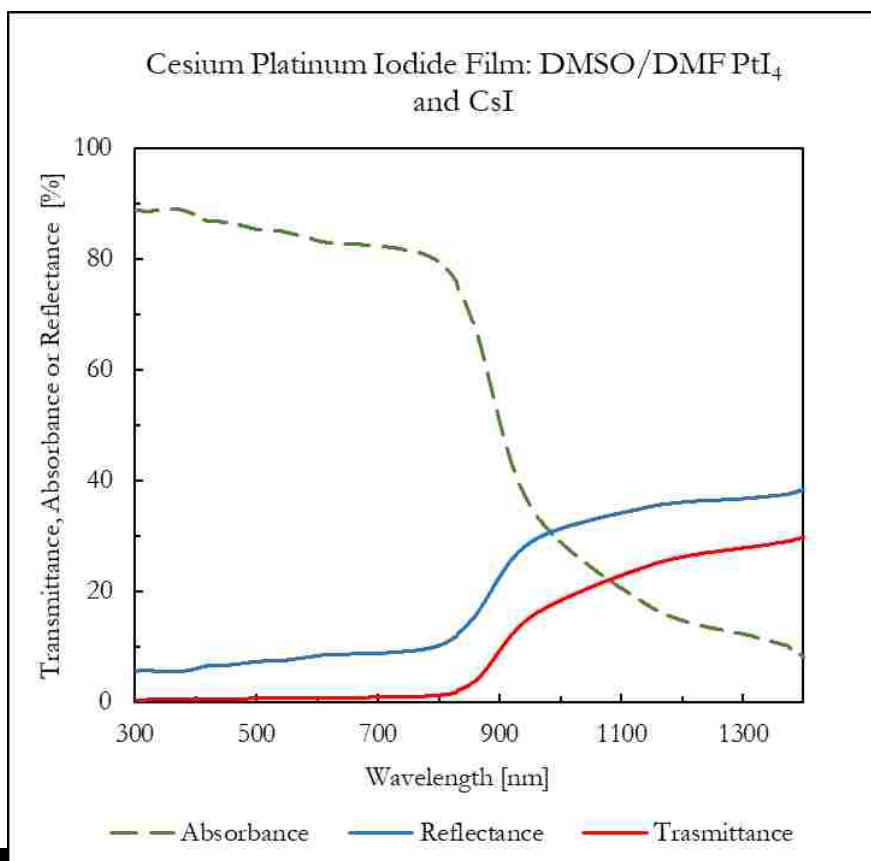


### 2.1.1 Optical Properties and Bandgap Determination

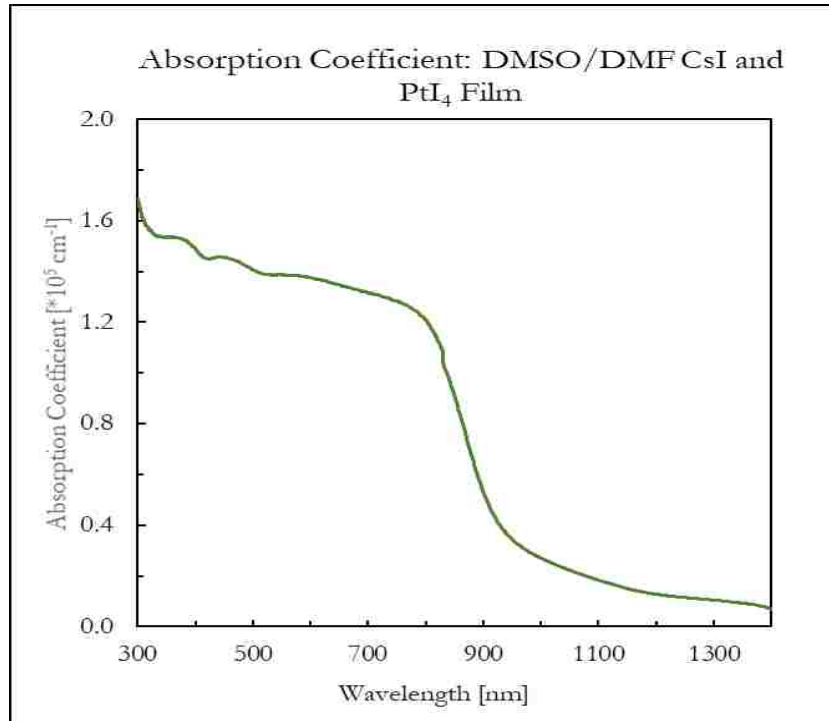
Using UV-Vis spectroscopy, transmittance and reflectance measurements made from wavelengths ranging from 300 to 1400 nm on a film sample deposited on a glass superstrate. As observed in Figure 12, the transmittance and reflectance are relatively low (<10%) for lower wavelength, higher energy photons, resulting in the calculated absorbance to be high (>80%) at



wavelengths under 850 nm. Using the methods and equations described in the Chapter 1, the absorbance was calculated using transmittance and reflectance data.

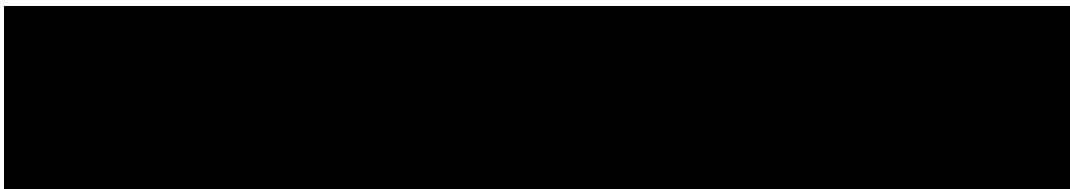
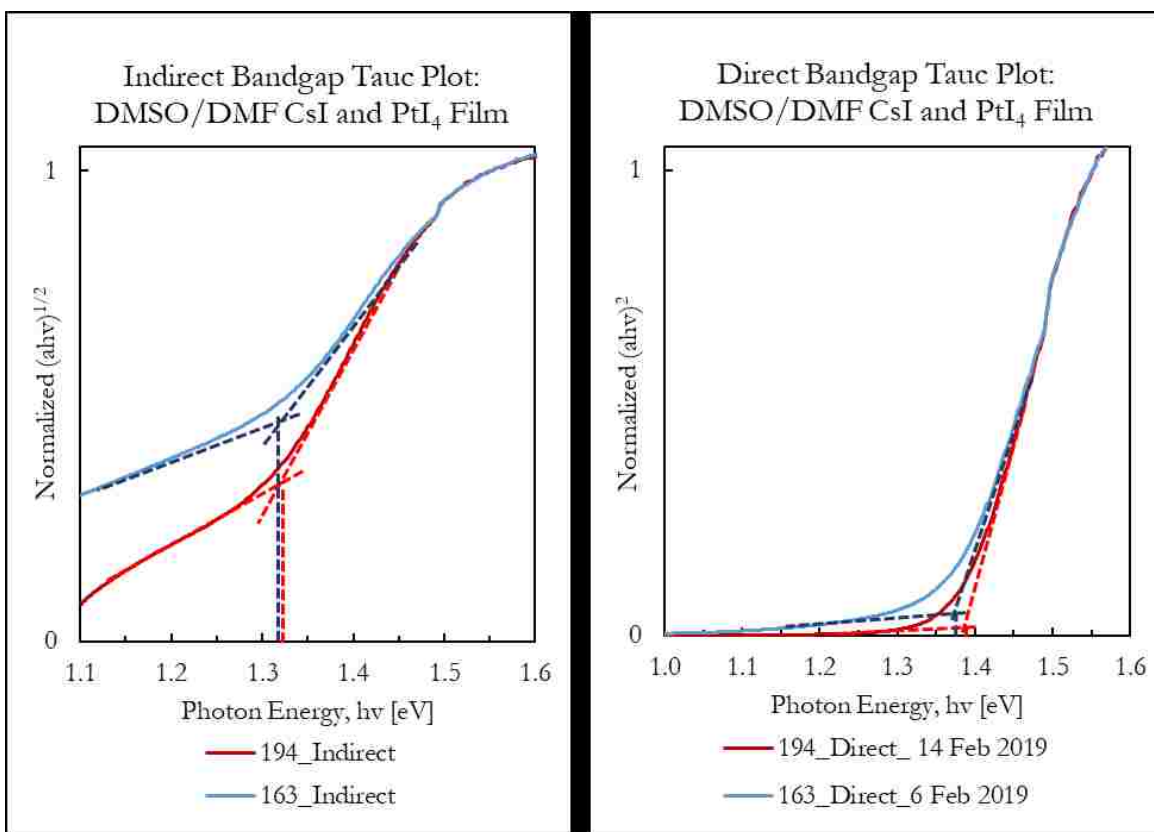


Using the transmittance and reflectance, the absorbance coefficient was calculated for the range of measurements given as seen in Figure 13. The absorbance coefficient is a measure of how much light of a certain wavelength is absorbed by a certain thickness of the material; this material has relatively high absorbance and absorption coefficient. Additionally, this material has a prominent absorption edge at about 860 nm, indicating much of the light below this wavelength is absorbed by the material. Comparison to other perovskite materials can be found in Chapter 3.



The Tauc method can be used to determine the materials optical bandgap. A direct bandgap is estimated by computational studies for the Cs<sub>2</sub>PtI<sub>6</sub> material[26]. Both indirect and direct Tauc

methods are used to evaluate the material band gap. The indirect and direct bandgap Tauc plots with linear approximation of the bandgap can be found in Figure 14 for two film samples from identical processes occurring on separate days. The direct bandgap as determined by UV-vis Tauc is slightly below 1.4 eV; the indirect bandgap for this material is slightly above 1.3 eV. These results are in agreement with the direct bandgap estimate for Cs<sub>2</sub>PtI<sub>6</sub> published in 2018 by Cai et al., with an estimate of 1.34 eV–1.47 eV, respectively with and without spin orbit coupling [26]. While the experimental results found are not enough to determine spin orbit coupling, they do point to some amount of absorbance through the slightly lower indirect bandgap.



The variations between samples is relatively low. Samples from four batches synthesized from November 2018 through February 2019 indicate an average indirect bandgap of 1.33 eV and an average direct bandgap of 1.36 eV, as demonstrated in Table 3. The standard deviation of 0.0065 eV (indirect) and 0.0171 eV (direct) are relatively low and indicate minimal variation between batches. By observation, the sample data is similar with no other major bandgaps or absorption

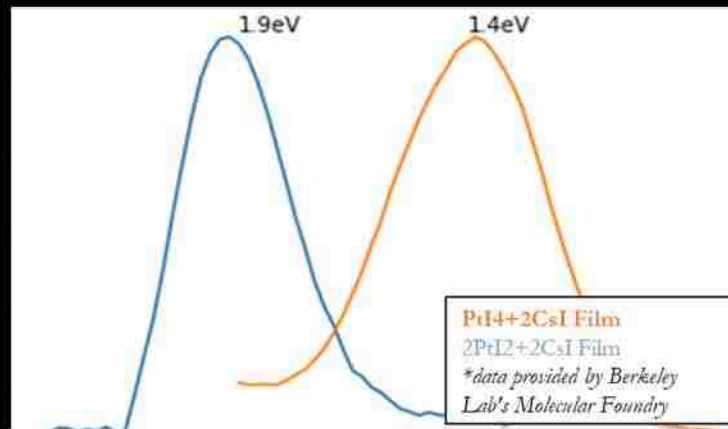
edges apparent. The amount of observable and calculated variation between four sample batches indicate this material synthesis is easily repeatable.

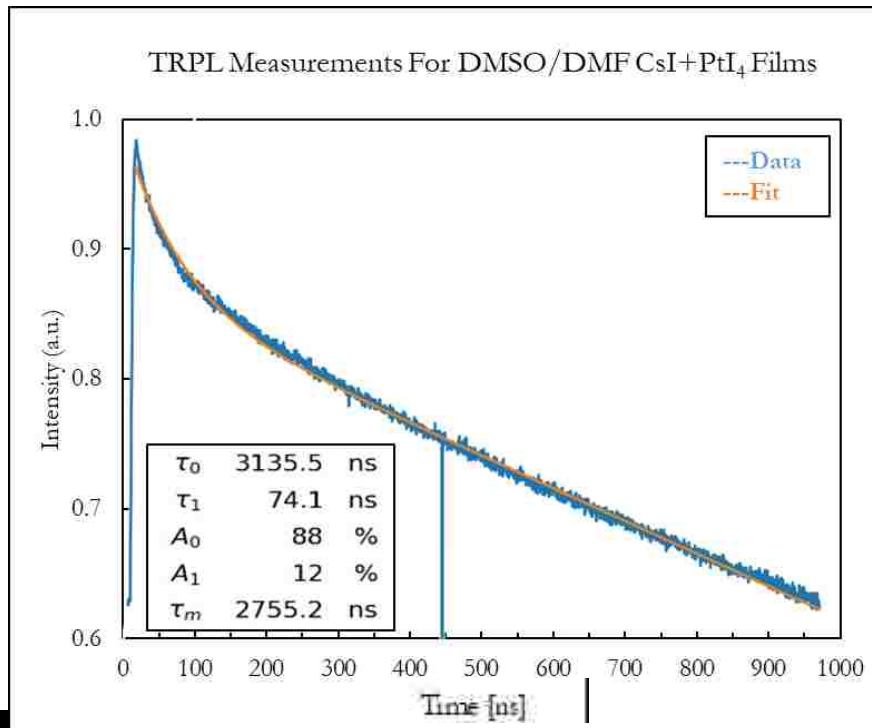
**Table 3: Statistics for four samples from different batches indicate low variation with a standard deviation of under 0.02 eV between measurements.**

Sample Name	Bandgap [eV]	
	Direct	Indirect
135	1.340	1.325
160	1.370	1.330
163	1.360	1.335
194	1.380	1.320
Average [eV]	1.363	1.328
Standard Deviation [eV]	0.0171	0.0065

For verification of bandgap and measurement of minority carrier lifetime, a  $\text{PtI}_4/\text{CsI}$  film sample was sent to Berkeley Lab's Molecular Foundry for PL and TRPL measurements. Room temperature PL shows a direct bandgap semiconductor with band-band transition at 1.4 eV or 880 nm. Bandgap measured by the two methods agrees well and the films exhibit absorption coefficient  $> 1e5 \text{ cm}^{-1}$ . The slight discrepancy between the two values can be attributed to the fact that film area measured by PL is much smaller than UV/Vis spot size and does not account for non-uniformities. In-depth bandgap mapping and correlation with composition variations are suggested as future work. In addition to verifying bandgap, the TRPL measurements indicate a minority carrier lifetime of 2.75  $\mu\text{s}$ , as shown in Figure 16. This is a very long lifetime, higher than reported 15  $\mu\text{s}$  for  $\text{MAPbI}_3$ , indicating large minority carrier diffusion length

(characteristic of indirect bandgap) in combination with high absorption coefficient (characteristic of direct bandgap) [41]. Further investigations are needed to understand the effect of spin-orbit coupling contribution to the superior properties of this material.





This material shows promising optical properties for thin film photovoltaics. A bandgap of 1.4 eV was determined using two methods: UV-Vis with Tauc plot analysis and photoluminescence completed at Berkeley Lab's Molecular Foundry. Furthermore, minority carrier lifetime is measured  $> 2.5 \mu\text{s}$ . A photovoltaic material of this bandgap is ideally suited for a single junction thin-film solar cells due to high absorption coefficient. Because of the high absorption coefficient and low sub-bandgap absorption, semi-transparent thin-films can be used a top cell in a tandem device with wider bandgap expected from substitution of X anion from I to Br to Cl.

### 2.1.2 Phase Identification

The predominant phase in this sample type is  $Fm\bar{3}m$  (cubic)  $Cs_2PtI_6$ , as expected from the idealized chemical formula. This was verified using powder XRD to find a sample pattern and comparing with computational patterns as shown in Figure 17 [42]. The complete data for the Topas Reitveld refinement is located in APPENDIX C. Figure 17 A depicts the raw pattern with a square root intensity y-axis with miller indices callouts at  $Cs_2PtI_6$  peaks matched using Topas Reitveld refinement and two raw  $CsI+PtI_4$  sample patterns. All  $Cs_2PtI_6$  peaks are present in the raw pattern. Peaks not matched are not likely to be cubic  $Cs_2PtI_6$ ; it is possible some of the peaks are a tetragonal  $Cs_2PtI_6$  phase. A comparison of the two raw patterns shows similar peaks with different peak heights but similar height proportions. Both patterns have low intensity peaks at two thetas of  $17^\circ$ ,  $41^\circ$  and  $51^\circ$  that are not associated with cubic or tetragonal  $Cs_2PtI_6$  phases which may indicate lattice defects, undissolved solvents, tertiary phase formation, or contaminants in the powder sample.

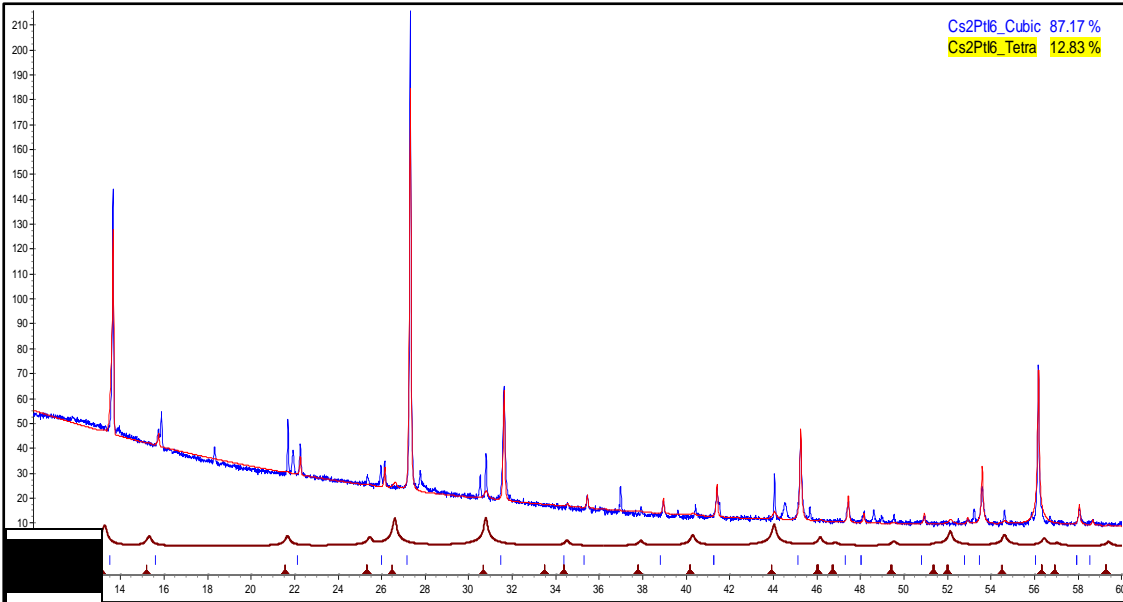
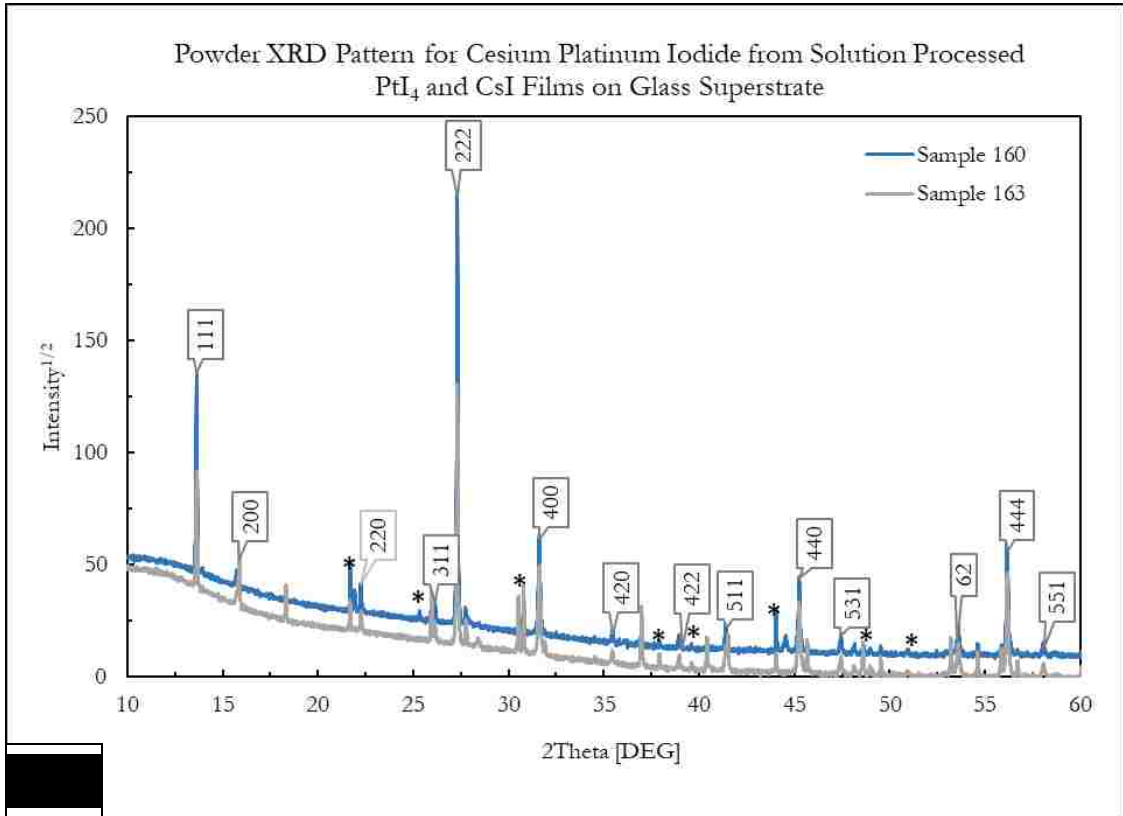
Figure 17 B depicts the Topas refinement of  $Fm\bar{3}m$  (cubic)  $Cs_2PtI_6$  with a tetragonal  $Cs_2PtI_6$  phase. The  $Fm\bar{3}m$   $Cs_2PtI_6$  phase was refined to a lattice parameter of 11.36 Å. The pattern shown in the figure, along with all other patterns from similar samples, show preferred orientation in the (111) and related planes; the reason for this is not yet understood but may be influenced by processing variables. However, it is common to both samples presented in Figure 17 as well as other similarly processed samples. The crystalline size parameters were increased due to refinement parameters near the maximum end of the scale. The final grain size was found to be 30,000 nm (30  $\mu\text{m}$ ) by Topas; this provides some verification to the largest crystals observed



using SEM of around 20  $\mu\text{m}$  (see Chapter 1). However, this was determined to be acceptable because the grain size as determined by Topas is of the correct magnitude.

No standard was used in this pattern and the precise peak location and lattice parameter may be off due to uncorrected displacement error. Running a similar sample with a standard may with phase identification and quantification significantly. A range of other phases including most available combinations of cesium, platinum, iodide, oxygen, and other common elements were attempted but did not reveal definite or likely phase matches.

Using powder XRD and Topas software for Reitveld refinement, cubic  $\text{Cs}_2\text{PtI}_6$  was determined to be the primary phase in the powder samples analyzed. The fit is consistent with the expected results and magnitude of grain size; however, unidentified phases (one or more) are present but account for low intensity peaks. Pattern results are relatively consistent in peak location, presence, and proportional intensity. The presence of tetragonal  $\text{Cs}_2\text{Pt}_6$  is not confirmed, however, a related structure type might be present. Further work is required for complete phase quantification.



### 2.1.3 Chemical Information

EDS methods were used to confirm the chemical content of films composed of PtI<sub>4</sub> and CsI. A ratio of 2 cesium: 1 platinum: 6 iodide is expected in the film based on the equivalent ratios of solutes used. Trace amounts of common elements such as nitrogen, oxygen, carbon, and sulfur may be present due to the solvents used and atmospheric processing. A range of spectrums were taken through the sample; the spectrum displayed in Table 4 was selected due to relatively high counts. There is an approximate ratio of 2.0 cesium: 1.0 platinum: 6.1 iodide at all sample spectrums measures. Some oxygen may be present. EDS measurements pick up 0-10% oxygen in the PtI<sub>4</sub>+CsI samples; this comes from oxygen in the sample, oxygen from the silicon dioxide substrate, and may be misattributed iodide M peaks (0.497 KeV) instead of oxygen K $\alpha$  peaks (0.523 KeV) due to high background at low energy levels. This data shows the ratio of elements is relatively constant across a film sample, indicating even phase formation of the Cs<sub>2</sub>PtI<sub>6</sub> phase.

**Table 4: Chemistry data from EDS testing methods computed using INCA software for PtI<sub>4</sub>+CsI material. No chlorine source was present during processing or storage and may be an error.**

	<b>Atomic %</b>	<b>Ratio to Platinum</b>
<b>Cesium</b>	19.5	2.0
<b>Platinum</b>	9.6	1.0
<b>Iodide</b>	58.4	6.1
<b>Oxygen</b>	9.1	possible contamination
<b>Chlorine*</b>	3.4	possible contamination

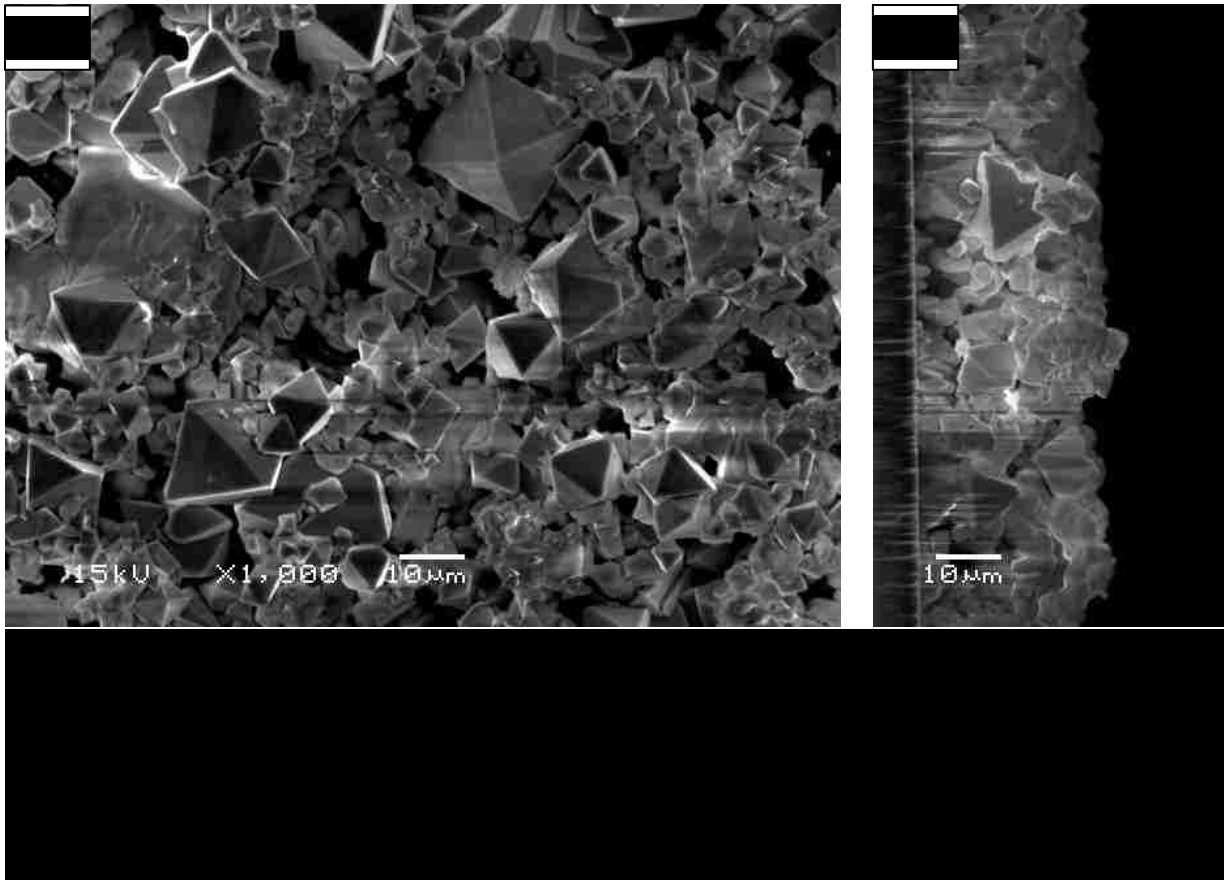
The amounts of cesium, platinum, and iodide are relatively consistent (within 10 atomic percent) within a single sample and between similar samples but the secondary elements are highly variable, even within a single sample. The presence of carbon was omitted from the table because the initial amount suggested by the INCA software (23.9%) is well above what is expected when comparing the sample to XRD data and likely carbon sources, other spectrums in the vicinity did not pick up carbon, and the UNLV EDS equipment and software currently has very high background apparent at low energies that can be mistaken for a Carbon  $K\alpha$  peak at 0.27 KeV. Preliminary secondary ion mass spectroscopy (SIMS) measurements (not presented upon here) confirm small amounts of contaminants including chlorine and sodium, although these elements are not directly added to the processing. It is possible that these elements emerge from impurities in the solvents (specifically DMSO) or are unintentionally included from the lab environment. Small amounts of elements including un-evaporated solutes, elements displayed in the table below, and light elements not picked up by EDS may be present in the sample and contribute to small amounts of non- $Cs_2PtI_6$  phases or defects.

#### **2.1.4 Morphology**

Films yielded from solution processing of  $PtI_4$  and  $CsI$  have a unique morphology. Using SEM, individual grains are visible with sizes ranging from 2-20  $\mu m$  and dispersed evenly throughout the film cross section, as seen in Figure 18. Surface and cross-sectional morphology are consistent with no evidence of more grain growth on the superstrate or surface. Large voids

between the grains exist. This grain formation was found to be independent of the deposition method used; spin coating deposition methods resulted in thinner films with a grainy appearance. Although the film appeared even immediately after the solution was deposited and spun, the outcome was concentrated grains with very large voids. As a result, these films were not fit for device fabrication. While the grain size itself may not be an issue, film synthesis without voids will be important for high efficiency devices. Additionally, a thin film of  $<1 \mu\text{m}$  cannot be synthesized from  $20 \mu\text{m}$  grains.

Since these cells are grown on an amorphous superstrate, it is hypothesized that the grains originate from the solution. Alternate deposition techniques may result in a different formation. Growing these films on a crystalline superstrate may encourage grain growth



### 2.1.5 Thermal Stability

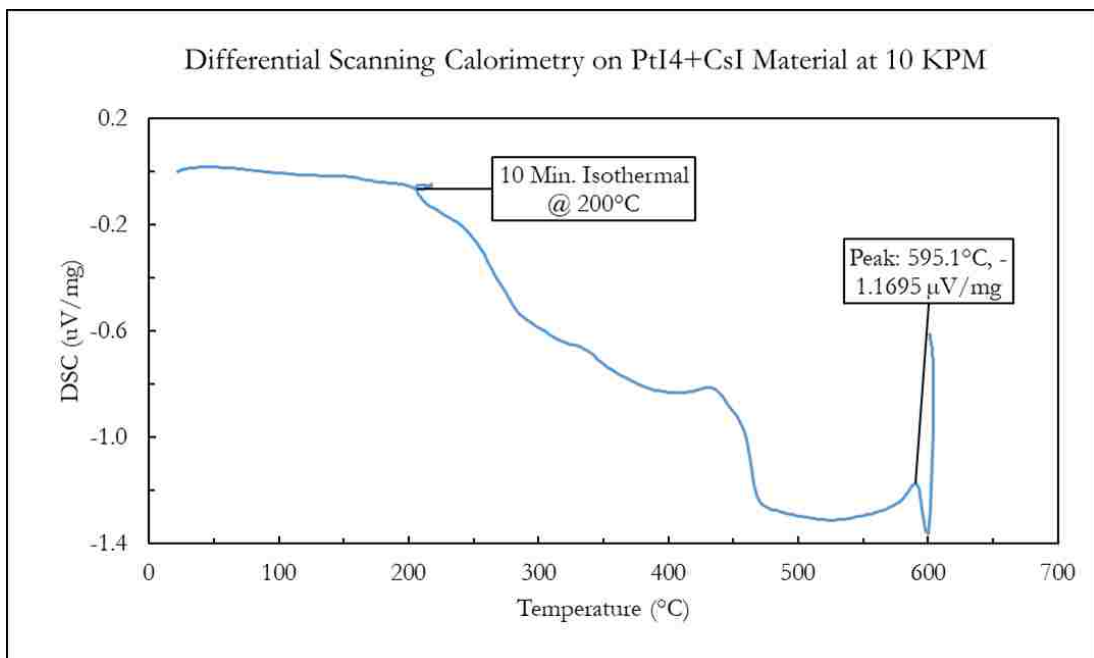
Thermal stability of photovoltaic materials is vital. Standard testing conditions of a cell are 25°C, however, non-shaded cells exceed the ambient temperature significantly. Using the Skoplanki model [43], as shown in Equation 8, a cell temperature can exceed 85°C on a very hot and windless day. The cell temperature may increase further depending on cell placement (i.e. rooftop solar on a dark roof with little space between cell and roof will increase the ambient temperature, thus increasing the cell temperature). Actual maximum cell operating temperature will depend on application. It is important that a solar cell designed for normal applications can withstand temperatures well above 85°C without degrading or otherwise becoming unstable.

**Equation 8: The Skoplanki model is one of many models used to determine cell temperature. It is relatively simple and accounts for irradiance, ambient temperature and wind speed. This model is used to demonstrate the difference between cell temperature and ambient temperature.**

$$T_{Cell} = T_{ambient} + \left( \frac{0.32}{8.91 + 2V_{wind}} \right) * G_{Solar\ irradiance}$$

In order to identify phase transitions, DSC measurements were performed on powder samples prepared with  $PtI_4$  and  $2CsI$ . These powder samples were prepared by annealing on a hotplate in a fume hood due to large amount of solvent evaporation for bulk samples. As the sample increases in temperature, the voltage to keep the sample at a higher temperature tends to increase. However, there are no endothermic or exothermic peaks below  $500^\circ\text{C}$ , indicating no phase changes below that point. A possible peak around  $590^\circ\text{C}$  indicates a possible phase change; however, a future test needs to be conducted past  $600^\circ\text{C}$  with appropriate isothermals to verify the precise location of this peak. Results from the  $600^\circ\text{C}$  test are shown in Figure 19. The mass of the sample was found to be constant for the duration of the test. Thermally stability past  $500^\circ\text{C}$  is promising compared to  $MAPbI_3$  which has a tetragonal to cubic phase transition at  $58^\circ\text{C}$  [44]. Only one sample has been tested using DSC thus far, and repeat measurements will be conducted to temperature beyond  $600^\circ\text{C}$  to confirm the peak at  $590^\circ\text{C}$ . As large amount of powder is needed for DSC measurements, variation to the thin-film process was made. Temperature dependent XRD may be more suitable to determine the stability of these materials.

Modifications to normal processing needed to be made to increase sample thickness; the coloration and consistency of the resulting thicker sample indicate the similar formation of  $\text{Cs}_2\text{PtI}_6$ . Future testing should be done to verify the same percentage of phase synthesized. An aluminum oxide sample holder was used which has reduced heat capacity from metal sample holders. Once it can be determined the material does not react with a platinum sample holder, a platinum sample holder should be used for more accurate testing.





## 2.1.6 Summary of Results of Cesium Platinum Iodide Material from $\text{PtI}_4$ and CsI in DMF/DMSO

The material resulting from solution processing of CsI  $\text{PtI}_4$ , DMF, and DMSO has consistent results while using the same processing methods; the synthesized material is black large crystals of  $\text{Cs}_2\text{PtI}_6$ . The absorption coefficient is  $> 1.5 \times 10^5 \text{ cm}^{-1}$  at 1.75 eV which is 10x of  $\text{MAPbI}_3$ , which makes  $\text{Cs}_2\text{PtI}_6$  ideally suited for thin film photovoltaic absorbers. However, further research is needed to make compact void-free thin-film samples of  $\text{Cs}_2\text{PtI}_6$ . Thin-film samples show an optical bandgap of about 1.3-1.4 eV and minority carrier lifetime of 2.7  $\mu\text{s}$  which is incredibly promising. Using powder XRD,  $\text{Cs}_2\text{PtI}_6$  is confirmed to be the primary phase with small amounts of other unidentified phases present. Chemical information obtained using EDS methods confirm the correct cesium platinum iodide ratio for  $\text{Cs}_2\text{PtI}_6$  with possible contaminants including elements present in the solvents. Cubic crystals are visible using SEM imaging; evenly distributed grain sizes of 2-20  $\mu\text{m}$  make up the surface and cross section of the film with numerous voids. This presents an issue for thin film devices; processing methods will need to be altered to address the voids and very large grains.  $\text{Cs}_2\text{PtI}_6$  has promising thermal stability with no suspected phase changes below 500 °C. These results indicate  $\text{Cs}_2\text{PtI}_6$  can be used as an absorber layer and alternate processing methods and device structures need to be developed.

## 2.2 Platinum Di-iodide and Cesium Platinum Iodide Derived Perovskites Synthesis

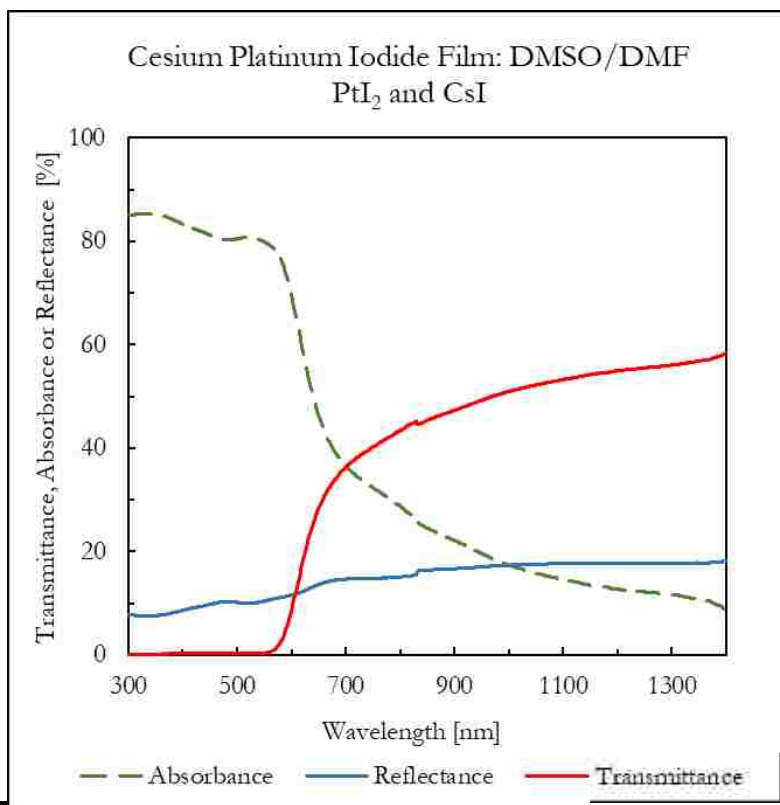
Perovskite materials made using platinum(II) iodide and cesium iodide follow the process procedure provided in the methodology section. It was determined these solutes dissolve well in a 50/50 combination by volume of the solvents DMSO and DMF and regularly produce films with an observable optical bandgap. The reasons for this can be determined in further work. Combinations including GBL alone, DMF alone and combinations of GBL and DMF resulted in grayish films with no to little bandgap presence using UV-vis spectroscopy. Further work with solvents may yield interesting results. Only materials produced using DMF/DMSO and  $\text{PtI}_2 + \text{CsI}$  are discussed in this section.

The  $\text{PtI}_2$  and  $\text{CsI}$  solute combination processed in 0.25-0.4M DMF/DMSO solution and deposited using doctor blade methods. Spin coating was done and is discussed but doctor blade methods yielded consistent results and was found to be more reliable for film characterization methods. An image of a typical film can be found in Figure 20; all similar materials appear red and are well adhered to the glass or glass coated superstrate. 100% of samples made using this method were observably similar to the figure image.

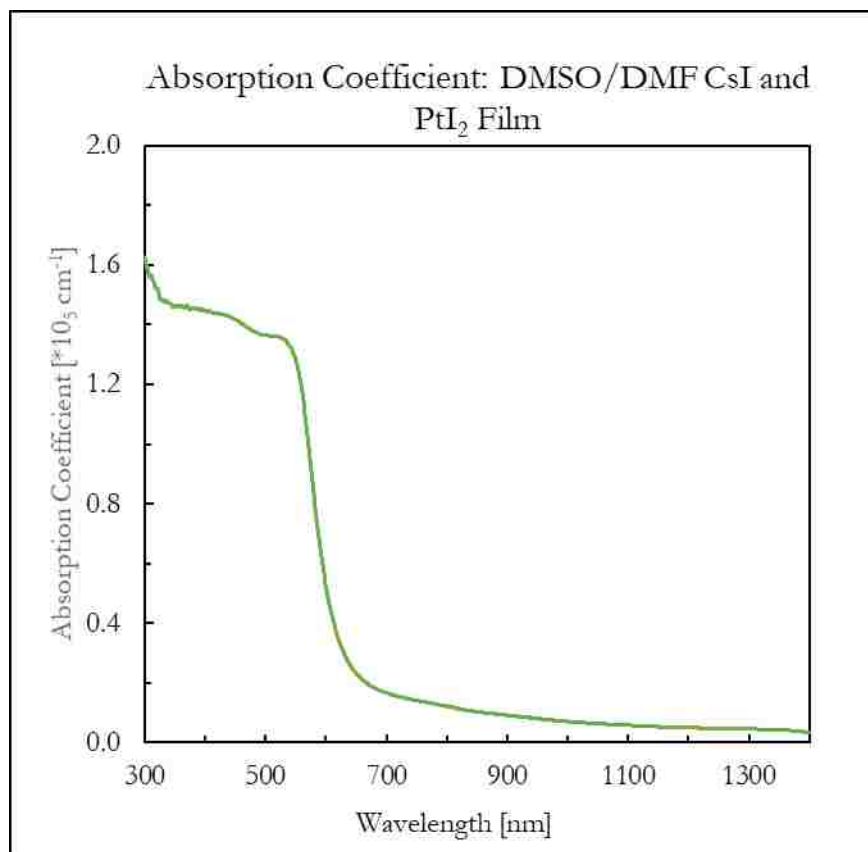


### 2.2.1 Optical Properties and Bandgap Determination

The using UV-Vis spectroscopy, transmittance and reflectance measurements made from wavelengths ranging from 300 to 1400 nm on a film sample deposited on a glass superstrate. As observed in Figure 21, the transmittance and reflectance are relatively low (<10%) for lower wavelength, higher energy photons. Using the methods and equations described in Chapter 1, the absorbance was calculated using transmittance and reflectance data. The resulting absorbance is high (>80%) for wavelengths below about 600 nm.



Using the transmittance and reflectance, the absorbance coefficient was calculated for the range of measurements given as seen in Figure 22. The absorbance coefficient is a measure of how much light of a certain wavelength is absorbed by a certain thickness of the material; this material has relatively high absorbance and absorption coefficient. Additionally, this material has a prominent absorption edge at about 600 nm, indicating much of the light below this wavelength is absorbed by the material. Comparison to other perovskite materials can be found in Chapter 3.

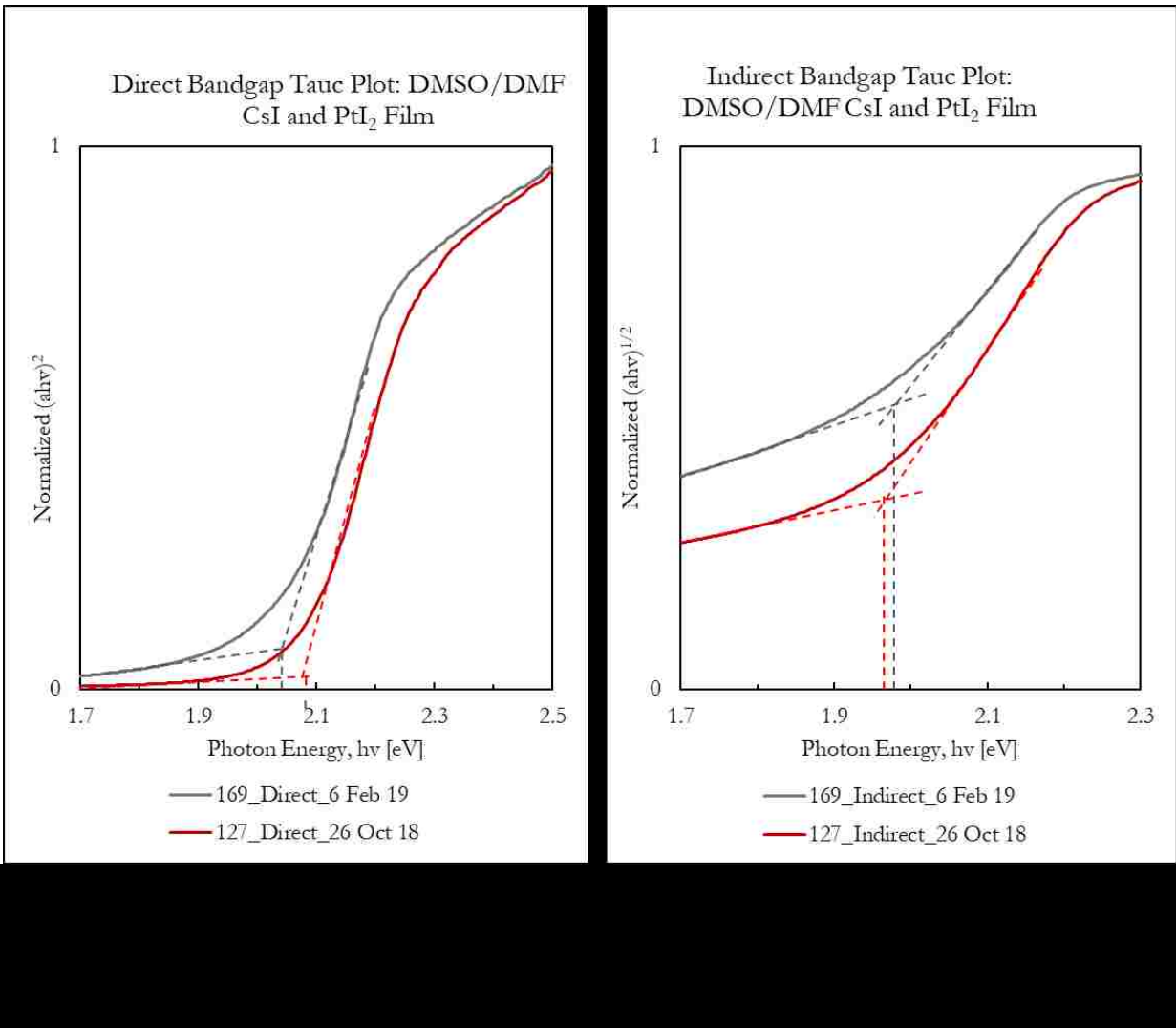


The Tauc method can be used to determine the material's optical bandgap. A direct bandgap is estimated by computational studies for the Cs<sub>2</sub>PtI<sub>6</sub> material [26]. Both indirect and direct Tauc methods are used to evaluate the material band gap. The indirect and direct bandgap Tauc plots with linear approximation of the bandgap can be found in Figure 23 for two film samples from identical processes occurring on separate days. The direct bandgap as determined by UV/Vis Tauc is slightly below 2.1 eV; the indirect bandgap for this material is slightly above 1.9 eV.

These results indicate possible indirect bandgap absorption and leave questions about the composition of the absorber material.

These results are not in agreement with the direct bandgap estimate for  $\text{Cs}_2\text{PtI}_6$  published in 2018 by Cai et al. (1.340 eV–1.472 eV, respectively with and without spin orbit coupling) [26].

This indicates that the absorber material synthesized from  $\text{PtI}_2$  and  $\text{CsI}$  is not  $\text{Cs}_2\text{PtI}_6$ , particularly when compared to the experimental results immediately before this section. Rather, the material must be composed of cesium, platinum, iodide and/or elements from the solvent or atmosphere. However, the high absorption coefficient and bandgap are adequate for use in photovoltaic absorber materials and warrant further study.



The variations between samples is relatively low. Samples from four batches synthesized from July 2018 through February 2019 indicate an average indirect bandgap of 1.94 eV and an average direct bandgap of 2.05 eV, as demonstrated in Table 5. The standard deviation of 0.0239 eV (indirect) and 0.0354 eV (direct) are indicate some variation between batches. By observation, the sample data is similar with no other major bandgaps or absorption edges apparent;

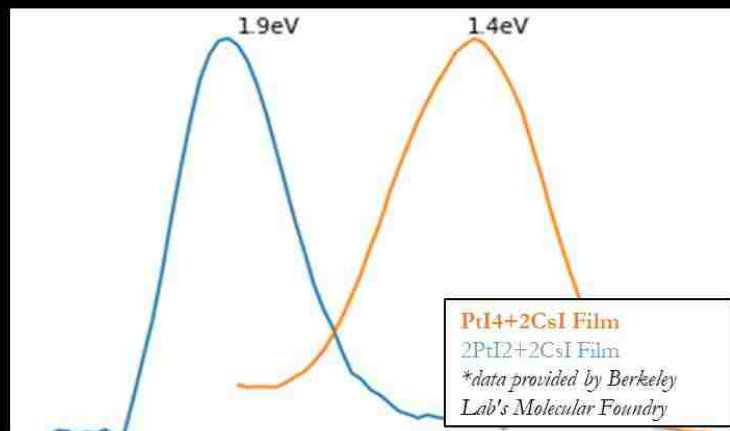
however, significantly more variation is present compared to the previously discussed samples synthesized from CsI and PtI<sub>4</sub>. The amount of observable and calculated variation do indicate this material synthesis is repeatable, although some variation in composition or morphology may result in alterations to the bandgap.

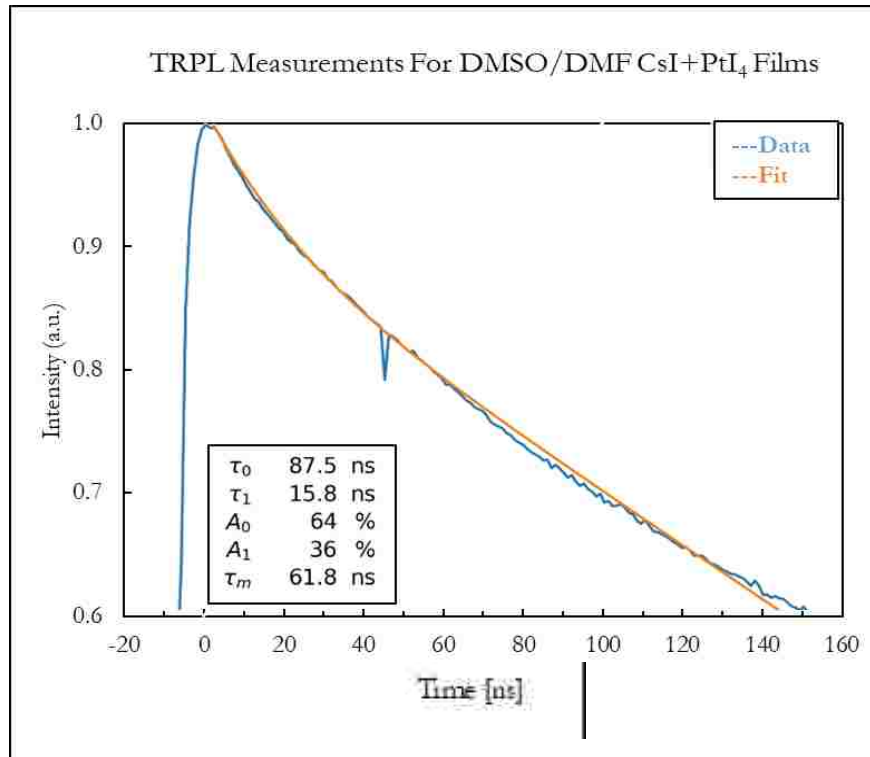
**Table 5: Statistics for four samples from different batches indicate some variation with a standard deviation of under 0.04 eV between measurements.**

Sample Name	Bandgap [eV]	
	Direct	Indirect
<b>124</b>	2	1.925
<b>127</b>	2.075	1.95
<b>169</b>	2.05	1.975
<b>187</b>	2.075	1.925
<b>Average [eV]</b>	2.05	1.94
<b>Standard Deviation [eV]</b>	0.0354	0.0239

For verification of material and methods used, a PtI<sub>2</sub>/CsI film sample was sent to Berkeley Lab's Molecular Foundry for photoluminescence measurements. The photoluminescence peak is observed at 620 nm corresponds to a bandgap of 1.9 eV, as shown in Figure 24. The slight disagreement between UV/Vis measurements and PL measurements might be due to the methods used to determine the bandgap, resolution of the PL measurements, or sample variation. However, these two methods are close enough to verify the existence of a bandgap near 1.9-2.1 eV. In addition to verifying bandgap, the TRPL measurements indicate a minority carrier lifetime of 61 ns, as shown in Figure 25.







Thin-films prepared with PtI<sub>2</sub> + CsI precursors exhibits good optoelectronic properties suitable for multi-junction solar cell. These thin-films also show high absorption coefficient and low sub-bandgap absorption making them suitable for wide bandgap top cell for Si or CIGS bottom cells.

## 2.2.2 Phase Identification

Due to consistent optical bandgap findings of 1.9-2.1 eV, verified using two methods, as well as a highly repeatable absorbance edge, a perovskite structure is expected in this material.

However, the material appears more reddish than black and bandgap is increased significantly from the verified  $\text{Cs}_2\text{PtI}_6$  phase synthesized using  $\text{PtI}_4$  as the platinum source. Additionally, excess platinum from the solute ratio of  $2\text{CsI}$  and  $2\text{PtI}_2$  must result in the presence of at least two phases if any of the  $\text{Cs}_2\text{PtI}_6$  is present. The increased bandgap of the  $\text{PtI}_2$  materials could have multiple causes: (1) the material could be formed into a non-cubic  $\text{Cs}_2\text{PtI}_6$  phase, possibly by interstitial platinum atoms (which are relatively large). (2) Defect introduced from the atmosphere or solvents might be part of a cubic or non-cubic perovskite-type material, thus increasing the bandgap and increasing the structure complexity. (3) The perovskite may be forming as a secondary or tertiary phase with the bandgap increased due interactions with the surrounding phase.

In order to evaluate the sample composition and increased bandgap, power XRD analysis was performed on a sample composed with solution processing of  $\text{PtI}_2$  and  $\text{CsI}$  solutes in DMF/DMSO solvents. The pattern results are more complex than those of samples composed using similar processing with a  $\text{PtI}_4$  platinum source and do not immediately confirm any of the above hypothesizes. All  $\text{CsI}+\text{PtI}_2$  samples created have similarities in the bandgap (1.9-2.2 eV) and optical properties and visually appear similar. The XRD patterns share some similarities but have much greater variation as opposed to the patterns resulting from a  $\text{PtI}_4$  platinum source. One of the more common pattern trends is shown with less common patterns discussed.

The pattern resulting from Figure 26 is represents a common group of patterns, with some consistency in peak locations but considerable proportional peak height variation. Figure 26 A

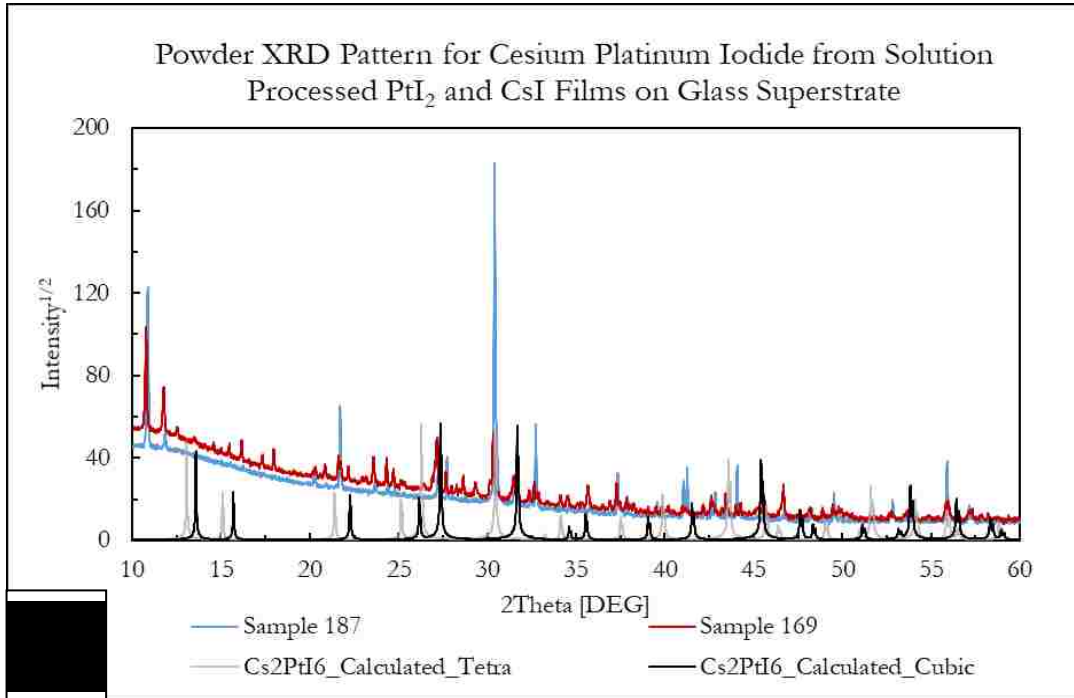
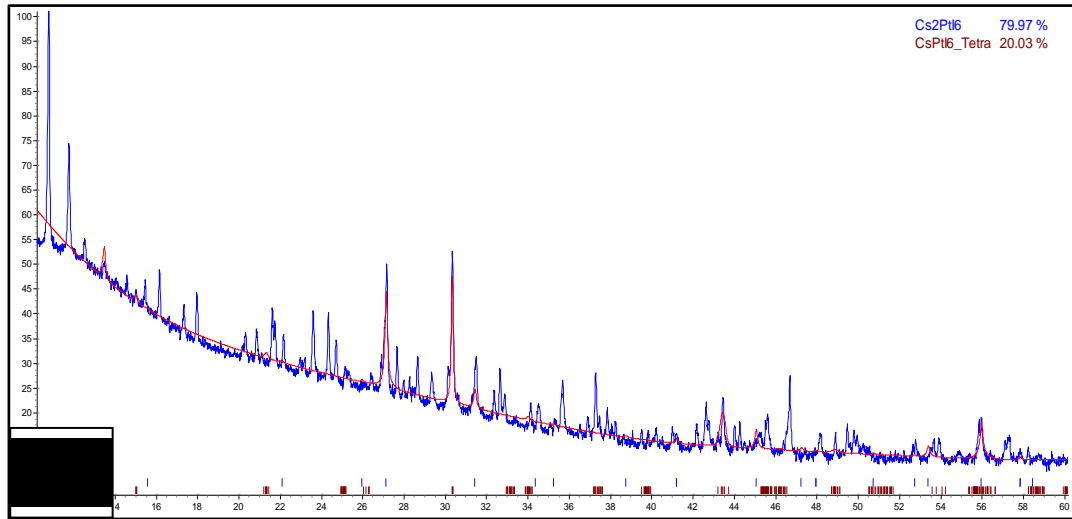
depicts the attempted fit of a typical pattern using Topas for Reitveld refinement.

Computational cubic and tetragonal phases  $\text{Cs}_2\text{PtI}_6$  phases were found to be the best match to the pattern of any other cesium platinum iodide and other common elements patterns attempted [42]. While  $\text{Cs}_2\text{PtI}_6$  might account for some of the phase present, this sample type is not a full match to either the cubic or tetragonal  $\text{Cs}_2\text{PtI}_6$  phase. Other possible phases attempted did not fit well. Initial results using ICDD's PDF-4 database showed possible match to a cubic  $\text{Pm}\bar{3}\text{m}$   $\text{CsGeI}_3$  phase; however, it was determined by research partners at the Technical University of Denmark that the  $\text{CsPtI}_3$  phase is likely metallic in nature and would not have the appropriate lattice parameters for a pattern match.

Figure 26B show the same pattern as Figure 26A (red) with an additional raw pattern (blue) with fewer and more intense peaks. While the cubic and tetragonal  $\text{Cs}_2\text{PtI}_6$  phases are a plausible match, many peaks are unaccounted for including two prominent peak at  $11^\circ$  and  $14^\circ$  two theta values. The additional pattern has fewer peaks and lacks the prominent (111) and (222) peaks ( $14$  and  $27^\circ$  two theta, respectively) expected for the  $\text{Cs}_2\text{PtI}_6$  phase. This blue pattern was not an obvious match to any other phase using Topas and Eva but is an example of the variation within the CsI and  $\text{PtI}_2$  samples. Other less frequent patterns have very intense peaks at  $39.5^\circ$  and  $85^\circ$  two thetas, corresponding to the 111 and 222 planes expected for platinum. This is interesting because there is extra platinum within the sample. However, this pattern type is not frequent and only appeared in one sample batch.

Further analysis may be done to better determine lattice parameters and preferred orientation, resulting in a better fit. However, even if the  $\text{Cs}_2\text{PtI}_6$  phase is a match, the two very prominent

peaks two thetas of  $10.8^\circ$  and  $11.8^\circ$  are unaccounted for. Many patterns for combinations of cesium, platinum, iodide, oxygen and other common elements were attempted and not found to be good fits using Topas software. Before any phases can be eliminated, a standard should be included in this sample. If matches remain scarce, it is possible this sample is composed of a phase not available in the databases used. However, the initial match with  $\text{Cs}_2\text{PtI}_6$  and other material properties indicates some version of perovskite exists in this sample.



### 2.2.3 Chemical Composition

EDS methods were used to confirm the chemical content of films composed of  $\text{PtI}_2$  and  $\text{CsI}$ . A ratio of 1 cesium: 1 platinum: 3 iodide is expected in the film based on the equivalent ratios of solutes used. However, if the  $\text{Cs}_2\text{PtI}_6$  phase were to form, pockets of a different ratio is possible. Trace amounts of common elements such as nitrogen, oxygen, carbon, and sulfur may be present due to the solvents used and atmospheric processing. A range of spectrums were taken through the sample; the spectrum displayed in Table 6 was selected due to relatively high counts. There is an approximate ratio of 1.0 cesium: 1.0 platinum: 3.5 iodide at all sample spectrums measures. It is unclear where the excess iodide might originate as a ratio of 1 cesium: 1 platinum should result in 3 iodide due to the solutes used. This excess of iodide may indicate an excess of platinum or cesium or a decrease of iodide at some sample locations. Preliminary calculations show  $\text{CsPtI}_3$  is metallic, however, the effect of oxygen needs to be explored. The 1:1:3 phase containing oxygen has been shown to be p-type in this experimental work and needs to be further studied. There are no reports on  $\text{CsPtI}_x\text{O}_y$  halogen-chalcogen semiconductors, but the promising initial results here warrant further research into this material.

Some oxygen is present and may account for 22.4% of the atoms in the sample. As noted in the methodology section, EDS is not the best method to determine concentrations of light elements such as oxygen. However, there is a consistent increase in oxygen between the materials composed from  $\text{PtI}_2$  (15-30%) as compared to  $\text{PtI}_4$  (0-10%) for materials near the same thickness.

It is possible an increase in oxygen concentration is responsible for the significant differences between the materials synthesized from PtI<sub>4</sub> and PtI<sub>2</sub>.

Small amounts of elements including un-evaporated solutes, elements displayed in the table below, and light elements not picked up by EDS may be present in the sample and contribute to additional phases and defects. The excess of iodide and significant oxygen presence are likely key in determining the absorber material and other phases present.

**Table 6: Chemistry data from EDS testing methods computed using INCA software for PtI<sub>2</sub>+CsI material.**

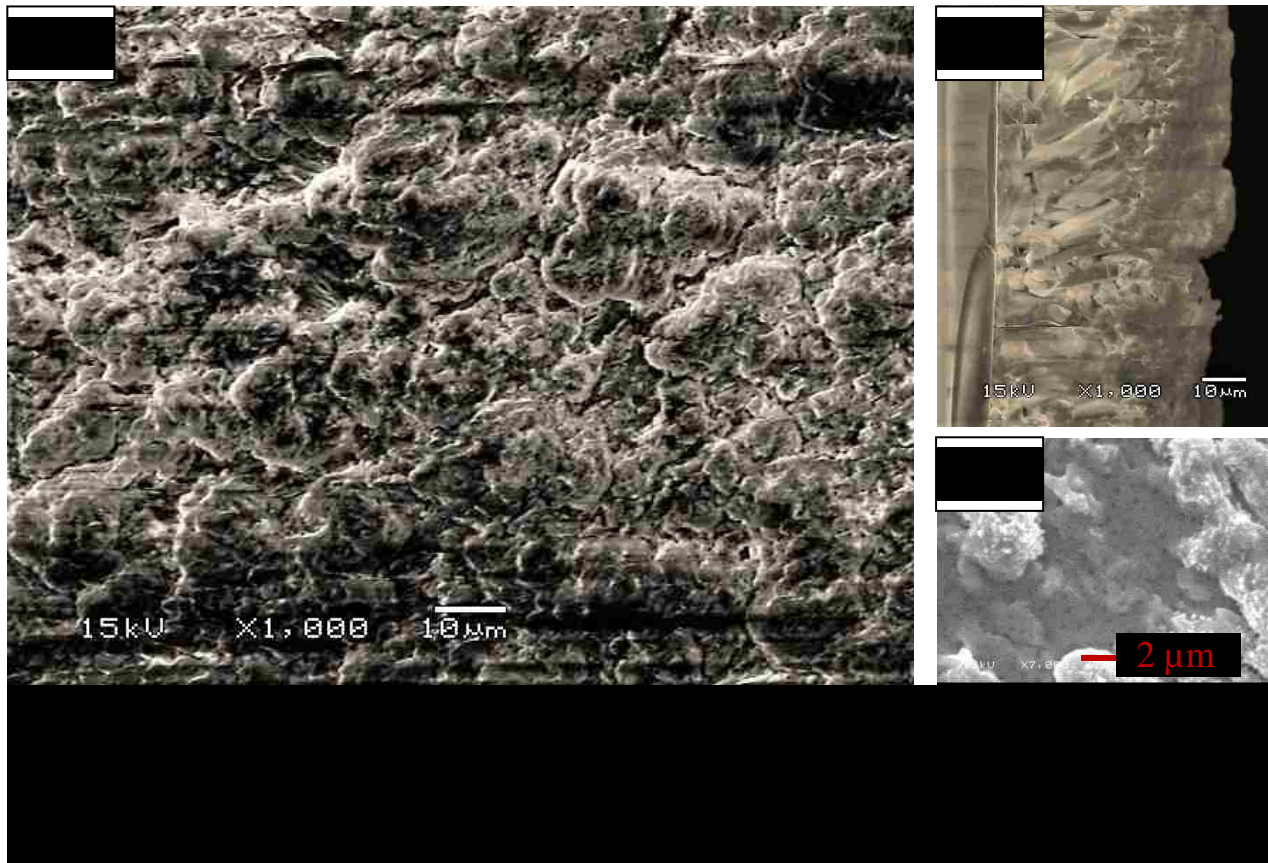
	Atomic%	Ratio to Platinum
<b>Cesium</b>	14.3	1.0
<b>Platinum</b>	14.0	1.0
<b>Iodine</b>	49.3	3.5
<b>Oxygen</b>	22.4	

## 2.2.4 Morphology

The perovskite material composed of CsI and PtI<sub>2</sub> results in a film with an uneven surface with a layered cross section. There is a significant amount of variation in morphology of these samples, although they all appear reddish and look visually similar. Figure 27 shows typical film morphology, with less typical morphology discussed in subsequent sections. Figure 27 A shows the uneven surface at X1000 with no visible grains (unlike the PtI<sub>4</sub> Cs<sub>2</sub>PtI<sub>6</sub> samples).



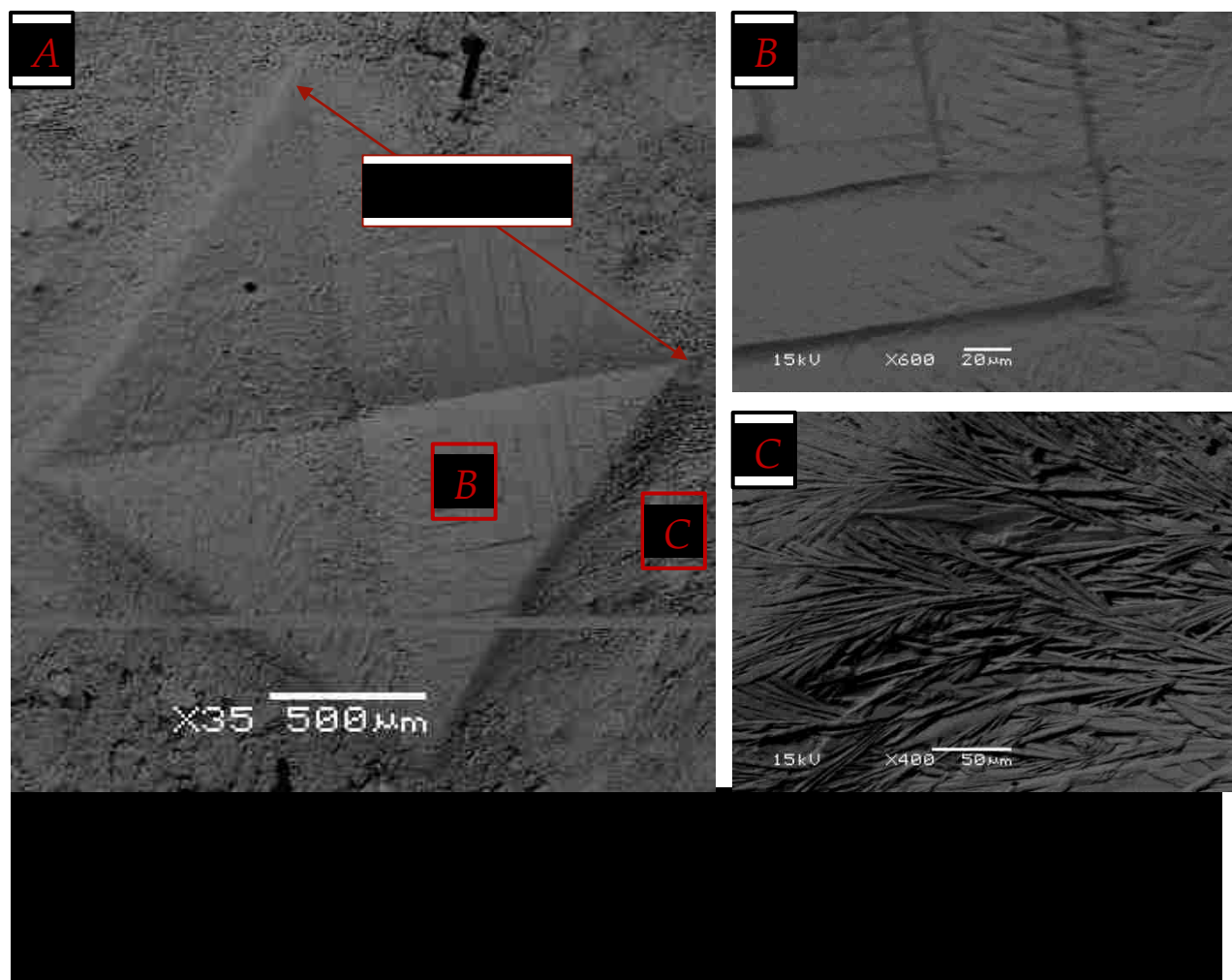
Figure 27 B shows a cross section of the same sample as A; two layers are evident with grain growth near the superstrate surface and less formed material near the top layer. Figure 27 C shows a different but similar sample at a higher magnification. Pin holes are evident on the sample surface.



Synthesizing this material on a crystalline surface may encourage grain growth. Unlike the  $\text{PtI}_4$  sample, grains are smaller and more cohesive with less void space. This is likely better for photovoltaic application. The effect of spin coating on film morphology is discussed in a subsequent section.

### **2.2.5 Crystal Formation in Platinum Cesium Iodide Perovskite**

In February of 2019, multiple sample batches of PtI<sub>2</sub>+CsI perovskite were synthesized with the formation of visible crystals of possibly Cs<sub>2</sub>PtI<sub>6</sub> due to morphology and limited chemical data. These films are deposited on an amorphous SiO<sub>2</sub> glass surface. Due to lattice mismatch between the cubic crystalline structure from the solution and the amorphous substrate, it is hypothesized this crystal formed within the solution. The accidental formation of crystals measuring 0.5-2.0 mm in width indicates the possibility of growing sizable single crystals, given the proper growth conditions. These crystals were further investigated using SEM and EDS techniques. A larger crystal and surrounding film are depicted in Figure 28. Corresponding EDS information is located in Table 7, with the full EDS report located in APPENDIX D.



The solutes used in this film (see Equation 2 in methodology) has an atomic percentage ratio of 1:1:3 (cesium: platinum: iodide). For a homogenous solid solution film, this ratio would be expected. However, a ratio of nearly 2:1:6 is found at the site of the crystal with no or very little other elements present. This chemistry combined with the square formation indicates the formation of the  $\text{Cs}_2\text{PtI}_6$  phase. Other phase identification methods could not be performed on this sample due to the crystal size and project timeframe. The surrounding film with a dendritic structure has chemical results closer but not equivalent to the 1:1:3 ratio expected with significant presence of contaminants including oxygen and sulfur (likely from the solvents

used) and gold (from thin coating facilitating conductivity for SEM imaging); other contaminants recommended by the INCA software may or may not be present but have no likely source. Variables such as film smoothness effect the EDS analysis accuracy; this may result in the dendritic structure with a cesium platinum iodide ratio nearer to 1:1:3.

**Table 7: EDS data from the sample pictures in Figure 28. The cubic crystal information corresponds to site B, while the dendritic information corresponds to site C.**

Element	Cubic Crystal		Dendritic	
	Atomic %	Platinum Ratio	Atomic %	Platinum Ratio
<b>Cesium</b>	21.0	1.8	12.6	0.8
<b>Platinum</b>	11.8	1.0	15.4	1.0
<b>Iodine</b>	67.2	5.7	52.6	3.4
<b>Other</b>	None		S (19%)	
<b>Cs:Pt:I Ratio</b>	2: 1: 6		0.8: 1.0: 3.4	

The processing variables required to produce these crystals are not yet understood. Using a crystalline superstrate may facilitate crystal growth for initial study.

### **2.2.6 Effect of Deposition Method on PtI<sub>2</sub> CsI Material**

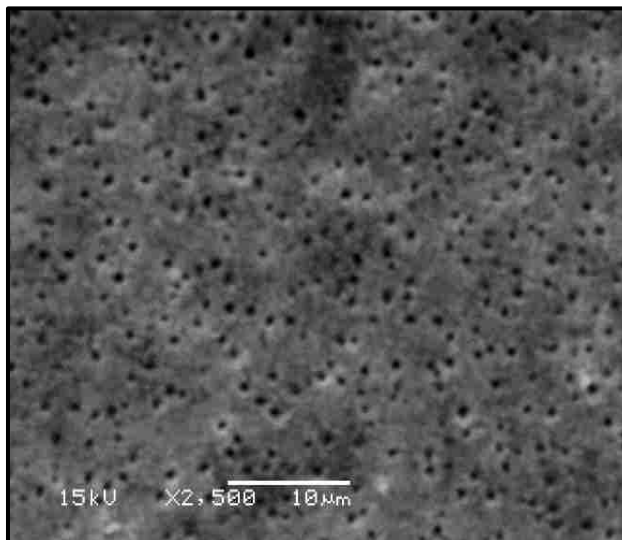
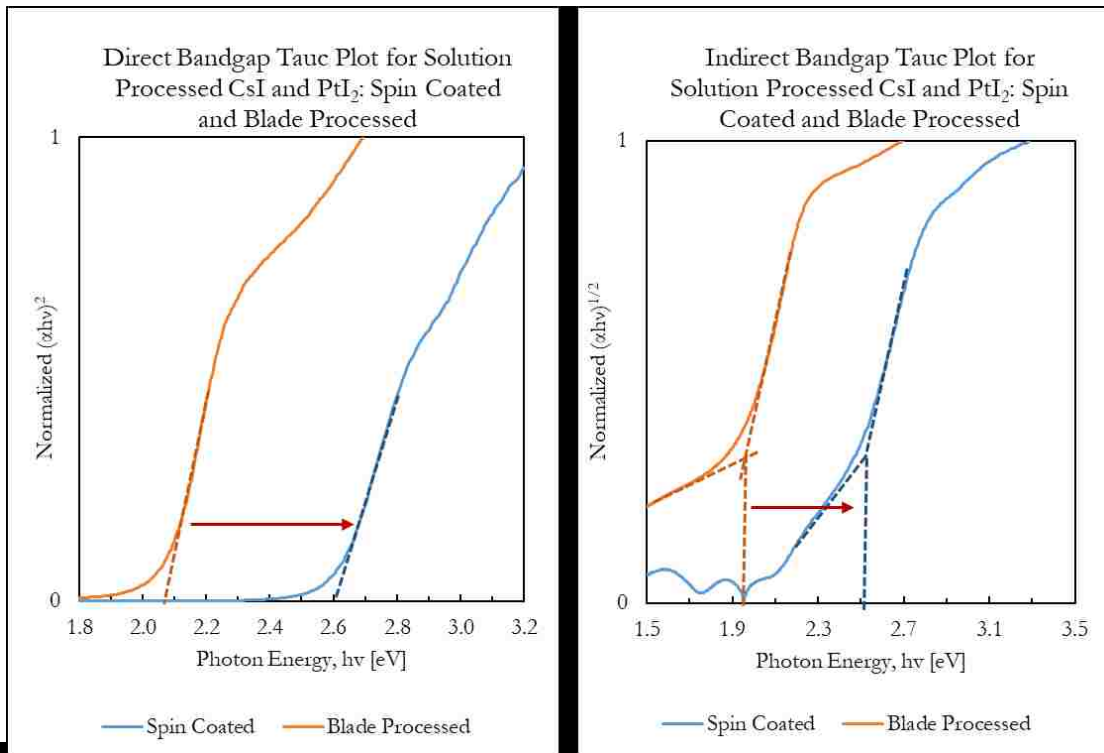
The deposition method has a large effect on the material synthesized, holding all other variables constant with the exception of annealing time. Two deposition methods were used: doctor blade and spin coating. These methods are described in greater detail in the methodology section. The reasons behind these material differences are not understood but are relevant to phase

identification and future processing methods. The differences in doctor-blade deposited materials and spin coated materials are outlined below:

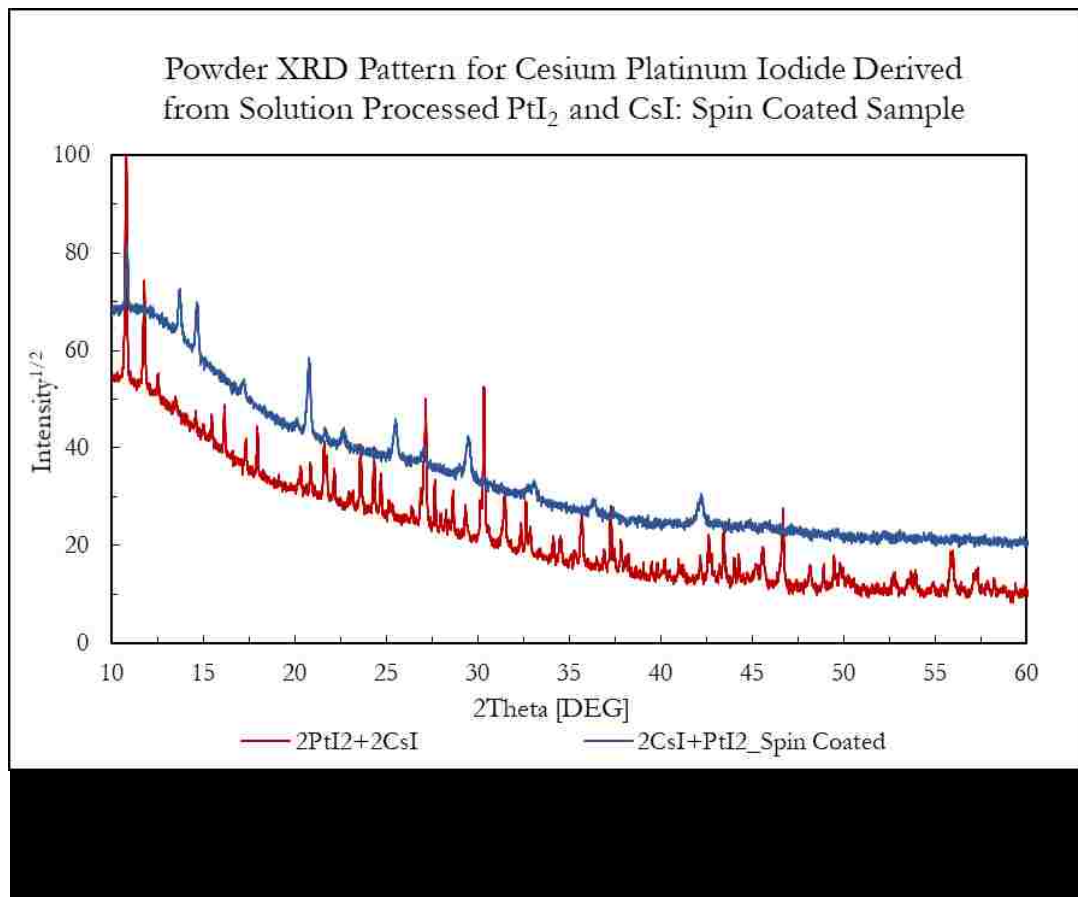
- These two films are visually different. As the layer becomes thinner, the film turns from a reddish black color to an orange color, as shown in Figure 29.



- The bandgap increases as from around 2.0 eV to around 2.6 eV. This bandgap increase is significant; a 1.9-2.0 eV semiconductor would be useful for wide bandgap photovoltaic applications. A 2.6 eV bandgap semiconductor would be able to absorb only a small portion of sunlight and will be much less useful. Figure 31 shows the effect of processing methods on the material bandgap.
- The surface becomes smoother and more evenly distributed. This is expected for spin coating methods and should be beneficial for a thin film photovoltaic material. The surface does have pin-holes which may be reduced by altering processing methods. Figure 30 shows the surface of a spin coated film and can be compared with Figure 27 A and C for blade processed films.



- There is a significant difference in phase presence between the blade processed and spin coated phases, although none of the phases have been successfully identified. The samples do share the most intense peak at 10.89 degrees and the peaks present in the spin coated sample are present in the doctor blade sample although generally less intense, as displayed in Figure 32. The spin coated sample has fewer visible peaks which generally have larger widths. This is likely due to decreased grain size. It is unclear if the spin coated samples contain an entirely different phase or one type has increased defects or substitutions.



This information is included because this material will likely be most efficient as a thin film material. However, most testing was completed on blade processed, thicker samples. Both film types have attributes important to the function of photovoltaic devices. The effect of processing methods is very important. These two material types raise a number of questions:

- What is the structure and chemistry of the 2.0 eV and 2.6 eV absorber?
- Does some amount of the phase found in the spin coated sample exist in the top layer of a blade processed sample?
- How can a thin film  $\text{PtI}_2$  CsI device with a 2.0 eV bandgap be synthesized?
- Is the difference in bandgap related to the oxygen content? If so, how does this relate to the  $\text{Cs}_2\text{PtI}_6$  material synthesized with  $\text{PtI}_4$ ?

Further discussion is provided in the Chapter 4.

### **2.2.7 Summary of Results of Cesium Platinum Iodide Material from $\text{PtI}_2$ and CsI in DMF/DMSO**

The material resulting from solution processing of CsI,  $\text{PtI}_4$  in DMF and DMSO has consistent results while using the same processing methods; the synthesized material is red and well adhered to the superstrate. The absorption coefficient is  $> 1.5 \times 10^5 \text{ cm}^{-1}$  at 1.75 eV making it a suitable candidate as a thin film photovoltaic absorber. Film samples show an optical bandgap of about 1.9-2.1 eV using multiple measurement techniques. Additionally, preliminary minority carrier lifetime estimates of 61 ns are sufficient for photovoltaic applications. Using powder XRD, it is determined this material does not match the computational  $\text{Cs}_2\text{PtI}_6$  phase used in the



previous section. Further, the pattern does not match likely cesium, platinum, iodide and/or common element phases. Chemical information obtained using EDS methods confirm indicate a cesium platinum iodide ratio near the solute input with a significant oxygen presence (>20 atomic%). SEM shows a morphology with an uneven surface and two distinct layers: grain growth on the substrate surface covered by less crystallized material. Pinholes are present but the film is free of large voids.

The presence of what are likely large (0.5-2.0 mm)  $\text{Cs}_2\text{PtI}_6$  crystals are possible in this material; although the conditions for their appearance is not understood, this indicates it may be feasible to produce large single crystal  $\text{Cs}_2\text{PtI}_6$  specimens and the formation of  $\text{Cs}_2\text{PtI}_6$  is possible using  $\text{PtI}_2$  in the correct processing conditions. The film result is dependent on the deposition method which is important for transitioning from material synthesis to device fabrication. This material type is determined to be repeatable although larger amount of variation are found in the bandgap, phase presence, morphology and visible appearance (i.e. visible crystals) as compared to the material formed by  $\text{CsI}$  and  $\text{PtI}_4$ . This material has many positive attributes for solar cell application, although a greater understanding is necessary for successful implementation.

## **2.3 Cesium Platinum Iodide Photovoltaic Device Fabrication and Performance**

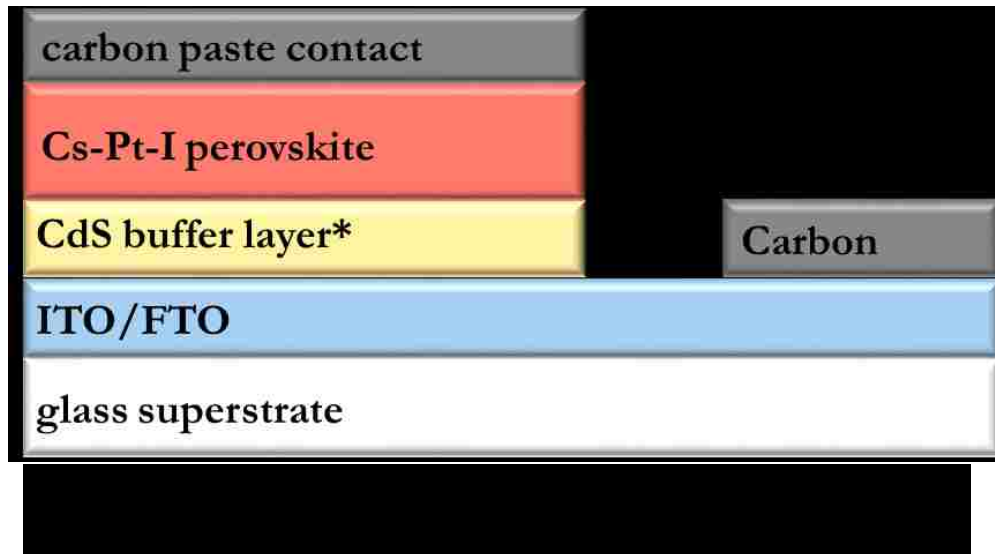
The ultimate goal of this research is to fabricate functional thin-film cesium platinum iodide perovskite photovoltaic devices. This goal remains unachieved; devices fabricated during this effort leave much to be desired, including a photovoltaic response to light. However, the results and analysis of the devices made, including dark current-voltage response and capacitance-voltage response. Hypothesis is provided for the minimal to non-existent photoelectric response with ideas for future device improvement.

### **2.3.1 Devices Tested**

Six device types were tested, as detailed in Table 8 and Figure 33. All devices presented upon have a doctor-blade deposited perovskite layer 20-30  $\mu\text{m}$  thick. Further information about device fabrication and the absorber layers used is located in the previous sections. The devices discussed in this section are not thin film devices. All are fabricated on a conductive metal oxide with or without a buffer layer. Positive and negative contacts are made using carbon paste with conductive tin aluminum tape used as positive and negative leads. Future fabrication technique improvement could result in significant device performance improvement.

**Table 8: Device type summary with layer composition.**

Perovskite Layer Composition	Electron Transport Layer	Buffer Layer	Behavior	Forward Current Density [mA*cm <sup>-2</sup> ] @ 2.0 V
PtI <sub>4</sub> +CsI	FTO	none	Diode	12 *10 <sup>-3</sup>
PtI <sub>4</sub> +CsI	FTO	CdS	Leaky Diode	1.2 *10 <sup>-3</sup>
PtI <sub>4</sub> +CsI	ITO	none	Resistor	1.5
PtI <sub>2</sub> +CsI	FTO	none	Diode	1.8
PtI <sub>2</sub> +CsI	FTO	CdS	Diode	3.6 *10 <sup>-3</sup>
PtI <sub>2</sub> +CsI	ITO	none	Resistor	1.5



### 2.3.2 Device Results

Dark and light current voltage measurements were performed on the devices with a voltage range of -0.5-2.0 volts. Dark tests resulted in diode curves for many of the device types indicating a semi-conductive nature of the perovskite material. However, no device type was found to be conclusively photo responsive.

Using the best current-voltage curves from both perovskite materials, the diode factor, series resistance, shunt resistance, and the diode current density using the methods detailed in Chapter 1. The results of this analysis can be found in Table 9. These results are estimates for the current devices and may be different in further analysis. The J-V curves used in this analysis are located in the following section.

**Table 9: Device diode factor, series resistance, shunt resistance, and diode current density estimates.**

	PtI <sub>4</sub> Material	PtI <sub>2</sub> Material
<b>Diode Factor</b>	1.4-2.6	2.2-4.6
<b>Series Resistance [kΩ]</b>	109	241
<b>Shunt Conductance [kΩ<sup>-1</sup>]</b>	0.00025	0.00006
<b>Diode Current Density, J<sub>0</sub> [uA/cm<sup>2</sup>]</b>	0.009	0.003

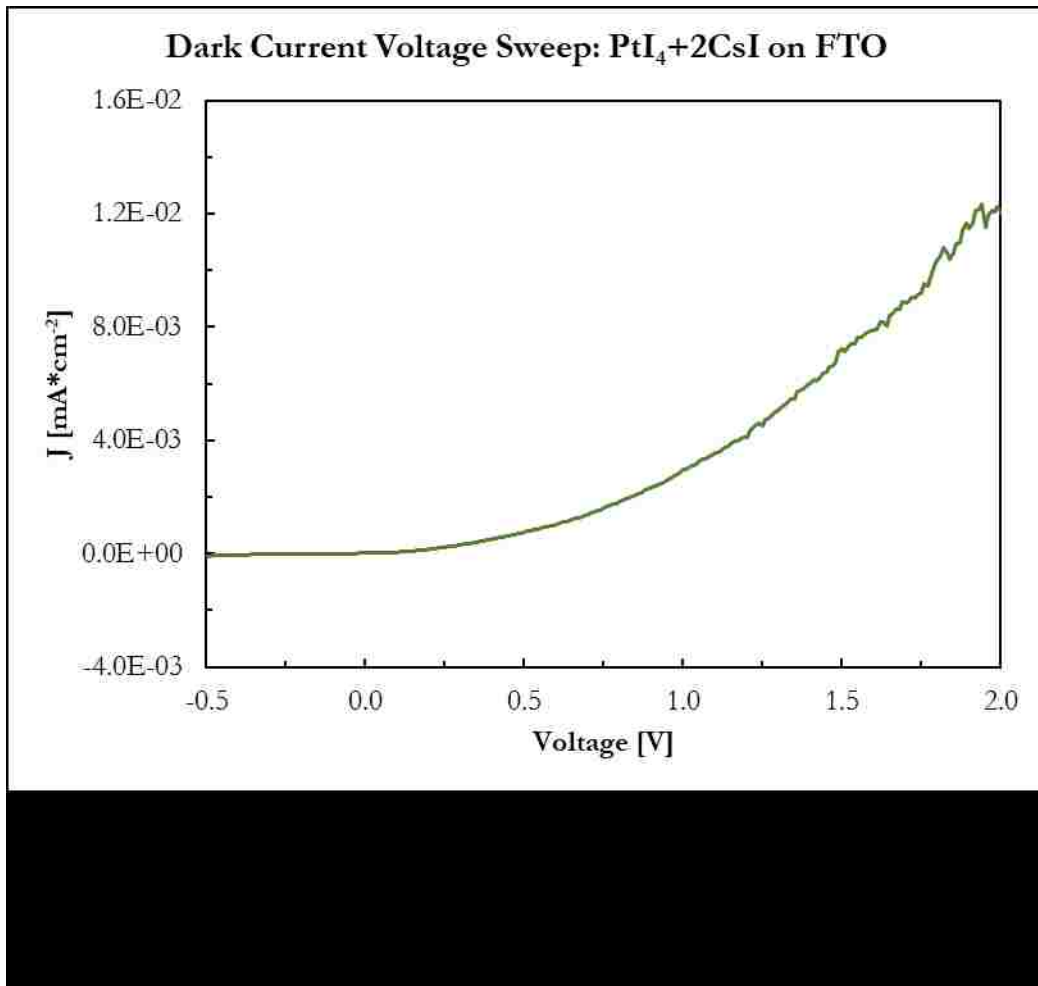
■ Devices fabricated with PtI<sub>4</sub>

The devices presented are composed of the Cs<sub>2</sub>PtI<sub>6</sub> perovskite composed from PtI<sub>4</sub> and CsI using a DMF/DMSO solvent. Device fabrication variations with a FTO electron transport layer, CdS and a FTO electron transport layer, and an ITO electron transport layer are discussed below.

### **Cs<sub>2</sub>PtI<sub>6</sub> on FTO**

The absorber layer was annealed onto an FTO layer and coated with carbon paste, as outlined in Chapter 1. The current voltage data found in Figure 34 shows the device exhibits diode

behavior; the non-linear convex curve shape indicates little to no flow in reverse bias with increased current flow in forward bias. The shunt and series resistance can be determined from examining the slope near 0.0 volts and at a linear region higher voltage.

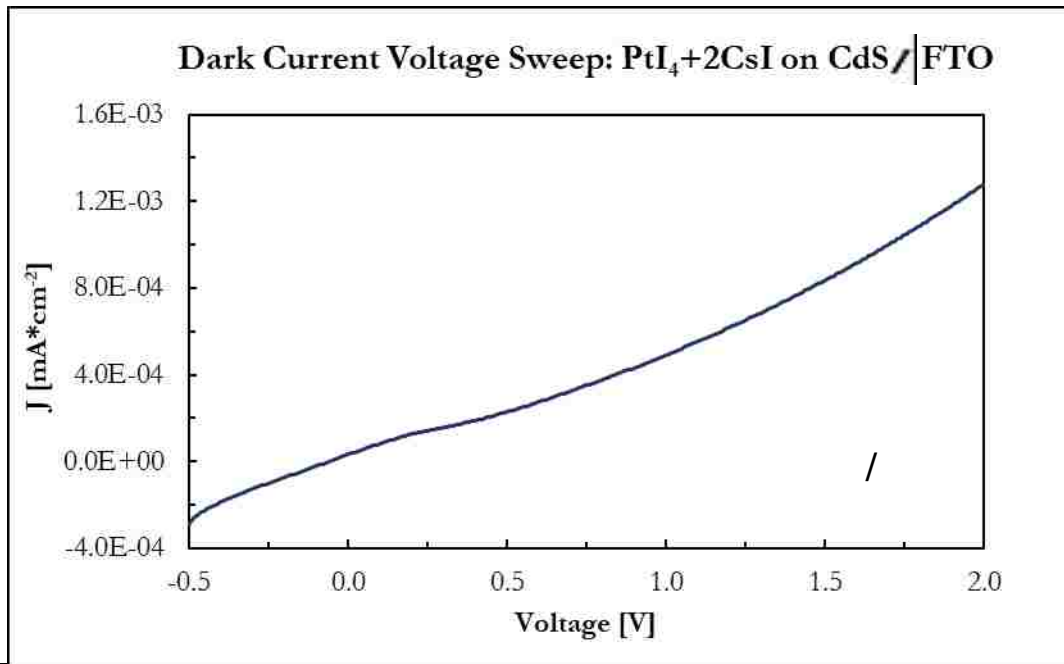


The dark diode curve indicates semiconductor behavior; however, the lack of photovoltaic response to the same test repeated with a solar simulator at 100 mW\*cm<sup>-2</sup> indicate issues in

interactions between layers, in perovskite layer thickness, or other issues preventing an increased current with light exposure.

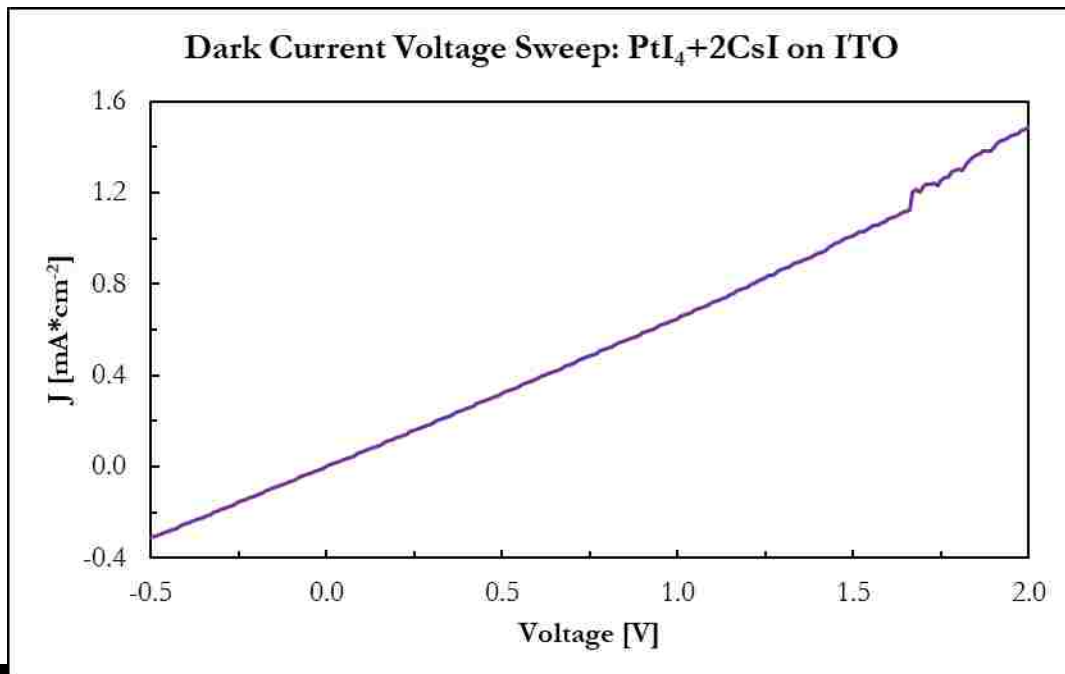
### **Cs<sub>2</sub>PtI<sub>6</sub> on FTO and CdS**

The absorber layer was annealed onto a CdS coated FTO layer and coated with carbon paste, as outlined in the Methodology section. The addition of the CdS buffer layer was hypothesized to increase the current flow, although this was not found to be the case. The current voltage data found in Figure 35 shows the device exhibits a combination of diode and resistive behavior; the non-linear curve indicates increased current flow in forward bias with some flow in reverse bias. The dark diode curve indicates semiconductor behavior; however, the lack of photovoltaic response to the same test repeated with a solar simulator at  $100 \text{ mW} \cdot \text{cm}^{-2}$  indicate issues in interactions between layers, in perovskite layer thickness, or other issues preventing an increased current with light exposure.



### Cs<sub>2</sub>PtI<sub>6</sub> on ITO

The absorber layer was annealed onto an ITO layer and coated with carbon paste, as outlined in the Methodology section. The current voltage data found in Figure 36 shows the device exhibits only resistive behavior; the linear shape indicates proportional increase of flow as the voltage is increased with an approximate resistivity of 1.52 kΩ\* cm<sup>-2</sup>. The dark diode curve does not exhibit semiconductor behavior; additionally, the lack of photovoltaic response to the same test repeated with a solar simulator at 100 mW\*cm<sup>-2</sup> indicate other issues as discussed in the subsequent section.



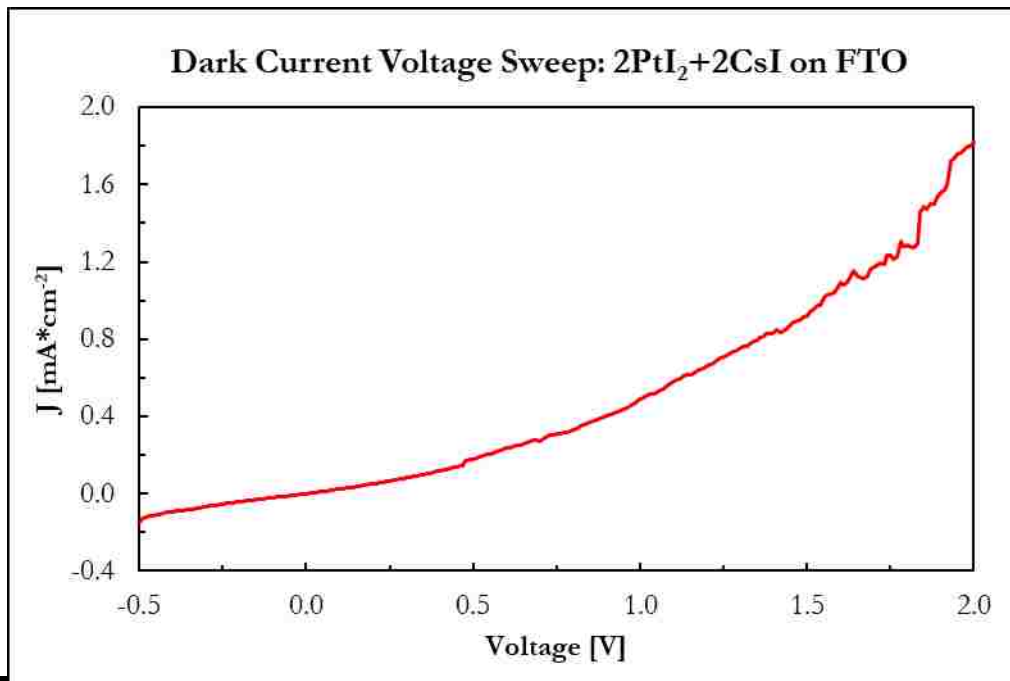
■ Devices fabricated with PtI<sub>2</sub>

The devices presented are composed of the cesium platinum iodide perovskite composed from PtI<sub>2</sub> and CsI using a DMF/DMSO solvent. Device fabrication variations with a FTO electron transport layer, CdS and a FTO electron transport layer, and an ITO electron transport layer are discussed below.



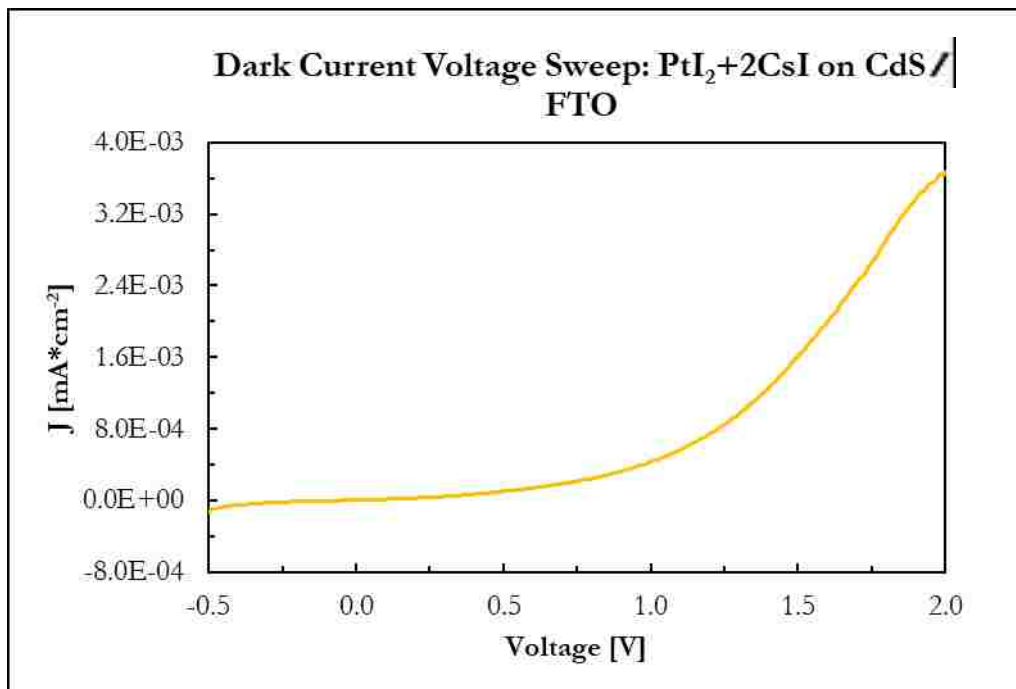
## CsI and PtI<sub>2</sub> Material on FTO

The absorber layer was annealed onto an FTO layer and coated with carbon paste, as outlined in the Methodology section. The current voltage data found in Figure 37 shows the device exhibits diode behavior; the non-linear convex curve shape indicates little to no flow in reverse bias with increased current flow in forward bias. The dark diode curve indicates semiconductor behavior; however, the lack of photovoltaic response to the same test repeated with a solar simulator at 100 mW\*cm<sup>-2</sup> indicate issues in interactions between layers, in perovskite layer thickness, or other issues preventing an increased current with light exposure.



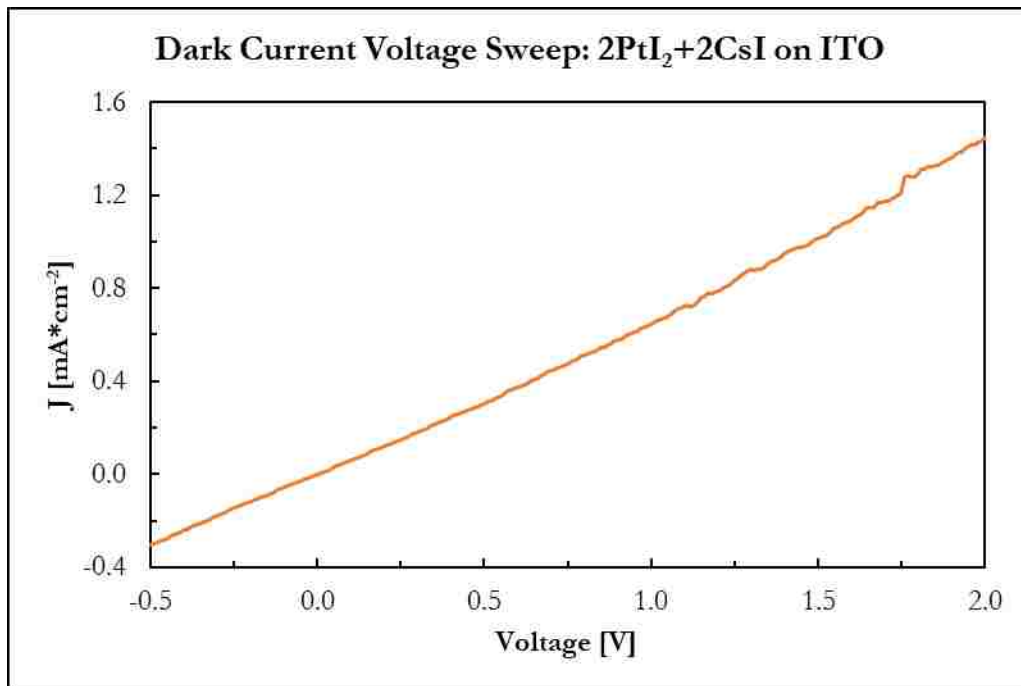
## CsI and PtI<sub>2</sub> Material on CdS Coated FTO

The absorber layer was annealed onto a CdS coated FTO layer and coated with carbon paste, as outlined in the Methodology section. The addition of the CdS buffer layer was hypothesized to increase the current flow, although this was not found to be the case. The current voltage data found in Figure 38 shows the device exhibits a combination of diode and resistive behavior; the non-linear curve indicates increased current flow in forward bias with some flow in reverse bias. The dark diode curve indicates semiconductor behavior; however, the lack of photovoltaic response to the same test repeated with a solar simulator at 100 mW\*cm<sup>-2</sup> indicate issues in interactions between layers, in perovskite layer thickness, or other issues preventing an increased current with light exposure.



## CsI and PtI<sub>2</sub> Material on ITO

The absorber layer was annealed onto an ITO layer and coated with carbon paste, as outlined in the Methodology section. The current voltage data found in Figure 39 shows the device exhibits only resistive behavior; the linear shape indicates proportional increase of flow as the voltage is increased with an approximate resistivity of 1.53 k $\Omega$ -cm<sup>2</sup>. The dark diode curve does not exhibit semiconductor behavior; additionally, the lack of photovoltaic response to the same test repeated with a solar simulator at 100 mW\*cm<sup>-2</sup> indicate other issues as discussed in the subsequent section.



### 2.3.3 Opportunities for Device Fabrication Improvement

Why does a material exhibiting diode behavior and a bandgap within an appropriate range for photovoltaic response result in no increased current output when exposed to light? The issues with these devices are twofold; the perovskite layer is sub-optimal for photovoltaic performance and the device fabrication methods need improvement. Issues specific to each layer are discussed below:

- **Electron Transport layer:** ITO or FTO was used for this layer. The ITO, purchased from Sigma Aldrich, had a 70-100  $\Omega$  resistance. However, all devices fabricated using ITO and either cesium platinum iodide material was purely a resistor with a resistance of around 1.5  $\text{k}\Omega \cdot \text{cm}^{-2}$  as calculated from dark current voltage data. The increase in resistance is not understood but is likely related to ITO layer. FTO resulted in a diode curve for both material types with more significant current density in the device made from the  $\text{PbI}_2$  material. Preliminary results indicate FTO may be a more effective ETL for both perovskite materials but less resistive ITO may also be effective.
- **Buffer layer:** A buffer layer is expected to increase the current output of a solar cell by improving shunt resistance and is widely used and reported in perovskite solar cells. However, this was not found to be the case for the FTO with CdS devices tested. While devices made from both absorber material types show some amount of diode behavior, the maximum current output was less than the maximum output for the same cell without the buffer layer by a factor of one to three magnitudes. A variety of reasons could cause this decrease in output: the surface may have oxidized prior to perovskite

deposition, the absorber layer or some element of the cell could have poor contact with another layer (possibly unrelated to the CdS layer), or CdS could be a poor buffer layer match for the cesium platinum iodide material. Other buffer layers could be tried and more tests should be done with CdS.

- **Contacts:** This layer is currently composed of conductive carbon paste. Some cells were shorted by carbon paste leaking through the perovskite layer, resulting in no current density measurements. Thus, the use of carbon paste directly on the perovskite necessitated the perovskite layer be thicker than a typical spin-coated layer. Additionally, though conductive, the conductivity may be less than that of gold or platinum contacts resulting in a current loss at the contact. Other contact types should be evaluated for use in cesium platinum iodide perovskite cells.
- **CsI+PtI<sub>4</sub> perovskite absorber layer:** This layer is composed of the material discussed in the first section of this chapter. The medium bandgap, high absorbance coefficient, and very long carrier lifetime suggest this material would be optimal as a thin film material. However, spin coating methods have resulted in large grains with voids in between; this is a recipe for device shunting. Rather, a thicker layer was used for preliminary testing. This may lead to higher recombination and series resistance and result in decreased current output. Opportunities for improvement exist in morphology optimization.

- **CsI+PtI<sub>2</sub> perovskite absorber layer:** This layer is composed of the material discussed in the second section of this chapter. The high bandgap, high absorption coefficient, and average carrier lifetime suggest this material would be optimal as a thin film material. However, spin coating methods have resulted a material with a very high bandgap. A thicker layer was used for preliminary testing. This may lead to higher recombination and series resistance and result in decreased current output. Opportunities for improvement exist in material synthesis and morphology optimization.
- **Positive and negative leads:** The leads used in these devices were conductive aluminum coated tin tape due to material availability. These may not be the optimal match for either material type.

### 2.3.4 Device Fabrication Summary

Six device types were made using the two cesium platinum iodide materials as p-type and FTO, ITO or CdS as n-type junction partners detailed previously. None of the devices were found to be conclusively light responsive, although devices fabricated from both types of materials exhibited diode behavior in dark current-voltage measurements. This indicates these devices are behaving as semiconductors. Many variables in the absorber layer processing, ETL and buffer layer coated superstrate preparation, and device fabrication need to be optimized and better understood. Outstanding issues include reducing the absorber layer thickness without creating shunting in the cell, reducing bulk film resistance as well as contact resistance between

layers. Successful high efficiency devices have not yet been fabricated using these materials; however,  $\text{Cs}_2\text{PbI}_6$  and  $\text{CsI} + \text{PbI}_2$  based perovskite materials remain promising for further study as mid to wide bandgap semiconductors for photovoltaics and other optoelectronic applications.

## CHAPTER 3: LABORATORY FABRICATION COSTS OF LEAD AND LEAD FREE PEROVSKITES

A major draw to the study of perovskites for photovoltaic applications is the relatively low costs associated with the solution processing methods used to synthesize many of these materials.

The cost of materials for lead-based perovskites and the simplicity of lab equipment required for processing has assisted in the increased study of perovskites since 2012 when the first methylammonium lead iodide solar cells [45] were reported. In order to alter the perovskite material bandgap, stability and other properties, various molecular modifications have been studied. Lead-free perovskites are of particular interest, due to the lead toxicity concerns in the United States and continues stability issues with lead perovskites. However, modifying the  $ABX_3$  perovskite element composition and proportion alters many aspects of the cost including solutes used, solvents used and processing methods. This section provides a cost analysis and comparison of various iodide perovskites.

The costs in this section are intended to represent a realistic laboratory costs of consumable materials used in perovskite processing. Increased cost due to lab equipment required for oxygen free processing is briefly discussed but no cost estimates are provided. Various iodide-based perovskites, double perovskites, and double perovskites with excess B-site cation are evaluate in terms of solute, solvent and total solution cost. Cost calculations assume a pin-hole free surface and a pure perovskite product, unless specifically stated.



### 3.1 Costs Associated with Solute Used

This analysis determines the cost per volume of each perovskite material. While the desired thickness of each material will vary based on the material's optical properties and application, these thin film materials will require a similar thickness and volume for laboratory study. Therefore, cost per unit volume is appropriate for cost comparison in thin film perovskite materials.

The cost per unit volume is determined by the perovskite (product) volume and the cost and proportional amount of reactants needed to achieve the product volume. The amount of perovskite, by moles, is determined using the known molecular mass (g/mol) and density (g/cm<sup>3</sup>) of the product, as seen in Equation 1. Table 10 shows the published molecular mass and density values with the resulting moles for one cubic centimeter of perovskite product, calculated using Equation 9.

**Equation 9: Moles of perovskite by volume as a function of density and molar mass.**

$$\frac{\text{Moles of Perovskite} \left[ \frac{\text{mol}}{\text{cm}^3} \right]}{\text{cm}^3} = \frac{\text{Density} \left[ \frac{\text{g}}{\text{cm}^3} \right]}{\text{Molar mass} \left[ \frac{\text{g}}{\text{mol}} \right]}$$

**Table 10: Published molecular mass and density, as used to calculate the resulting moles of perovskite product per cubic centimeter. The required mMol refers to the moles of product perovskite in a cubic centimeter.**

Perovskite Product	Molecular Mass [g* $\text{mol}^{-1}$ ]	Density [g* $\text{cm}^{-3}$ ]	Required mMol [mMol]
<b>Cs<sub>2</sub>PtI<sub>6</sub></b>	1222	5.02	4.11
<b>Cs<sub>2</sub>SnI<sub>6</sub></b>	1146	4.33	3.78
<b>Rb<sub>2</sub>SnI<sub>6</sub></b>	1051	4.19	3.99
<b>K<sub>2</sub>PtI<sub>6</sub></b>	1035	4.74	4.58
<b>Cs<sub>2</sub>TeI<sub>6</sub></b>	1155	4.37	3.78
<b>CsSnI<sub>3</sub></b>	632	4.28	6.77
<b>RbSnI<sub>3</sub></b>	585	4.87	8.33
<b>CsGeI<sub>3</sub></b>	586	4.30	7.33
<b>MAPbI<sub>3</sub></b>	620	4.16	6.71
<b>Cs<sub>2</sub>PtI<sub>6</sub> +Pt</b>	1417	7.28	5.14
<b>Cs<sub>2</sub>SnI<sub>6</sub> +Sn</b>	1265	7.00	5.53

From here, an idea chemical reaction formula is used to determine the amount of solvent needed. Three different chemical formulas are used, as depicted in Table 11. A formula type is selected for each perovskite type depending on the product molecular structure. This analysis uses standard perovskite structure ( $\text{ABX}_3$ , Type A), vacant B cation modified perovskite structure ( $\text{A}_{2-2}\text{BX}_6$ , Type B), and the same modification with excess B-cation ( $\text{A}_2\text{BX}_6+\text{B}$ , Type C). The Type C formula is necessary in certain processing conditions where a  $\text{BX}_4$  molecule will not react with the  $2\text{AX}$  molecule to form a perovskite and  $\text{BX}_2$  reactants must be used. While there are methods to extract the excess B-cation excess from the final product, its  $\text{BX}_2$  reactant molecule is still necessary for the reaction and is included in the cost analysis.

**Table 11: Ideal chemical formulas for perovskites.**

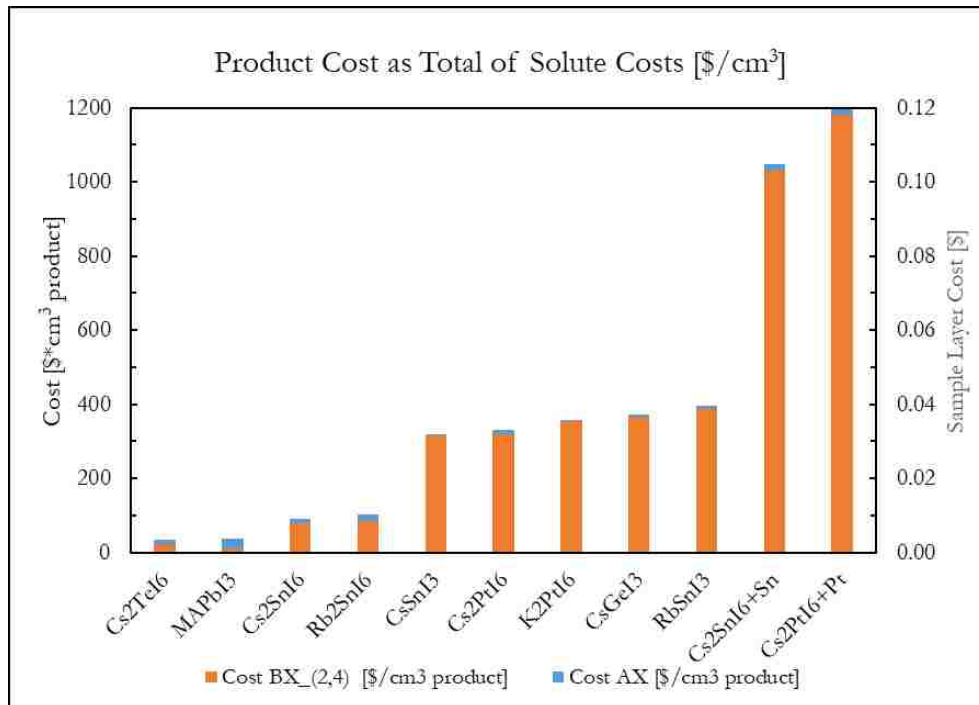
Formula Type	Perovskite	Proportion of AX	Proportion of BX <sub>2</sub>	Proportion of BX <sub>4</sub>	Formula
<b>A</b>	ABX <sub>3</sub>	1	1	0	AX + BX <sub>2</sub> → ABX <sub>3</sub>
<b>B</b>	A <sub>2</sub> BX <sub>6</sub>	2	0	1	2AX + BX <sub>4</sub> → A <sub>2</sub> BX <sub>6</sub>
<b>C</b>	A <sub>2</sub> BX <sub>6</sub> + B	2	2	0	2AX + 2BX <sub>2</sub> → A <sub>2</sub> BX <sub>6</sub> + B

From the previous analysis, the moles of product and molar proportions of solute are known. These proportions can be multiplied with the moles of product to obtain the required moles of reactant. For example, 10<sup>-3</sup> moles of product is required for a certain volume of ABX<sub>3</sub> perovskite, 10<sup>-3</sup> moles of AX and 10<sup>-3</sup> moles of BX<sub>2</sub> are required. The molecular mass can be used to determine the amount of solute required in grams. Solute costs were found using Sigma-Aldrich and/or Alpha Aesar and converted into \$USD per gram. Solute costs are subject to change; the costs used can be found in APPENDIX E and are valid as of February 2019. Cost analysis results can be found in Table 12.

**Table 12: Amount of solutes required to produce 1 cubic centimeter of perovskite product. Conversion between moles and grams of solutes and solute cost can be found in Appendix E.**

Product	Product Moles [ $\cdot 10^{-3}$ ]	AX	Mass of AX [g]	Cost AX [\$]	BX <sub>(2,4)</sub>	Mass of BX <sub>(2,4)</sub> [g]	Cost BX <sub>(2,4)</sub> [\$]	Total Cost [\$/cm <sup>3</sup> ]
Cs <sub>2</sub> PtI <sub>6</sub>	4.11	CsI	2.13	\$6.22	PtI <sub>4</sub>	4.11	\$317.45	\$324
Cs <sub>2</sub> SnI <sub>6</sub>	3.78	CsI	1.96	\$5.73	SnI <sub>4</sub>	3.78	\$79.52	\$85
Rb <sub>2</sub> SnI <sub>6</sub>	3.99	RbI	1.69	\$9.06	SnI <sub>4</sub>	3.99	\$83.89	\$93
K <sub>2</sub> PtI <sub>6</sub>	4.58	KI	1.52	\$1.89	PtI <sub>4</sub>	4.58	\$354.10	\$356
Cs <sub>2</sub> TeI <sub>6</sub>	3.78	CsI	1.97	\$5.73	TeI <sub>4</sub>	3.78	\$22.59	\$28
CsSnI <sub>3</sub>	6.77	CsI	1.76	\$5.13	SnI <sub>2</sub>	6.77	\$315.18	\$320
RbSnI <sub>3</sub>	8.33	RbI	1.77	\$9.46	SnI <sub>2</sub>	8.33	\$387.72	\$397
CsGeI <sub>3</sub>	7.33	CsI	1.91	\$5.56	GeI <sub>2</sub>	7.33	\$366.34	\$372
MAPbI <sub>3</sub>	6.71	MAI	1.07	\$28.59	PbI <sub>2</sub>	6.71	\$9.47	\$38
Cs <sub>2</sub> PtI <sub>6</sub> +Pt	5.14	CsI	2.67	\$7.78	PtI <sub>2</sub>	10.27	\$590.33	\$598
Cs <sub>2</sub> SnI <sub>6</sub> +Sn	5.53	CsI	2.88	\$8.38	SnI <sub>2</sub>	11.07	\$515.33	\$524

The actual cost of solutes will depend on the volume of perovskite necessary. This will depend on the film purpose and material properties. A perovskite film may be used as a layer in a photovoltaic device, for material characterization or for some other purpose. The optical absorbance will influence the optimum thickness and effect the film volume. Figure 40 indicates the total solution costs by cubic centimeter and by cm<sup>2</sup>, 1 μm thick layer. Generally, the AX solute is inexpensive in comparison to the BX<sub>(2,4)</sub> solute cost.



As expected, MAPbI<sub>3</sub> is much less expensive than the majority of the materials studied although the cost of the ABX<sub>3</sub> and A<sub>2</sub>BX<sub>6</sub> materials have no clear trend. The A<sub>2</sub>BX<sub>6</sub>+B materials are the most expensive due to the increased ratio on Bx<sub>2</sub> to AX and increased density from the excess B-cation.

In the case of tin-iodide perovskites, SnI<sub>2</sub> is significantly more expensive than SnI<sub>4</sub> but often dissolves better in low-temperature solution based processing. Thus, Type A and C are significantly more expensive than Type B, but Type B may be more difficult to synthesize in a low temperature process.

For comparison purposes, the costs were derived on a per volume basis. However, it is unlikely a cubic centimeter of perovskite material will need to be synthesized at one time. Thin film photovoltaic materials are often under a micron thick. In a laboratory setting, thickness will vary based on deposition technique and sample purpose. For reference, solute costs is given for a cell area of 1 cm<sup>2</sup> and 1 micron thick. These costs can be scaled depending on estimated sample volume.

### **3.2 Costs Associated with Solvent Used**

Solution based processing utilizes solvents to dissolve solute, form intermediate phases, and precipitate out perovskite product. While an ideal reaction leaves no solvent content within the final product, the solvent is a factor in the total sample cost. Solvents used throughout perovskite processing vary. Four common solvents are included in this analysis for the purpose of cost estimation, as seen in Table 13. Often, solvents are combined for optimum processing results.

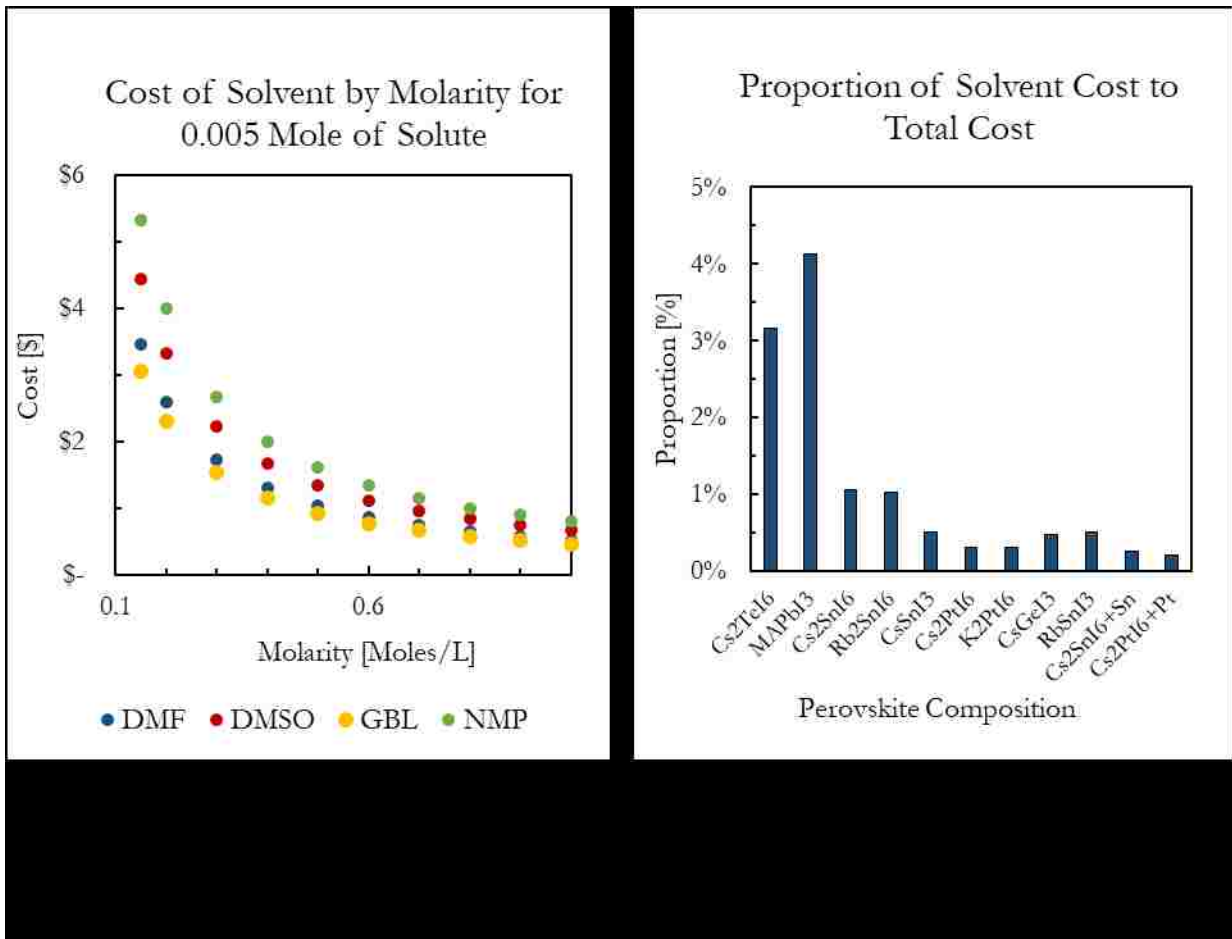
**Table 13: Common perovskite processing solvents with cost information from Sigma-Aldrich. Cost is highly dependent on amount. Costs were selected using purchase prices for as close to 1 liter as possible. GBL is a List 1 controlled chemical in the United States and similarly regulated in many countries; it can be less convenient and timely to obtain larger volumes resulting in higher costs than the cost used in this analysis.**

<b>Solvent</b>	<b>Full Name</b>	<b>Cost [\$/mL]</b>	<b>Purity [%]</b>	<b>Sigma Aldrich CAS</b>
<b>DMF</b>	Dimethylformamide	\$ 0.10	0.998	68-12-2
<b>DMSO</b>	Dimethyl sulfoxide	\$ 0.13	0.999	67-68-5
<b>GBL</b>	$\gamma$ -Butyrolactone	\$ 0.09	0.99	96-48-0
<b>NMP</b>	1-Methyl-2-pyrrolidinone	\$ 0.16	0.995	872-50-4

Solvent costs are determined by finding the volume of solvent required for a certain solution molarity multiplied by the solvent cost per unit volume, as displayed in Equation 10. Solution molarity is dependant on the solvents, solutes and processing methods. The molarity is variable throughout perovskite processing literature but is often between 0.2M to 1M. The estimated cost of solvents is plotted as a function of molarity for a constant solute amount can be found in Figure 41. The solute amount selected is within the scale of solutes needed to synthesize 1 cm<sup>3</sup> of perovskite as listed in Figure 41 and Table 13. It is apparent the solvents are an inexpensive cost component; this can be observed clearly in Figure 42, where the average solvent cost (by unit volume) is used to estimate the proportion of solvent cost to the total solution cost. Unless a more expensive solvent is used or a solution is at a very low molarity, solvents are expected to contribute under 10% of the costs for solutions with less expensive solvents and likely under 1% for solutions with more expensive solutes. Solute should not be neglected in cost estimates but are not a large contributor in laboratory setting solution-based processing perovskite synthesis.

Equation 10: The solvent cost depends upon the volume of solvent used and the cost of the solvent. The volume required is dependent upon the molarity and amount of solute used.

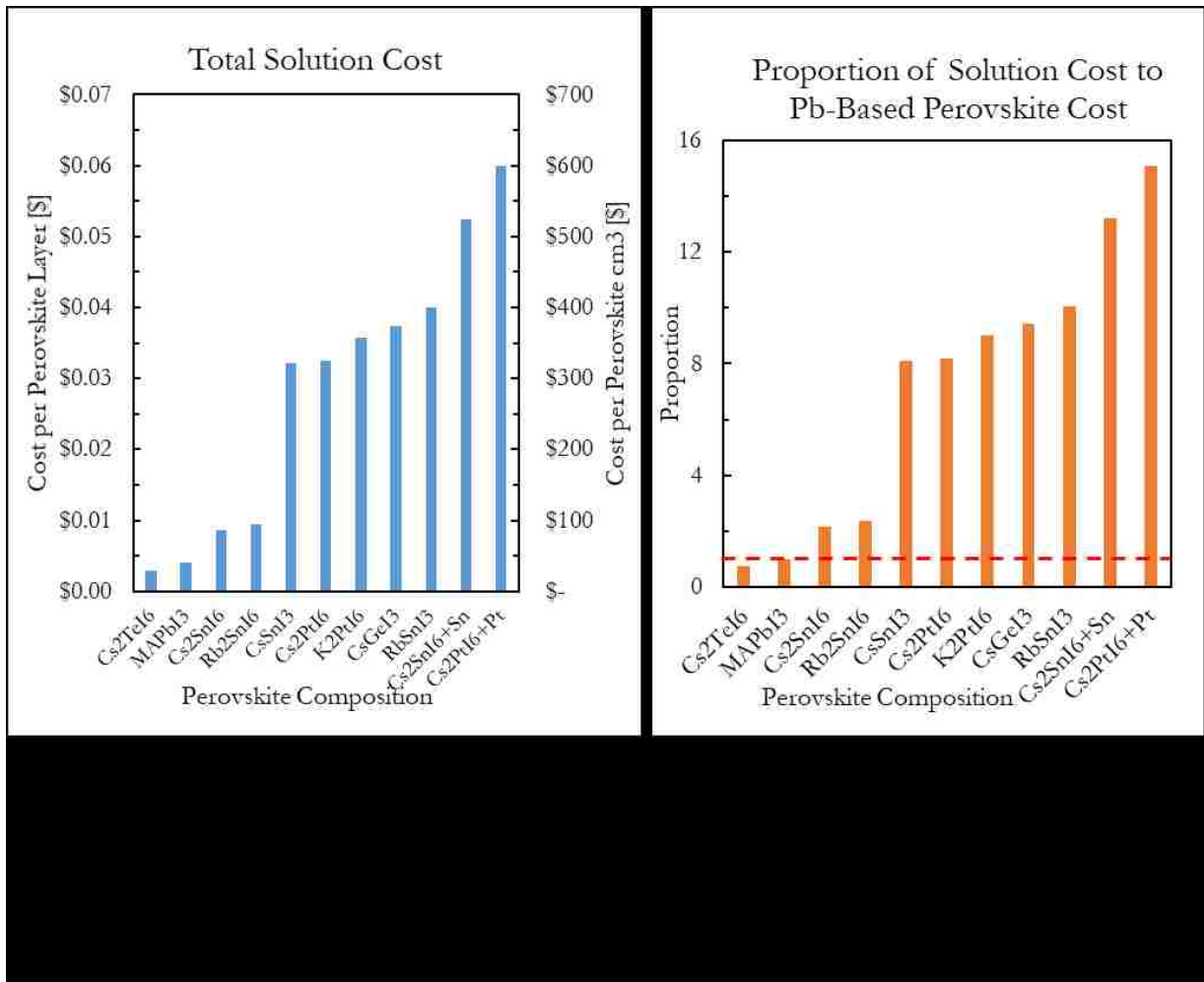
$$\text{Solvent Cost [\$]} = \frac{\text{Moles of Product [Mol]} * \text{Cost of solvent } \left[\frac{\$}{\text{L}}\right]}{\text{Molarity } \left[\frac{\text{Mol}}{\text{L}}\right]}$$





### 3.3 Total Costs Associated with Solution Preparation

Thin film materials do not present exorbitant laboratory costs when looking at the materials alone. Solutes make up the majority of the expense (>95% in most cases). However, there is a large cost difference when comparing traditional lead-based perovskites with  $ABX_3$  and  $A_2BX_6$  lead-free materials. While costs for a  $1\text{ cm}^2$ , 1 micron sample range from around 0.05-0.6¢, the more expensive lead free perovskites are 10-15X the costs of  $MAPbI_3$ , as seen in Figure 42.



While this is a significant cost difference, the solution costs are not representative of the total processing expensive. Other materials used in film sample and photovoltaic device fabrication are largely similar for all thin film materials. For example, ITO coated glass, which is commonly used as a substrate or superstrate in thin film devices, costs roughly \$5.00-\$15.00 per 25mm square (Sigma Aldrich). This significantly exceeds the solution costs for a single film sample.

Further, various materials will require changes in processing methods. Some materials, such as  $\text{Cs}_2\text{PbI}_6$  and  $\text{Cs}_2\text{SnI}_6$ , have been reported using ambient air processes. Lead and germanium perovskites, while possibly stable in atmospheric conditions post-processing, require processing in inert gas gloveboxes which drastically increases laboratory start up fees and possibly more space. As perovskites develop further, processing sophistication (and therefore associated equipment costs) will inevitably increase. However, studying lead-free perovskites in a laboratory setting is not cost prohibitive based on solute and solvent costs alone. Further, low temperature solution-based perovskite processes are inexpensive and simple regarding the lab equipment required for study.

### **3.4 Practical Applications of Cost Analysis**

The previous analysis compares ideal perovskite materials on a per thickness unit basis. This is useful as a general comparison but neglects the realities of thin film photovoltaics. The optimal thickness required for a photovoltaic device is dependent on many variables; generally, an absorber layer should be thick enough to absorb as much energy as possible without accumulating thickness-induced losses. The following analysis attempts to compare cost using

measured optical properties for a traditional photovoltaic perovskite (MAPbI<sub>3</sub>) and a more recent cesium platinum iodide perovskites reported on previously in this document.

Material thickness is not arbitrary and will vary based on other material properties including the absorbance coefficient, which is the capability of a material to absorb photons of different energies. By comparing the absorbance coefficient at various wavelengths for two materials, the ratio of thickness required to achieve the same photon absorbance can be determined using the ratio determined by Equation 11. Using the analysis in the previous section, a more meaningful material cost ratio can be achieved.

**Equation 11: The ratio of absorbance coefficients (denoted by  $\alpha$ ) will be related to the ratio of material thickness (denoted by  $x$ ) for the same intensity ratio.**

$$\frac{\alpha_1}{\alpha_2} = \frac{x_2}{x_1} = \ln \frac{I}{I_0}$$

The absorbance coefficients for perovskite materials was determined for two cesium platinum iodide perovskite films. The proposed formula for these materials can be found in Equation 11: The ratio of absorbance coefficients (denoted by  $\alpha$ ) will be related to the ratio of material thickness (denoted by  $x$ ) for the same intensity ratio.; however, the resulting film is not a single phase or of ideal density. Thus, the absorbance coefficients proposed in Figure 43 may change with processing improvements. For an ideal density film with only a perovskite phase, the absorbance should increase. For this analysis, the non-ideal absorbance coefficient is paired with the ideal costs from the previous section. Cost analysis updates should be made as material processing improves. The MAPbI<sub>3</sub> absorbance coefficient is believed to be near ideal representative and is not expected to change much [29]. From the figure, it is apparent both

cesium-platinum-iodide combinations have a higher absorbance coefficient below 2.75 eV. The resulting thickness and cost ratios determined from Figure 43 and the previous cost analysis can be found in Table 14.

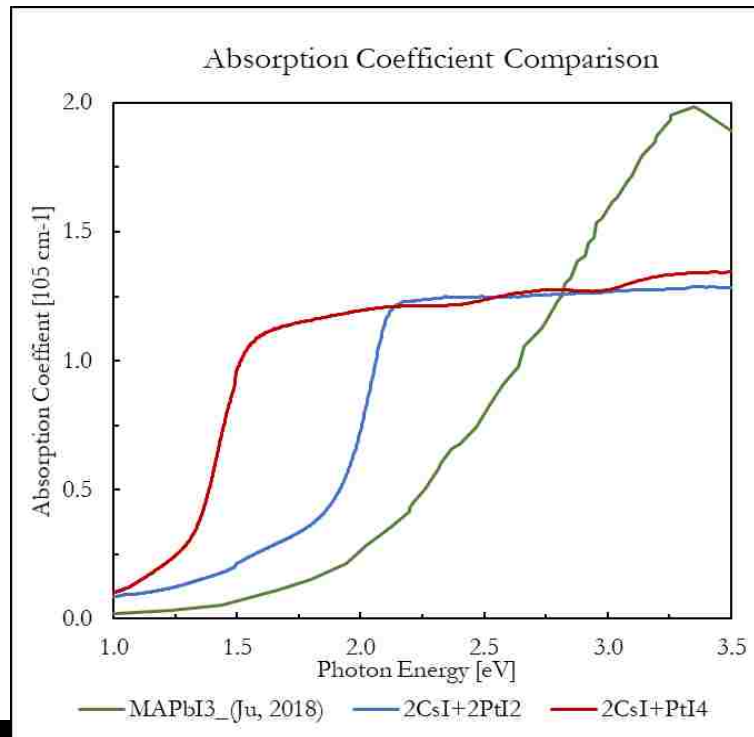


**Table 14: Thickness and cost ratios of MAPbI<sub>3</sub> to cesium platinum iodide perovskites.**

Photon Energy [eV]	MAPbI <sub>3</sub> :Cs <sub>2</sub> PtI <sub>6</sub>		MAPbI <sub>3</sub> :Cs <sub>2</sub> PtI <sub>6</sub> +Pt	
	Thickness Ratio	Cost Ratio	Thickness Ratio	Cost Ratio
1.50	17.5	2.1	3.9	0.2
1.75	10.3	1.2	3.0	0.2
2.00	5.6	0.7	3.4	0.2
2.25	2.7	0.3	2.8	0.2
3.00	0.8	0.1	0.8	0.1

For most wavelengths, the thickness of MAPbI<sub>3</sub> required is greater than that of both of the cesium platinum iodide perovskite variations. Even with the greater thickness requirement of MAPbI<sub>3</sub>, the solute cost is generally lower. Near the bandgap of MAPbI<sub>3</sub> ( $E_g = 1.4$ ), however, the absorbance coefficient is relatively low resulting in a film that must be 17 times thicker and twice as expensive as Cs<sub>2</sub>PtI<sub>6</sub> which has a similar bandgap. The absorption coefficient increases with photon energy and photons with energies at and just above a material bandgap are beneficial to efficiency to harvest; therefore, the thickness and cost ratios at 1.5 eV represent a minimum thickness comparison. While perovskite and material costs are dependent on many variables, this general analysis determines that non-lead perovskites are not cost-prohibitive and can even be less expensive than lead-based perovskites if ultra-thin film processing methods are available.

## CHAPTER 4: CONCLUSIONS AND FUTURE RESEARCH

### 4.1 Conclusions

Global energy use is expected to increase with the expanding human population and an increase in access to electricity sources; facilitating this growth with reliable clean energy sources is of increasing concern. Since the debut of practical photovoltaic solar power by Bell Labs in the mid-1900s, silicon technology has improved to the point that residential solar is common across the United States. However, photovoltaics make up small fraction of the utility scale electricity production in the United States despite visibility and technological advances. An energy market dominated by photovoltaics is unrealistic; numerous barriers impervious to solution by solar cell technological advances prevent this reality. However, advances in photovoltaic cell efficiency and relative cost can drastically accelerate photovoltaic technology adoption for residential and commercial use. Additionally, reducing the area required to produce a certain amount of energy could improve feasibility for multi-level buildings, transportation, public lighting and a multitude of other uses. Continued research on photovoltaics, including third generation materials such as thin film perovskites, are imperative to the creation and adoption of affordable high efficiency energy sources.

Cesium platinum iodide perovskites were selected for study as a possible absorber layer in a tandem or single layer photovoltaic device due to expected mid to high bandgaps and increased thermal and environmental stability over the more widely studied high efficiency, lead-based perovskites. Using solution processing techniques similar to common methods used in lead-

based perovskite processing, two cesium platinum iodide materials were synthesized. Unlike lead perovskite processing, all process steps (except annealing) occurred under atmospheric conditions. This material requires less equipment for initial study and is more air tolerant than many other perovskite variations which require some amount of fabrication within an inert gas glove box. Two distinct material types were formed using a combination of DMF and DMSO solvents with CsI and PtI<sub>4</sub> or CsI and PtI<sub>2</sub> solutes. Other solvent combinations attempted did not consistently result in the formation of a perovskite phase.

Using a PtI<sub>4</sub> platinum source formed a black film with Cs<sub>2</sub>PtI<sub>6</sub> as the major phase and a low intensity unidentified peaks. This film was found to have a number of positive attributes for photovoltaic use. An optical bandgap of 1.4 eV was found using UV-vis spectroscopy and photoluminescence methods. A minority carrier lifetime of 2.75 μs, exceeding that of known lead-based perovskites was determined. Additionally, it is found to have high absorption coefficient relative to other MAPbI<sub>3</sub> and other thin film materials. These three factors indicate this material has the potential to act as an effective thin film absorber layer in a single or multilayer solar cell. Additionally, preliminary differential scanning calorimetry indicate phase transition ~ 590 °C, indicating material stability well above normal operating temperature. Large crystals of Cs<sub>2</sub>PtI<sub>6</sub> with small amount of Cl impurities was produced by atmospheric processing with CsI and PtI<sub>4</sub> based precursors, which can be utilized in form of a mesoporous or planar device structure. To obtain a uniform, void-free polycrystalline film, alternate deposition methods such as vapor deposition or alternate seed materials may be needed to control crystal growth.

Using a  $\text{PtI}_2$  based precursors, a wider bandgap material, a reddish-black looking film is formed composed of a mixed phase of  $\text{Cs}_2\text{PtI}_6$  and an unidentified phase in varying ratios. This film was found to have a number of positive attributes for photovoltaic use. An optical bandgap of 1.9 eV was found using UV-vis spectroscopy and photoluminescence methods. Additionally, it is found to have high absorption coefficient ( $1.5 \times 10^5 \text{ cm}^{-1}$ ) and minority carrier lifetime of 63 ns, indicating promise for effective top-cell absorber layer in a multi-junction solar cell. Significant challenges remain with this material; current synthesis procedures with doctor blade deposition produce samples which are consistent in color and bandgap but present a significant variation in film morphology and powder x-ray diffraction patterns. Furthermore, 1-2 mm crystals of what is thought to be  $\text{Cs}_2\text{PtI}_6$  have formed on these films during at least two separate sample batches. Spin coating deposition methods in an ambient environment lead to an increased bandgap past usefulness for significant photovoltaic generation. Further study is required to determine phase stability in environments with increased temperatures or prolonged air and humidity exposure. This material is certainly interesting but ultimately requires more work and understanding for utility as a photovoltaic absorber material.

Devices fabricated using both materials resulted in device structure dependent diode behavior with no definite photo generation. The devices fabricated show small forward current in dark indicating low diffusion and recombination current, perhaps resulting from high bulk sheet resistance of perovskite or contact resistance. The lack of photo generation could result from issues in the perovskite materials, other materials used as layers, contacts and leads or, most likely, a combination thereof. The resulting diode behavior with n-type layers such as ITO, FTO,



CdS indicates formation of a n-p junction confirming p-type semiconducting behavior of both types of materials processed here.

A materials cost analysis performed indicates that cesium platinum iodide synthesis costs are higher than lead based materials on a per-weight basis, as is expected. However, upon comparison of optimal absorption thickness, a thinner layer of the platinum is needed, thus reducing the price of platinum containing perovskites nearer to that of lead perovskites. In a laboratory setting, the price of coated substrates is likely greater than that of individual layers. While these costs will not directly extrapolate to commercial scale manufacturing, it is worth keeping in mind the cost of the absorber layer is a small portion of the total solar cell cost; platinum based perovskites may not be commercially cost prohibitive due to the small layer thickness and value in efficiency improvement in a tandem cell. Additionally, most labs will not find working with platinum containing solutes cost prohibitive if materials are used carefully.

Promising results have been shown for first experimental demonstrations of  $\text{Cs}_2\text{PtI}_6$  phase formation and promising properties of the material for photovoltaic and other optoelectronic applications. A new halogen-chalcogen phase containing Cs-Pt-I-O-S has also be discovered in this research as a p-type semiconductor with bandgap tunability that can be achieved by varying chalcogen (O, S) concentration. More research is needed into identifying this phase, but this material can also be very interesting for photovoltaic or other optoelectronic applications due to its unique properties. Suggestions to future research are highlighted below.

## 4.2 Future Research

A list of topics of interest is provided to encourage further research into this subject. This current research provides an initial motivation for continues study but leave apple room opportunity for future development. Generally, the process used needs modification for optimal morphology and phase purity for high efficiency absorber materials.

Future study is needed for the optimization of material synthesized from platinum tetra iodide and cesium iodide for use in photovoltaics. Specific research ideas are listed below:

- Correlation of grain size to processing conditions with the objective of forming a closely packed thin film. Quicker precipitation from the solution, possibly accomplished using anti-solvent methods, may assist in smaller and more closely packed grain formation.
- Single crystal x-ray diffraction measurements can be completed with the larger  $\text{Cs}_2\text{PtI}_6$  grains from the blade processed films. Single crystal measurements can confirm or update existing x-ray diffraction patterns as few exist.
- Material synthesis and grain growth on a single crystal superstrate may encourage more tightly packed and similarly oriented grains.
- A thorough study of phase stability in heat, light, air and high humidity should be completed to verify hypothesized stability and better understand how the material is effected by testing and processing conditions.

Future study is needed for the optimization of material synthesized from platinum di-iodide and cesium iodide for use in photovoltaics. Specific research ideas are listed below:

- Phase identification and quantification will be necessary for this materials use as a photovoltaic absorber. If multiple phases exist, which is producing the bandgap? Extensive experimental work coupled with first-principle calculations will be needed to identify this new p-type semiconductor structure.
- The formation of  $\text{Cs}_2\text{PtI}_6$  may be feasible despite mismatches in solute elemental proportions, as seen in a few sample batches with visible areas. Further research into the intermediate phase formed in the solution to understand the reaction paths to formation of pure  $\text{Cs}_2\text{PtI}_6$  (with  $\text{PtI}_4$ ) vs. oxygen containing phase with  $\text{PtI}_2$ .
- A through study of phase stability in heat, light, air and high humidity should be completed to better understand how the material is effected by testing and processing conditions.
- Study into the effect of oxygen concentration on the materials composition and bandgap.
- Optimal charge transport layers will need to be developed based on optimal band alignments.

## APPENDIX A: TESTING AND ANALYSIS PROCEDURES

### A.1 UV-Visible Light Testing and Analysis Procedure

#### A.1.1 Testing Procedure:

The below procedure is a summary of normal instrument use for  $\text{Cs}_2\text{PtI}_6$  measurement purposes. A detailed system of procedure can be found in lab and should be followed for proper instrument use.

1. Turn instrument on and allow machine to warm-up for 15 minutes prior to use.
2. Perform a baseline correction. This can be done in either transmittance or reflectance mode.
3. Take sample transmittance measurements. See Figure 7 for locations.
  - a. Place film in sample holder at location T on as seen in the figure.
  - b. Ensure the white plate is in place at location R.
  - c. Set software to "Transmittance" and S/R Exchange to "normal"
4. Take sample reflectance measurements
  - a. Place film in sample holder at location R on as seen in the figure with white plate removed
  - b. Set software to "reflectance" and S/R Exchange to "inverse"
5. Shut off spectrometer when all samples are measured. Replace the white plate and close the chamber.
6. If sample left residue, carefully clean with small vacuum using small attachment.

### A.1.2 Analysis Procedure:

For this section:

$A = \text{Absorbance}$

$T = \text{Transmittance}$

$R = \text{Reflectance}$

$a = \text{Absorption coefficient}$

$d = \text{Film thickness}$

$h\nu = \text{Photon energy (eV)}$

$E_g = \text{Bandgap (eV)}$

$\lambda = \text{wavelength (nm)}$

$\gamma = \text{bandgap coefficient}$

$$h = \text{Planck's constant} = 6.62607004 \times 10^{-34} \frac{\text{m}^2\text{kg}}{\text{s}}$$

$$c = \text{speed of light} = 299\,792\,458 \frac{\text{m}}{\text{s}}$$

Analysis is done assuming a finite thickness film model (air, film, air). In an ideal scenario with no losses, light hits an interface and is either absorbed, transmitted, or reflected (see Equation 12). Assuming the same entrance and exit interface,

**Equation 12: Assuming no losses, light is absorbed, transmitted and/or reflected as it encounters a new medium.**

$$A + T + R = 1$$

**Equation 13: Relation of normalized transmittance and normalized absorbance assuming no losses and identical surface interfaces.**

$$\frac{T}{(1 - R)^2} = 1 - \frac{A}{(1 - R)^2}$$

**Equation 14: Absorbance coefficient assuming no losses and identical surface interfaces.**

$$\alpha = -\frac{1}{d} * \ln\left[\frac{T}{(1 - R)^2}\right]$$

Total transmission and reflection measurements were done on films deposited on bare glass and the film thickness was determined using cross-sectional scanning electron microscopy (SEM). Tauc plots (methodology developed in 1968) has been used to determine bandgap using a linear fit method with Equation 15 [46].

**Equation 15: Tauc equation, developed in 1968 by J. Tauc for determining the bandgaps of semiconductor materials.**

$$ahv = constant(hv - E_g)^\gamma$$

Where  $\gamma$  is 1/2 for a direct bandgap material and 2 for an indirect bandgap material. Thus, the bandgap must be equal to the photon energy at which  $(\alpha hv)^{1/\gamma}$  is equal to zero. In practice, a line

is fitted to a linear portion of the Tauc relation associated with the absorption edge and where that time crosses the x axis indicated the material bandgap.

1. Plot reflectance and transmittance for each sample tested from 300 nm to 1400 nm
2. Calculate the absorption coefficient using Equation 14.
3. Calculate the photon energy using the equation for photon energy

$$a. \quad hv = \frac{hc}{\lambda} = \frac{1240}{\lambda} \frac{eV \cdot nm}{nm}$$

4. Plot the Tauc relation,  $hv$  vs.  $(\alpha hv)^{1/\gamma}$
5. Find where  $(\alpha hv)^{1/\gamma}$  has a slope change associated with the absorbance edge
  - a. Fit a line through the more sloped portion of the curve
  - b. For a direct bandgap (expected from  $Cs_2PtI_6$ ), the x-value of this fit where  $(\alpha hv)^{1/\gamma}=0$  is the material bandgap.

## A.2 Powder X-Ray Diffraction Testing and Analysis Procedure

### A.2.1 Use Procedure:

The SEB Bruker XRD should not be used without radiochemistry lab access and proper guidance. The machine is normally left on and time should be scheduled using the radiochemistry calendar. Take appropriate safety and health precautions while in the radiochemistry lab.

1. Open the glass doors immediately after pressing the “open door” button. Wearing gloves, prepare sample on a non-rad pad by placing the sample on the gray putty of an available sample stage. Depress the sample using a clean microscope slide so the sample surface is even with the stage. Insert the stage and close glass doors.

2. Using the XRD Commander on the computer, select “Create New Job”. Fill out the new job form using a unique sample ID and the appropriate parameter file.
  - a. The parameter file determines the angle range, step size, step time and rotation rate. XRD Wizard can be used to edit existing parameter files.
  - b. A thin film sample may need to run for two hours for good data, but depends on the sample type and previous XRD runs.
3. Allow sample to run for the time set by the parameter file. When sample is finished, remove sample by reversing step 1. Always remove the sample and leave the XRD area clean.

### **A.2.2 Qualitative Analysis Procedure:**

*Adapted from PowerPoint slides provided in UNLV’s ME695: XRD/SEM course.*

1. Insert .raw scan data
2. For a sample with a standard or known phase that can be used as reference data:
  - a. It is assumed the standard should match the standard’s reference peaks exactly, allowing the whole pattern to be shifted to correct displacement errors
  - b. Upload the reference data
  - c. Zoom in on a peak until a noticeable difference between the scan data and reference data is observed
  - d. Use the x-offset option in the scan data toolbox to match the reference peak and correct the whole pattern to be corrected of displacement errors
3. Within scan data toolbox, select “peak”. Conduct a peak search and append to list.



4. Remove reference peaks from the list and create a d-spacing intensity file (DIF)
  - a. Since the standard is known, leaving it in would expand the incorrect possibilities of phase matches
5. Search/Match in the toolbox to find possible phase matches
  - a. If chemistry is known, the possible elements should be included and the impossible elements excluded from the search
6. Sort through the most probable matches to find likely phases present.
  - a. Confirm possible phases using Topas
  - b. As likely phases are confirmed, those peaks may be excluded and steps 4-6 repeated until all peaks are accounted for.

#### Quantitative Reitveld Structure Refinement Using Topas 4.2:

*Adapted from PowerPoint slides provided in UNLV's ME695: XRD/SEM course.*

1. Import .raw scan file to Topas
2. In the emission profile tab, load the emission profile for the Bruker D8 (CuK $\alpha$ 1)
3. Set parameters
  - a. Chebychev "yes" (always refine)
  - b. Polynomial order 5-7
  - c. Set goniometer radii (mm)
    - i. Primary radius (mm) = 435
    - ii. Secondary radius (mm) = 217.5
  - d. Equatorial Convolutions

- i. Select linear PSD
  - e. Peak shift
    - i. Select sample displacement refinement
  - f. Intensity corrections
    - i. Set LP factor to 27.3 (Fix)
- 4. Load CIF files, as phases are discovered using FindIt/Eva
  - a. Refine lattice parameters to  $\pm 0.03 \text{ \AA}$
  - b. Refine crystal size between 40 to 10000  $\text{\AA}$
- 5. "Run" 1 iteration. If no errors, run all iterations to refinement.
- 6. Add in phases one at a time to confirm phase found using EVA/FindIt and repeat steps 4-6 as needed.
- 7. Phase analysis may be complete when all peaks are accounted for.
- 8. More complex refinement can be completed using Topas if needed.

### **A.3 Scanning Electron Microscopy Testing and Analysis Procedure**

#### **A.3.1 Testing Procedure:**

*Adapted from PowerPoint slides provided in UNLV's ME695: XRD/SEM course.*

1. Sample must be properly prepared. Sample must fully dried and coated with gold or carbon if not conductive. Gloves should be used for preparation, as skin oils can degrade the equipment.
2. Sample should be mounted on SEM stage using carbon tape to prevent charging of material. It should be loaded into the vacuum chamber with 2 cm of clearance using

vent and evacuation protocol to limit the time when the vacuum chamber is open to the atmosphere.

3. Ensure equipment variables are at appropriate starting values. These may need to be altered for image quality. Press the HT (high tension) button to begin imaging after the below variables have been set.
  - a. Select secondary electron imaging (SEI)
  - b. Set magnification to x35, if not already set. This will likely be changed but beginning with a low magnification allows the user to easily find the sample.
  - c. Set voltage to 15 kV
  - d. Aperture was set to "2"
  - e. Spot size was set to 40
4. Find the sample and select a site of interest using the X and Y controls. Scan 2 mode is recommended for this step for speed and to limit sample degradation.
5. Magnify (using the magnification knob to the appropriate level of detail. Image quality corrections may be required. Image quality corrections include:
  - a. Previously mentioned variables
  - b. Contrast and brightness
  - c. Focus (coarse and fine)
  - d. Working distance
  - e. Objective lens wobbler
6. Change mode to Scan 3 or 4 for improved quality. Make any further quality adjustments needed, then select "freeze" to capture the image and save with a scale bar.

7. Repeat steps 4-6 until imaging is complete. Turn off HT, center the X and Y control and return magnification to X35 for the next user. Remove the sample from the vacuum chamber and return the chamber to vacuum.
  - a. For thin film perovskites, it is recommended images are taken at a few magnifications in order to understand the surface morphology, visible defects and uniformity of the imaged sample.

## **A.4 Energy Dispersive Spectroscopy**

### **A.4.1 Use Procedure:**

*Adapted from PowerPoint slides provided in UNLV's ME695: XRD/SEM course.*

1. Steps 1-5 should be completed from the SEM Procedure guidelines.
2. The detection method should be changed to BEI (backscatter electron imaging).
3. The backscatter detector should be moved into the vacuum tube.
4. A project site of interest can now be selected, allowing an image to be taken.
5. Sites of interest can now be selected on the image using the computer mouse. Intensity counts and x-ray energy will be taken at the selected sites.
6. The user should confirm elements in the resulting report. Elements which are certainly present should be confirmed or added (if not present). Elements which are certainly not present may be removed. Care should be taken during this process; when in doubt, leave an element in.
  - a. An example of an appropriate removal is when a sample made with platinum, cesium, iodine, and common element solvents shows zirconium but no platinum. The  $L\alpha$  characteristic x-ray for zirconium (2.042 KeV) is close to the M

characteristic x-ray for platinum (2.048 KeV), and the software is very likely incorrectly identifying the presence of zirconium.

- b. An example of an inappropriate time to remove an element is when it is plausible it may be present, even if characteristic x-rays are close to an expected element. Removing these elements may be removing key information. Choose nearby sites of interest and confirm the existence of elements using alternate methods if needed.
7. Steps 2-6 can be repeated until complete. Remove the backscatter detector, turn off HT, center the X and Y control and return magnification to X35 for the next user. Remove the sample from the vacuum chamber and return the chamber to vacuum.

## **A.5 Current-Voltage Testing and Analysis Procedure**

### **A.5.1 Use Procedure:**

*For light measurements:*

1. Turn on the Abet Solar Simulator lamp, ensuring the shutter is closed. Let lamp warm up for 15 minutes prior to use.
2. Connect the leads to the silicon calibration cell and place on the center of the stage.
3. Open the lamp shutter. Adjust the lamp height until the calibration cell reads 100 mV.  
Turn the lamp shutter off.
4. Open lab view.
5. Connect device to be tested to the Keithly.
6. Open the lamp shutter. Immediately run program.
7. Close shutter and disconnect device. Repeat steps 5-7 as needed.

8. Close shutter, turn off the lamp and turn of the Keithly.

*For Dark measurements:*

1. Open lab view.
2. Connect device to be tested to the Keithly.
3. Cover test device loosely with a cloth to reduce ambient light. Run the program.
4. Disconnect device. Repeat steps 2-4 as needed.
5. Turn of the Keithley.

### **A.5.2 Diode and Photovoltaic Background**

■ P-n junction diode in photovoltaics:

The most functional and important component of a solar photovoltaic device is the p-n junction diode. A p-n junction diode is formed when an n-type semiconductor material and a p-type semiconductor material are brought into contact. The n-side electron concentration gradient allows the diffusion of electron majority carriers into the p-side, leaving behind positively charged ions, or “holes”, which are immobile. Similarly, the p-side hole concentration gradient allows the diffusion of the hole majority carriers across the p-n junction from the p-side to the n-side, leaving behind immobile ions with a negative charge.

A built-in electric field results from the separation of ions on opposing end of the p-n junction; this field applies a force on the electron and hole carriers in the opposite direction to the diffusion, known as a “drift force”. The diffusion and drift from the p-side and n-side balance and an equilibrium is achieved where the Fermi-energy level within the entire device is

constant, resulting in bends in the conduction and valence bands at the material junction. These bends create a potential barrier, (known as the built-in voltage,  $V_{bi}$ ), which is “seen” by electrons in the conduction band of the n-side as they traverse to p-side. The region is called space-charge-region (this is also commonly referred to as the depletion region). When a semiconducting device is in thermal equilibrium, this region is nearly depleted of mobile carriers and only has immobile positive and negative ions on the p and n sides.

Depending on the materials that form the junction, a p-n junction can be a homojunction or heterojunction. Heterojunctions are formed as two types of dissimilar semiconducting materials with different bandgaps and conductivity are in contact, as is the case with the material developed in this effort. Homojunctions are created when doped n-type and p-type layers of the same material come into contact, as is the case with most conventional silicon devices.

When a p-n junction is in forward bias, the energy potential in the device is reduced, allowing increased current will flow across the junction. However, the potential increases and less current flows through the devices p-n junction as the junction bias is reversed, creating a one way current gate through the material. The p-n junction current-voltage characteristics for diode are described by Equation 16:

**Equation 16: P-n junction diode current-voltage characteristics.**

$$J = J_0 \left[ \exp\left(\frac{eV}{AkT}\right) - 1 \right]$$

Where,  $A$  is diode factor,  $J_0$  is the dark saturation current density,  $T$  is temperature and  $k$  is Boltzmann constant.

### ■ Important Parameters of a Photovoltaic Device:

A solar cell is a p-n junction diode placed which is under illumination. As the device is illuminated, the J-V curve will be increased by the photo-generated current density ( $J_L$ ) as described by Equation 17:

#### **Equation 17: P-n junction diode current-voltage characteristics with photo-generated current density.**

$$J = J_0 \left[ \exp\left(\frac{eV}{AkT}\right) - 1 \right] - J_L$$

The parameters that describe a photovoltaic device performance are:

- Short-circuit current density,  $J_{sc}$  – the current density that flows through the junction under illumination at zero applied bias. Ideally, the short circuit current is equal to the photo-generated current density,  $J_L$ .
- Open-circuit voltage,  $V_{oc}$  – the voltage across the p-n junction while the device is illuminated and there is no current through the junction is zero (see Equation 18).
- Fill-factor, FF – the ratio of the power obtained to the maximum power possible given the measured short circuit current density and the measured open circuit voltage.
- Conversion efficiency,  $\eta$  – the total power generated as a proportion to the incident power provided by the solar spectrum.



**Equation 18: Open circuit voltage of a p-n junction diode.**

$$V_{oc} = \frac{AkT}{e} \ln \left( \frac{J_L}{J_0} + 1 \right)$$

To determine these important factors, the J-V characteristics can be analyzed under dark or light conditions. The J-V characteristics of a photovoltaic cell under illumination with series resistance (“parasitic resistance”) as described by Equation 19, where  $G = 1/R_{sh}$  is the shunt conductance.

**Equation 19: J-V characteristics of a photovoltaic device under illumination with photo-generated current and series resistance.**

$$J = J_0 \left[ \exp \left( \frac{e(V - R_s J)}{AkT} \right) - 1 \right] - J_L + (V - R_s J)G$$

■ Current-Voltage curve (J-V) analysis

Shunt resistance, series resistance, dark saturation current and diode ideality factor are extracted from the current-voltage curves. Our preliminary device fabrication has resulted in good dark J-V behavior, however, significant voltage dependent current collection is observed in light J-V curves. The analysis of dark J-V curves allows calculation of shunt resistance,  $R_{sh}$ , equal to the inverse of the shunt conductance,  $G$ , from the plot of  $dJ/dV$  and the voltage applied to the device. The relation can be found in Equation 20.

**Equation 20: The relation for the determination of the shunt resistance.**

$$\frac{dJ}{dV} = J_0 \frac{d}{dV} \left[ \exp\left(\frac{e(V - R_s J)}{AkT}\right) - 1 \right] - \frac{dJ_L}{dV} + G$$

Close to the short circuit current and under reverse bias conditions the exponential containing term in Equation 20 is or approaches zero and is therefore negligible. For dark measurements photo-current  $J_L$  is zero, the equation reduces to Equation 21:

**Equation 21: Simplified version of Equation 20 for dark measurements.**

$$\frac{dJ}{dV} \sim G$$

Using the plot of  $dV/dJ$ , the series resistance,  $R_s$ , can be determined. Dark saturation current  $J_0$  and ideality factor  $A$  are calculated. For the dark curves J-GV vs. V-JRs semi-logarithmic plot, intercept gives  $J_0$  and slope gives  $e/AkT$  to determine diode quality factor.

## APPENDIX B: MOLARITY CALCULATIONS

### B.1 Version 1: Cs<sub>2</sub>PtI<sub>6</sub> with PtI<sub>4</sub> and CsI

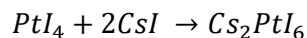
#### B.1.1 Equations

Molarity Definition:

$$\text{Molarity} = \frac{\text{Volume}}{\text{Moles}}$$

#### B.1.2 Given Information:

Chemical Equation:



Molecular Weight PtI<sub>4</sub>: 702.70 g/mol

Molecular Weight CsI: 259.81 g/mol

Molecular Weight Cs<sub>2</sub>PtI<sub>6</sub>: 1222.32 g/mol

Molarity: 0.25

Volume of Solvent: 1 mL

#### B.1.3 Calculations

Moles of Cs<sub>2</sub>PtI<sub>6</sub> Solute needed:

$$\text{Moles Cs}_2\text{PtI}_6 = \frac{1 * 10^{-3} [L]}{0.25}$$

$$\text{Moles } Cs_2PtI_6 = 0.00025$$

Amount of  $PtI_4$  reactant:

- 1 Mol of  $PtI_4$  for 1 Mol of  $Cs_2PtI_6$
- $\text{Weight } PtI_4 [g] = 0.00025 [mol] * 702.70 \left[ \frac{g}{mol} \right]$
- $\text{Weight } PtI_4 = 0.1757 \frac{g PtI_4}{ml \text{ of solution}}$

Amount of  $CsI$  reactant:

- 2 Mol of  $CsI$  for 1 Mol of  $Cs_2PtI_6$
- $\text{Weight } CsI [g] = 0.00025 [mol] * 2 * 259.81 \left[ \frac{g}{mol} \right]$
- $\text{Weight } CsI = 0.1299 \frac{g CsI}{ml \text{ of solution}}$

## B.2 Version 2: $Cs_2PtI_6$ with $PtI_2$ and $CsI$

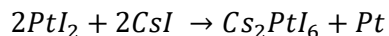
### B.2.1 Equations

Molarity Definition:

$$\text{Molarity} = \frac{\text{Volume}}{\text{Moles}}$$

### B.2.2 Given Information:

Chemical Equation:



Molecular Weight  $PtI_2$ : 448.89 g/mol

Molecular Weight  $CsI$ : 259.81 g/mol

**Molecular Weight** Cs<sub>2</sub>PtI<sub>6</sub>: 1222.32 g/mol

Molarity: 0.25

Volume of Solvent: 1 mL

### B.2.3 Calculations

Moles of Cs<sub>2</sub>PtI<sub>6</sub> Solute needed:

$$\text{Moles } Cs_2PtI_6 = \frac{1 * 10^{-3}[L]}{0.25}$$

$$\text{Moles } Cs_2PtI_6 = 0.00025$$

Amount of PtI<sub>2</sub> reactant:

- 2 Mol of PtI<sub>2</sub> for 1 Mol of Cs<sub>2</sub>PtI<sub>6</sub>
- **Weight PtI<sub>2</sub> [g] = 0.00025 [mol] \* 448.89  $\left[\frac{g}{mol}\right]$**
- **Weight PtI<sub>2</sub> = 0.2244  $\frac{g PtI_2}{ml \text{ of solution}}$**

Amount of CsI reactant:

- 2 Mol of CsI for 1 Mol of Cs<sub>2</sub>PtI<sub>6</sub>
- **Weight CsI [g] = 0.00025 [mol] \* 2 \* 259.81  $\left[\frac{g}{mol}\right]$**
- **Weight CsI = 0.1299  $\frac{g CsI}{ml \text{ of solution}}$**

Notes:

- There is an extra mole of platinum in the Version 2 of the calculation. This can also be used for a perfect  $ABX_3$  reaction.
- Molarities and reactants are varied in many experiments. This calculation describes the process used to determine solute content.

## APPENDIX C: POWDER XRD TOPAS REPORTS

### C.1 Powder XRD Pattern for cesium platinum iodide derived from solution processed PtI<sub>4</sub> and CsI

File 1 : "C:\DIFFDAT1\dakota\raw file\160\_DS\_CsI PtI4\_11 Feb 2019.raw"

Range Number : 1

R-Values

Rexp : 3.65 Rwp : 15.75 Rp : 10.25 GOF : 4.31

Rexp` : 9.67 Rwp` : 41.66 Rp` : 47.99 DW : 0.29

Quantitative Analysis - Rietveld

Phase 1 : Cs<sub>2</sub>PtI<sub>6</sub>\_Cubic 87(12) %

Phase 2 : Cs<sub>2</sub>PtI<sub>6</sub>\_Tetra 13(12) %

Background

Chebyshev polynomial, Coefficient 0 833.5(38)

1 -1214.6(54)

2 647.9(47)

3 -252.1(40)

4 80.7(30)

5 -23.6(24)

Instrument

Primary radius (mm) 435

Secondary radius (mm) 217.5

Linear PSD 2Th angular range (°) 4

FDS angle (°) 1

Corrections

Specimen displacement -0.3052(20)

LP Factor 27.3

Structure 1

Phase name Cs<sub>2</sub>PtI<sub>6</sub>\_Cubic

R-Bragg 11.878  
 Spacegroup Fm-3m  
 Scale 0.00000103(13)  
 Cell Mass 4889.236  
 Cell Volume (Å<sup>3</sup>) 1466.06(15)  
 Wt% - Rietveld 87(12)  
 Crystallite Size  
   Cry size Lorentzian (nm) 0(1100000)  
 Strain  
   Strain L 0.000(15)  
   Strain G 0.000(27)  
 Crystal Linear Absorption Coeff. (1/cm) 1554.09(16)  
 Crystal Density (g/cm<sup>3</sup>) 5.53781(58)  
 Preferred Orientation (Dir 1 : 1 1 1) 0.207(61)  
                                   (Dir 2 : 2 2 2) 1(76)  
   Fraction of Dir 1 0.24(18)  
 PVII peak type  
   FWHM = a + b/Cos(Th) + c Tan(Th)  
     a 0.000(40)  
     b 0.000(41)  
     c 0.050(13)  
   Exponent m = 0.6+ma+mb/Cos(Th)+mc/Tan(Th)  
     ma 0.0(16)  
     mb 0.0(13)  
     mc 0.151(58)  
 Lattice parameters  
   a (Å) 11.36015(40)

Site	Np	x	y	z	Atom	Occ	Beq
Cs1	8	0.25000	0.25000	0.25000	Cs+1	1	1
Pt1	4	0.00000	0.00000	0.00000	Pt+4	1	1
I1	24	0.23530	0.00000	0.00000	I-1	1	1

#### Structure 2

Phase name Cs<sub>2</sub>PtI<sub>6</sub>\_Tetra  
 R-Bragg 14.293  
 Spacegroup P1



Scale 0.000022(24)  
 Cell Mass 1222.309  
 Cell Volume (Å<sup>3</sup>) 0(2300000)  
 Wt% - Rietveld 13(12)  
 Crystallite Size  
   Cry size Lorentzian (nm) 160(340)  
 Crystal Linear Absorption Coeff. (1/cm) 0(8200000)  
 Crystal Density (g/cm<sup>3</sup>) 5(29000)  
 Preferred Orientation (Dir 1 : 2 1 1) 1(17)  
 PVII peak type  
   FWHM = a + b/Cos(Th) + c Tan(Th)  
     a 0.0(35)  
     b 0.0(36)  
     c 0.0(12)  
   Exponent m = 0.6+ma+mb/Cos(Th)+mc/Tan(Th)  
     ma 0.0(41)  
     mb 0.0(35)  
     mc 0.02(14)  
 Lattice parameters  
   a (Å) 8.2(63)  
   b (Å) 8(13000)  
   c (Å) 8(13000)  
   alpha (°) 60(26)  
   beta (°) 0(490000)  
   gamma (°) 0(490000)

Site	Np	x	y	z	Atom	Occ	Beq
I1	1	0.76871	0.23129	0.76871	I	1	1
I2	1	0.23129	0.23129	0.76871	I	1	1
I3	1	0.76871	0.23129	0.23129	I	1	1
I4	1	0.23129	0.76871	0.23129	I	1	1
I5	1	0.23129	0.76871	0.76871	I	1	1
I6	1	0.76871	0.76871	0.23129	I	1	1
Cs1	1	0.25000	0.25000	0.25000	Cs	1	1
Cs2	1	0.75000	0.75000	0.75000	Cs	1	1
Pt1	1	0.00000	0.00000	0.00000	Pt	1	1

Peaks Phase 1

Phase name

Peaks Phase:0

## C.2 Powder XRD Pattern for cesium platinum iodide derived from solution processed PtI2 and CsI

Report

File 1 : "C:\DIFFDAT1\dakota\raw file\169\_DS\_6 Feb 2019\_dd\_ptI2CsI.raw"

Range Number : 1

R-Values

Rxp : 3.75 Rwp : 18.75 Rp : 12.32 GOF : 5.00

Rxp` : 17.55 Rwp` : 87.71 Rp` : 90.57 DW : 0.12

Quantitative Analysis - Rietveld

Phase 1 : Cs<sub>2</sub>PtI<sub>6</sub> 80(78) %

Phase 2 : CsPtI<sub>6</sub>\_Tetra 20(78) %

Background

Chebyshev polynomial, Coefficient 0 922.4(43)

1 -1320.7(71)

2 749.9(62)

3 -361.1(58)

4 188.6(52)

5 -109.2(49)

6 54.4(37)

7 -11.2(29)

Instrument

Primary radius (mm) 435

Secondary radius (mm) 217.5

Linear PSD 2Th angular range (°) 4  
 FDS angle (°) 1

Corrections

Specimen displacement -0.040(47)  
 LP Factor 27.3

Structure 1

Phase name Cs<sub>2</sub>PtI<sub>6</sub>  
 R-Bragg 7.625  
 Spacegroup Fm-3m  
 Scale 0.00000018(16)  
 Cell Mass 4889.236  
 Cell Volume (Å<sup>3</sup>) 1472.3(31)  
 Wt% - Rietveld 80(78)  
 Crystallite Size  
 Cry size Lorentzian (nm) 0(8800000)

Strain

Strain L 0.15(37)  
 Strain G 0.07(36)

Crystal Linear Absorption Coeff. (1/cm) 1547.5(33)

Crystal Density (g/cm<sup>3</sup>) 5.514(12)

Preferred Orientation (Dir 1 : 4 4 4) 0.28(48)

(Dir 2 : 2 2 2) 0.9(40)

Fraction of Dir 1 0.4(18)

PVII peak type

FWHM = a + b/Cos(Th) + c Tan(Th)

a 0.01(66)

b 0.01(70)

c 0.01(25)

Exponent m = 0.6+ma+mb/Cos(Th)+mc/Tan(Th)

ma 0.1(14)

mb 0.0(12)

mc 0.018(45)

Lattice parameters

a (Å) 11.3763(80)

Site Np x y z Atom Occ Beq

Cs1	8	0.25000	0.25000	0.25000	Cs+1	1	1
Pt1	4	0.00000	0.00000	0.00000	Pt+4	1	1
I1	24	0.23530	0.00000	0.00000	I-1	1	1

## Structure 2

Phase name	CsPtI6_Tetra
R-Bragg	8.990
Spacegroup	P1
Scale	0.0000006(30)
Cell Mass	1222.309
Cell Volume (Å <sup>3</sup> )	410(290)
Wt% - Rietveld	20(78)
Crystallite Size	
Cry size Lorentzian (nm)	0(1600000)
Crystal Linear Absorption Coeff. (1/cm)	1400(1000)
Crystal Density (g/cm <sup>3</sup> )	5.0(36)
Preferred Orientation (Dir 1 : 2 0 2)	9(34)
PV_TCHZ peak type	
U	0.4(34)
V	0.2(17)
W	-0.08(21)
Z	0
X	0.23(61)
Y	0
Lattice parameters	
a (Å)	8.3(25)
b (Å)	8.33(10)
c (Å)	8.3(25)
alpha (°)	60(49)
beta (°)	60.2(39)
gamma (°)	60(61)

Site	Np	x	y	z	Atom	Occ	Beq
I1	1	0.76871	0.23129	0.76871	I	1	1
I2	1	0.23129	0.23129	0.76871	I	1	1
I3	1	0.76871	0.23129	0.23129	I	1	1
I4	1	0.23129	0.76871	0.23129	I	1	1

I5	1	0.23129	0.76871	0.76871	I	1	1
I6	1	0.76871	0.76871	0.23129	I	1	1
Cs1	1	0.25000	0.25000	0.25000	Cs	1	1
Cs2	1	0.75000	0.75000	0.75000	Cs	1	1
Pt1	1	0.00000	0.00000	0.00000	Pt	1	1

Plots

### C.3 Powder XRD Pattern for spin coated cesium platinum iodide derived from solution processed PtI2 and CsI

Report

File 1 : "C:\DIFFDAT1\dakota\raw file\Vanesa\25\_VE\_PtI2 CsI\_DMF DMSO\_13 Mar 19.raw"

Range Number : 1

R-Values

Rexp : 4.07 Rwp : 10.46 Rp : 7.38 GOF : 2.57  
 Rexp` : 25.63 Rwp` : 65.76 Rp` : 62.30 DW : 0.32

Quantitative Analysis - Rietveld

Phase 1 : Cs <sub>2</sub> PtI <sub>6</sub> _Cubic	59.1(75) %
Phase 2 : Cs <sub>2</sub> PtI <sub>6</sub> _Tetra	40.9(75) %

Background

Chebyshev polynomial, Coefficient 0	874.5(22)
1	-1402.6(31)
2	925.7(28)
3	-501.1(24)
4	224.5(20)
5	-86.9(15)

6 30.0(12)

#### Instrument

Primary radius (mm) 435  
Secondary radius (mm) 217.5  
Linear PSD 2Th angular range (°) 4  
FDS angle (°) 1

#### Corrections

Specimen displacement -0.319(24)  
LP Factor 27.3

#### Structure 1

Phase name Cs<sub>2</sub>PtI<sub>6</sub>\_Cubic  
R-Bragg 2.689  
Spacegroup Fm-3m  
Scale 0.00000079(24)  
Cell Mass 4889.236  
Cell Volume (Å<sup>3</sup>) 1459.8(42)  
Wt% - Rietveld 59.1(75)  
Crystallite Size  
Cry size Lorentzian (nm) 40(34)  
Strain  
Strain L 5.0(10)  
Strain G 0.0(24)  
Crystal Linear Absorption Coeff. (1/cm) 1560.8(45)  
Crystal Density (g/cm<sup>3</sup>) 5.562(16)  
Preferred Orientation (Dir 1 : 1 1 1) 0.29(49)  
(Dir 2 : 2 2 2) 1.42(10)  
Fraction of Dir 1 0.12(61)  
Lattice parameters  
a (Å) 11.344(11)

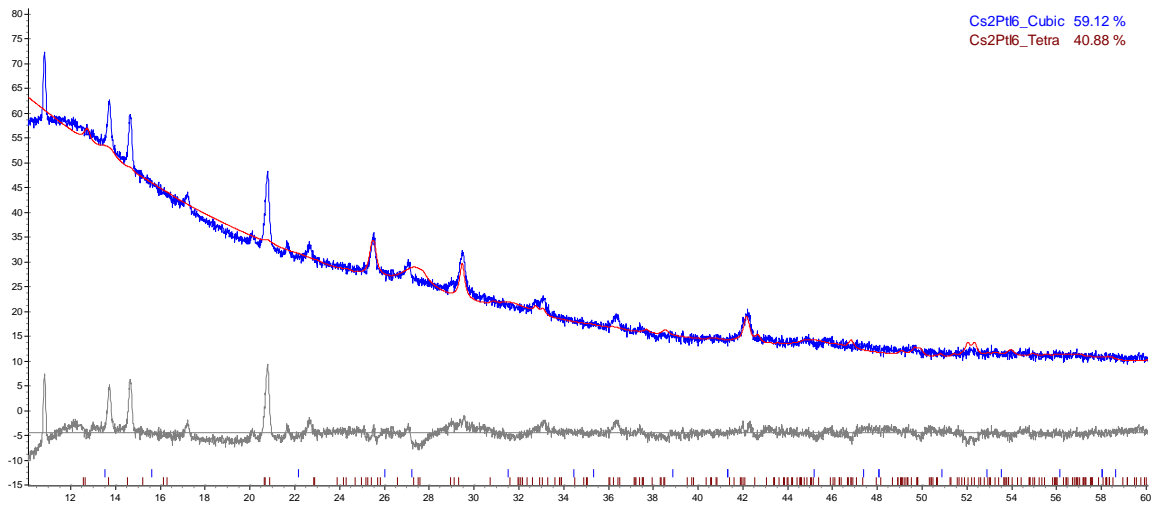
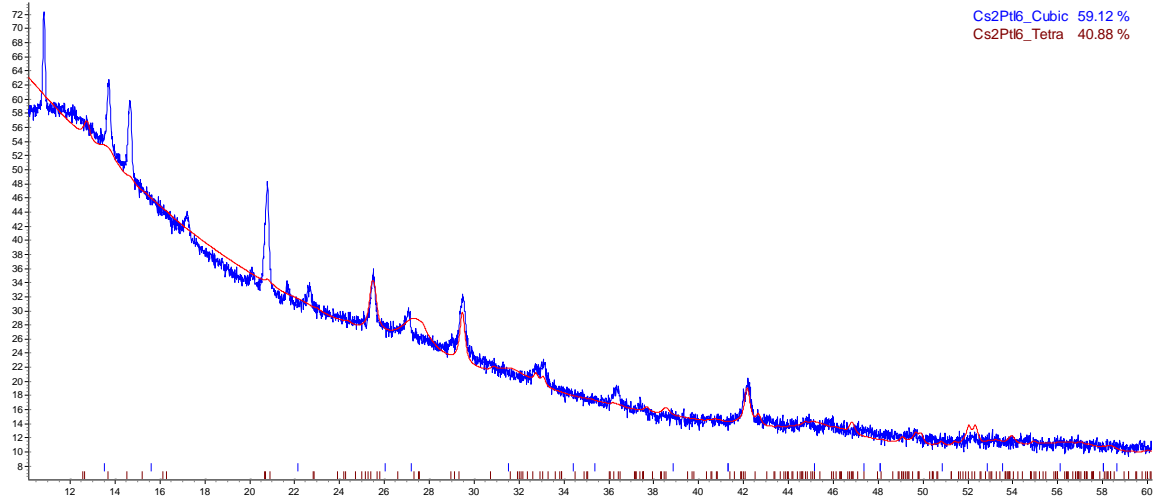
Site	Np	x	y	z	Atom	Occ	Beq
Cs1	8	0.25000	0.25000	0.25000	Cs+1	1	1
Pt1	4	0.00000	0.00000	0.00000	Pt+4	1	1
I1	24	0.23530	0.00000	0.00000	I-1	1	1

## Structure 2

Phase name	Cs <sub>2</sub> PtI <sub>6</sub> _Tetra
R-Bragg	6.195
Spacegroup	P1
Scale	0.00000854(47)
Cell Mass	1222.309
Cell Volume (Å <sup>3</sup> )	373.00(49)
Wt% - Rietveld	40.9(75)
Crystallite Size	
Cry size Lorentzian (nm)	40.0(30)
Crystal Linear Absorption Coeff. (1/cm)	1527.1(20)
Crystal Density (g/cm <sup>3</sup> )	5.4415(72)
Preferred Orientation (Dir 1 : 2 1 1)	1.683(54)
Lattice parameters	
a (Å)	7.1260(67)
b (Å)	8.5689(44)
c (Å)	8.6482(46)
alpha (°)	59.927(31)
beta (°)	59.776(49)
gamma (°)	60.157(45)

Site	Np	x	y	z	Atom	Occ	Beq
I1	1	0.76871	0.23129	0.76871	I	1	1
I2	1	0.23129	0.23129	0.76871	I	1	1
I3	1	0.76871	0.23129	0.23129	I	1	1
I4	1	0.23129	0.76871	0.23129	I	1	1
I5	1	0.23129	0.76871	0.76871	I	1	1
I6	1	0.76871	0.76871	0.23129	I	1	1
Cs1	1	0.25000	0.25000	0.25000	Cs	1	1
Cs2	1	0.75000	0.75000	0.75000	Cs	1	1
Pt1	1	0.00000	0.00000	0.00000	Pt	1	1

## Plots





# APPENDIX D: RAW EDS DATA

Project 1
**PtI4+2CsI in DMF/DMSO**
1/17/2019 12:46:45 PM

Spectrum processing :

No peaks omitted

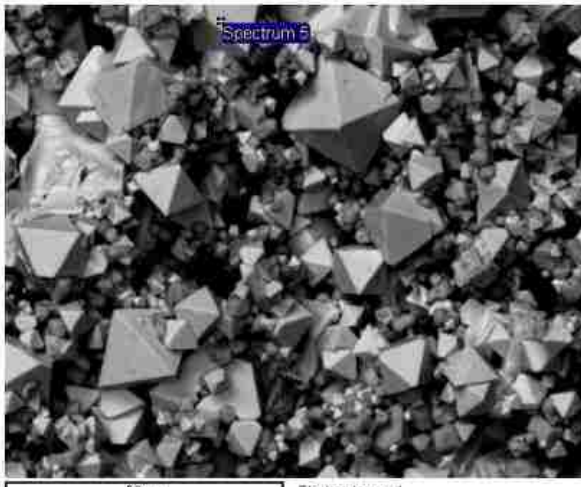
Processing option : All elements analyzed (Normalised)

Number of iterations = 3

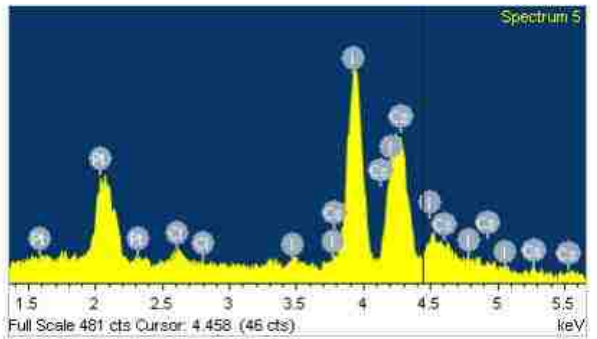
Standard :

- C CaCO3 1-Jun-1999 12:00 AM
- O SiO2 1-Jun-1999 12:00 AM
- Cl KCl 1-Jun-1999 12:00 AM
- I Not defined 1-Jun-1999 12:00 AM
- Cs Not defined 1-Jun-1999 12:00 AM
- Pt Pt 1-Jun-1999 12:00 AM

Element	Weight%	Atomic%
C K	3.02	23.91
O K	1.16	6.92
Cl K	0.97	2.61



50µm Electron Image 1



Full Scale 481 cts Cursor: 4.458 (46 cts)

**Inca**

Comment:

I L	59.24	44.46
Cs L	20.68	14.82
Pt M	14.93	7.29
Totals	100.00	

Project 1

2PtI2+2CsI in DMF/DMSO

6/7/2018 12:49:46 PM

Spectrum processing :

No peaks omitted

Processing option : All elements analyzed (Normalised)

Number of iterations = 3

Standard :

O SiO2 1-Jun-1999 12:00 AM

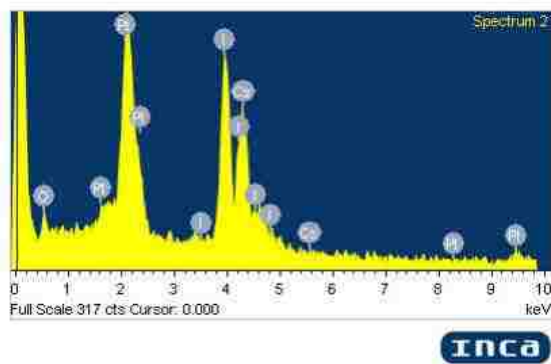
I Not defined 1-Jun-1999 12:00 AM

Cs Not defined 1-Jun-1999 12:00 AM

Pt Pt 1-Jun-1999 12:00 AM

Element	Weight%	Atomic%
O K	3.19	22.43
I L	55.60	49.25
Cs L	16.96	14.34
Pt M	24.25	13.97

Comment:



Project 1

2PtI2+2CsI in DMF/DMSO- on 1.5 mm crystal

2/14/2019 1:00:47 PM

Spectrum processing :

No peaks omitted

Processing option : All elements analyzed (Normalised)

Number of iterations = 3

Standard :

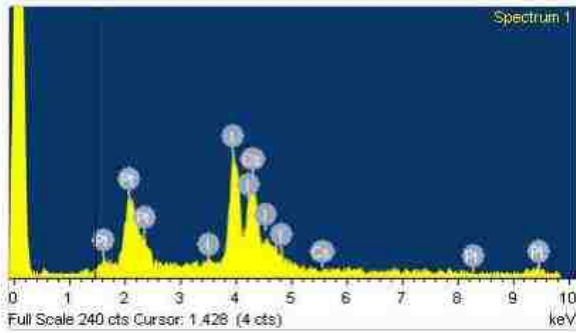
I Not defined 1-Jun-1999 12:00 AM

Cs Not defined 1-Jun-1999 12:00 AM

Pt Pt 1-Jun-1999 12:00 AM

Element	Weight%	Atomic%
I L	62.63	67.21
Cs L	20.52	21.02
Pt M	16.85	11.76
Totals	100.00	

Comment:



Project 1 **2PtI2+2CsI in DMF/DMSO- on dendrite structure near crystal** 3/19/2019 1:01:10 PM

Spectrum processing :

No peaks omitted

Processing option : All elements analyzed (Normalised)

Number of iterations = 3

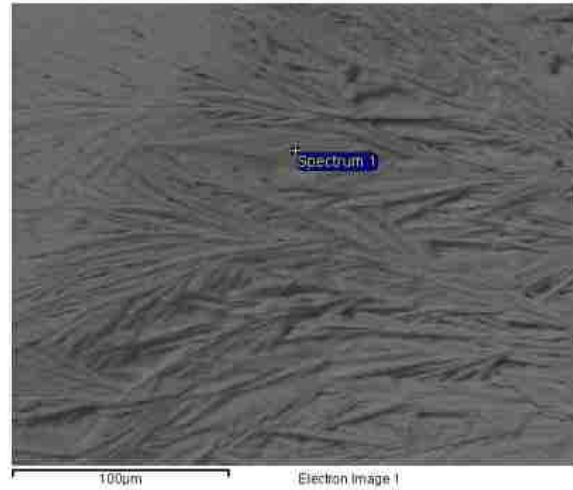
Standard :

S : FeS2: 1-Jun-1999 12:00 AM

I : Not defined: 1-Jun-1999 12:00 AM

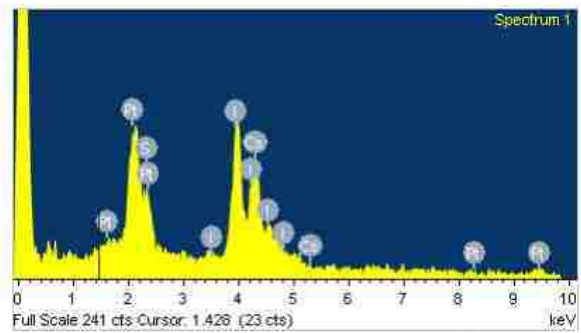
Cs : Not defined: 1-Jun-1999 12:00 AM

Pt : Pt : 1-Jun-1999 12:00 AM



Element	Weight%	Atomic%
S K	5.19	19.40
I L	55.73	52.60
Cs L	13.95	12.57
Pt M	25.13	15.43

Comment:



## APPENDIX E: SOLUTE COSTS

Costs are from Sigma-Aldrich unless otherwise stated. Costs were determined in February 2019.

Cost by mass was calculated from the given cost and mass for each solute. Solute costs are subject to change and differ based on amount purchased.

**Table 15: Solute costs as used in Chapter 3. Determined February 2019.**

<b>Solute</b>	<b>Molecular weight [g/mol]</b>	<b>Weight [g]</b>	<b>Price [\$]</b>	<b>Cost by Mass [\$g]</b>	<b>Purity [%]</b>	<b>CAS</b>
<b>CsI</b>	259.81	25	72.9	2.916	0.99900	7789-17-5
<b>GeI2</b>	326.45	1	153	153	0.99800	13573-08-5
<b>GeI4</b>	580.26	5	108	21.6	0.99990	13450-95-8
<b>KI</b>	166	100	124	1.24	0.99500	7681-11-0
<b>MAI</b>	158.97	10	268	26.8	0.99000	14965-49-2
<b>PbI2</b>	461.0	50	153	3.06	0.99999	10101-63-0
<b>PtI2</b>	448.89	1	128	128	0.98000	7790-39-8
<b>PtI4</b>	702.7	5	550	110	0.99900	Alpha Aesar
<b>RbI</b>	212.37	10	53.5	5.35	0.99900	7790-29-6
<b>SnI2</b>	372.52	1	125	125	0.99999	10294-70-9
<b>SnI4</b>	626.33	5	168	33.6	0.99999	7790-47-8
<b>TeI4</b>	635.22	5	47	9.4	0.99000	87795-06 Alfa Aesar

## REFERENCES

- [1] "U.S. Energy Information Administration (EIA) - Electricity." [Online]. Available: <https://www.eia.gov/electricity/>. [Accessed: 20-Mar-2019].
- [2] "4 Charts That Show Renewable Energy is on the Rise in America | Department of Energy." [Online]. Available: <https://www.energy.gov/eere/articles/4-charts-show-renewable-energy-rise-america>. [Accessed: 20-Mar-2019].
- [3] T. Unold and H. W. Schock, "Nonconventional (Non-Silicon-Based) Photovoltaic Materials," *Annu. Rev. Mater. Res.*, vol. 41, no. 1, pp. 297–321, Aug. 2011.
- [4] F. Dimroth and S. Kurtz, "High-Efficiency Multijunction Solar Cells," *MRS Bull.*, vol. 32, no. 03, pp. 230–235, Mar. 2007.
- [5] A. Shah, P. Torres, R. Tscharnner, N. Wyrsh, and H. Keppner, "Photovoltaic technology: the case for thin-film solar cells," *Science*, vol. 285, no. 5428, pp. 692–8, Jul. 1999.
- [6] A. Kojima, K. Teshima, Y. Shirai, and T. Miyasaka, "Organometal Halide Perovskites as Visible-Light Sensitizers for Photovoltaic Cells," *J. Am. Chem. Soc.*, vol. 131, no. 17, pp. 6050–6051, May 2009.
- [7] "Champion Photovoltaic Module Efficiency Chart | Photovoltaic Research | NREL." [Online]. Available: <https://www.nrel.gov/pv/module-efficiency.html>. [Accessed: 30-Mar-2019].
- [8] C. D. Bailie *et al.*, "Semi-transparent perovskite solar cells for tandems with silicon and CIGS," *Energy Environ. Sci.*, vol. 8, no. 3, pp. 956–963, Mar. 2015.
- [9] L. Kranz *et al.*, "High-Efficiency Polycrystalline Thin Film Tandem Solar Cells," *J. Phys. Chem. Lett.*, vol. 6, no. 14, pp. 2676–2681, Jul. 2015.
- [10] T. Todorov *et al.*, "Monolithic Perovskite-CIGS Tandem Solar Cells via In Situ Band Gap Engineering," *Adv. Energy Mater.*, vol. 5, no. 23, p. 1500799, Dec. 2015.
- [11] Y. (Michael) Yang *et al.*, "Multilayer Transparent Top Electrode for Solution Processed Perovskite/Cu(In,Ga)(Se,S)<sub>2</sub> Four Terminal Tandem Solar Cells," *ACS Nano*, vol. 9, no. 7, pp. 7714–7721, Jul. 2015.
- [12] W. S. Yang *et al.*, "High-performance photovoltaic perovskite layers fabricated through intramolecular exchange," *Science (80-. )*, vol. 348, no. 6240, pp. 1234–1237, Jun. 2015.
- [13] L. K. Ono, E. J. Juarez-Perez, and Y. Qi, "Progress on Perovskite Materials and Solar Cells with Mixed Cations and Halide Anions," *ACS Appl. Mater. Interfaces*, vol. 9, no. 36, pp. 30197–30246, Sep. 2017.
- [14] Z. C. Holman *et al.*, "23.6%-efficient monolithic perovskite/silicon tandem solar cells with improved stability," *Nat. Energy*, vol. 2, no. 4, 2017.
- [15] S. Chakraborty *et al.*, "Rational Design: A High-Throughput Computational Screening

- and Experimental Validation Methodology for Lead-Free and Emergent Hybrid Perovskites," *ACS Energy Lett.*, vol. 2, no. 4, pp. 837–845, Apr. 2017.
- [16] S. N. Habisreutinger, D. P. McMeekin, H. J. Snaith, and R. J. Nicholas, "Research Update: Strategies for improving the stability of perovskite solar cells," *APL Mater.*, vol. 4, no. 9, p. 091503, Sep. 2016.
- [17] M. Saliba *et al.*, "Cesium-containing triple cation perovskite solar cells: improved stability, reproducibility and high efficiency.," *Energy Environ. Sci.*, vol. 9, no. 6, pp. 1989–1997, Jun. 2016.
- [18] M. C. Weidman, M. Seitz, S. D. Stranks, and W. A. Tisdale, "Highly Tunable Colloidal Perovskite Nanoplatelets through Variable Cation, Metal, and Halide Composition," *ACS Nano*, vol. 10, no. 8, pp. 7830–7839, Aug. 2016.
- [19] D. P. McMeekin *et al.*, "A mixed-cation lead mixed-halide perovskite absorber for tandem solar cells," *Science (80-. )*, vol. 351, no. 6269, pp. 151–155, Jan. 2016.
- [20] S. Dastidar *et al.*, "High Chloride Doping Levels Stabilize the Perovskite Phase of Cesium Lead Iodide," *Nano Lett.*, vol. 16, no. 6, pp. 3563–3570, Jun. 2016.
- [21] F. Hao, C. C. Stoumpos, D. H. Cao, R. P. H. Chang, and M. G. Kanatzidis, "Lead-free solid-state organic–inorganic halide perovskite solar cells," *Nat. Photonics*, vol. 8, no. 6, pp. 489–494, Jun. 2014.
- [22] B.-W. Park, B. Philippe, X. Zhang, H. Rensmo, G. Boschloo, and E. M. J. Johansson, "Bismuth Based Hybrid Perovskites  $A_3Bi_2I_9$  (A: Methylammonium or Cesium) for Solar Cell Application," *Adv. Mater.*, vol. 27, no. 43, pp. 6806–6813, Nov. 2015.
- [23] G. Kapil *et al.*, "Investigation of Interfacial Charge Transfer in Solution Processed  $Cs_2SnI_6$  Thin Films," *J. Phys. Chem. C*, vol. 121, no. 24, pp. 13092–13100, Jun. 2017.
- [24] F. Hong, B. Saparov, W. Meng, Z. Xiao, D. B. Mitzi, and Y. Yan, "Viability of Lead-Free Perovskites with Mixed Chalcogen and Halogen Anions for Photovoltaic Applications," *J. Phys. Chem. C*, vol. 120, no. 12, pp. 6435–6441, Mar. 2016.
- [25] F. Guo *et al.*, "A two-step dry process for  $Cs_2SnI_6$  perovskite thin film," *Mater. Res. Lett.*, vol. 5, no. 8, pp. 540–546, Nov. 2017.
- [26] Y. Cai *et al.*, "Computational Study of Halide Perovskite-Derived  $A_2BX_6$  Inorganic Compounds: Chemical Trends in Electronic Structure and Structural Stability," *Chem. Mater.*, vol. 29, no. 18, pp. 7740–7749, Sep. 2017.
- [27] B. Saparov *et al.*, "Thin-Film Deposition and Characterization of a Sn-Deficient Perovskite Derivative  $Cs_2SnI_6$ ," *Chem. Mater.*, vol. 28, no. 7, pp. 2315–2322, Apr. 2016.
- [28] G. E. Eperon *et al.*, "Inorganic caesium lead iodide perovskite solar cells," *J. Mater. Chem. A*, vol. 3, no. 39, pp. 19688–19695, Sep. 2015.
- [29] M.-G. Ju *et al.*, "Earth-Abundant Nontoxic Titanium(IV)-based Vacancy-Ordered Double

- Perovskite Halides with Tunable 1.0 to 1.8 eV Bandgaps for Photovoltaic Applications,” *ACS Energy Lett.*, vol. 3, no. 2, pp. 297–304, Feb. 2018.
- [30] C. Wu *et al.*, “The Dawn of Lead-Free Perovskite Solar Cell: Highly Stable Double Perovskite Cs<sub>2</sub>AgBiBr<sub>6</sub> Film,” *Adv. Sci. (Weinheim, Baden-Wurttemberg, Ger.)*, vol. 5, no. 3, p. 1700759, 2018.
- [31] N. Sakai *et al.*, “Solution-Processed Cesium Hexabromopalladate(IV), Cs<sub>2</sub>PdBr<sub>6</sub>, for Optoelectronic Applications,” *J. Am. Chem. Soc.*, vol. 139, no. 17, pp. 6030–6033, May 2017.
- [32] Z. Xiao, Y. Zhou, H. Hosono, and T. Kamiya, “Intrinsic defects in a photovoltaic perovskite variant Cs<sub>2</sub>SnI<sub>6</sub>,” *Phys. Chem. Chem. Phys.*, vol. 17, no. 29, pp. 18900–18903, Jul. 2015.
- [33] C. J. Bartel *et al.*, “New tolerance factor to predict the stability of perovskite oxides and halides,” *Sci. Adv.*, vol. 5, no. 2, p. eaav0693, Feb. 2019.
- [34] V. M. Goldschmidt, “Die Gesetze der Krystallochemie,” *Naturwissenschaften*, vol. 14, no. 21, pp. 477–485, May 1926.
- [35] “N,N-Dimethylformamide | HCON(CH<sub>3</sub>)<sub>2</sub> - PubChem.” [Online]. Available: [https://pubchem.ncbi.nlm.nih.gov/compound/n\\_n-dimethylformamide#datasheet=LCSS](https://pubchem.ncbi.nlm.nih.gov/compound/n_n-dimethylformamide#datasheet=LCSS). [Accessed: 31-Mar-2019].
- [36] H. Borrmann, I. Persson, M. Sandström, and C. M. V. Stlhandske, “The crystal and liquid structures of N,N-dimethylthioformamide and N,N-dimethylformamide showing a stronger hydrogen bonding effect for C–H···S than for C–H···O†,” *J. Chem. Soc. Perkin Trans. 2*, no. 2, pp. 393–402, 2000.
- [37] “gamma-Butyrolactone | C<sub>4</sub>H<sub>6</sub>O<sub>2</sub> - PubChem.” [Online]. Available: <https://pubchem.ncbi.nlm.nih.gov/compound/gamma-Butyrolactone#datasheet=LCSS>. [Accessed: 31-Mar-2019].
- [38] “ISR-2600 for UV-2600/2700 ISR-2600Plus for UV-2600 Integrating Sphere Attachment INSTRUCTION MANUAL,” 2011.
- [39] “Time-Resolved Photoluminescence | CAPP – Centre for Advanced Photonics & Process Analysis.” [Online]. Available: <http://www.cappa.ie/advanced-research/techniques/time-resolved-photoluminescence/>. [Accessed: 31-Mar-2019].
- [40] D. Ma *et al.*, “A feasible method to measure the content of core and shell in heterostructural perovskite MOFs through differential scanning calorimetry,” 2018.
- [41] Y. Bi, E. M. Hutter, Y. Fang, Q. Dong, J. Huang, and T. J. Savenije, “Charge Carrier Lifetimes Exceeding 15 μs in Methylammonium Lead Iodide Single Crystals,” *J. Phys. Chem. Lett.*, vol. 7, no. 5, pp. 923–928, Mar. 2016.
- [42] D. Sinram, C. Brendel, and B. Krebs, “Hexa-iodoanions of titanium, zirconium, hafnium, palladium and platinum: preparation, properties and crystal structures of the caesium



- salts," *Inorganica Chim. Acta*, vol. 64, pp. L131–L132, 1982.
- [43] E. Skoplaki, A. G. Boudouvis, and J. A. Palyvos, "A simple correlation for the operating temperature of photovoltaic modules of arbitrary mounting," *Sol. Energy Mater. Sol. Cells*, vol. 92, no. 11, pp. 1393–1402, Nov. 2008.
- [44] F. F. Targhi, Y. S. Jalili, and F. Kanjouri, "MAPbI<sub>3</sub> and FAPbI<sub>3</sub> perovskites as solar cells: Case study on structural, electrical and optical properties," *Results Phys.*, vol. 10, pp. 616–627, Sep. 2018.
- [45] H.-S. Kim *et al.*, "Lead Iodide Perovskite Sensitized All-Solid-State Submicron Thin Film Mesoscopic Solar Cell with Efficiency Exceeding 9%," *Sci. Rep.*, vol. 2, no. 1, p. 591, Dec. 2012.
- [46] "Optical properties and electronic structure of amorphous Ge and Si," *Mater. Res. Bull.*, vol. 3, no. 1, pp. 37–46, Jan. 1968.
- [47] B. D. H Brown *et al.*, "Crystal Structures," science Publishers, 1966.

# CURRICULUM VITAE

Dakota C. Schwartz, E.I.T., LEED GA

*Las Vegas, NV • dcschwar@gmail.com*

---

## EDUCATION

**University of Nevada Las Vegas, Las Vegas, NV**

M.S. Mechanical Engineering Candidate

Concentration: Fluid and thermo sciences

Research Area: Photovoltaic materials

Expected Graduation: May 2019

**California Polytechnic State University, San Luis Obispo, CA**

Mechanical Engineering, B.S., June 2017

## Academic Projects

**UNLV Center for Energy Research**

**Oct. 2017 – Present**

- Thesis project completed under the guidance of Dr. Shubhra Bansal
- Develop and test lead-free perovskite materials for photovoltaic use
- Two novel cesium platinum iodide materials synthesized and studied

**Cal Poly and PG&E, San Luis Obispo, CA**

**Sept. 2016 – June 2017**

- Senior design project team leader
- Researched, designed, and built a model self-leveling bubble curtain to replicate and improve the current design implemented in the intake bay of Diablo Canyon Power Plant (nuclear) in Avila Beach, California
- Funding provided by PG&E Diablo Canyon Power Plant

## Relevant Experience

**UNLV Department of Mechanical Engineering, Las Vegas, NV**

**August 2018 – Present**

- Graduate Assistant for the Department of mechanical engineering
- Instruct a Materials Mechanics laboratory (ME 302L) for undergraduate mechanical engineering students
- Grade for Structures and Properties of Solids (ME 301)

**NLine Energy, El Dorado Hills, CA**

**Summer 2015, March 2017 – September 2018**

- Junior Engineer (promoted from engineering intern July 2017)
- Complete engineering analysis of new hydropower technology
- Perform feasibility studies of undeveloped hydro sites using basic design principles and go/no-go criteria to determine energy generation, financial, environmental and regulatory permitting, and interconnection features of a project
- Research for state and federal small hydropower related DOE and CEC EPIC grant projects
- Analysis of past projects to determine the future small hydropower market

### **STEM Outreach and Participation**

**UNLV Louis Stokes Alliance for Minority Participation**

**October 2017 – Present**

- Graduate student mentor
- Mentor thirteen STEM undergraduates from historically underrepresented minority groups interested in STEM
- provide support toward degree completion and post-graduation goals

**UNLV Three Minute Thesis**

**November 2018**

- Semifinalist in UNLV's Three Minute Thesis (3MT) event
- Presented upon research topic in three minutes to a general audience

**UNLV Howard Hughes College of Engineering**

**March 2018**

- Graduate celebration participant
- Poster presentation for graduate students to share research topics

### **Skills and Qualifications**

- Engineer in Training (NCEES, June 2017)
- LEED GA (USBBC, June, 2017)
- Microsoft Office (proficient)
- Solidworks (familiar)
- Matlab (familiar)
- Design Builder, BEopt, SAM (familiar)

### **Conference Presentations**

*Exploration of Novel Wide Bandgap 2-d Pb-free Perovskite Materials for Photovoltaics: Cs<sub>2</sub>PtI<sub>6</sub>.* Oral presentation at 21st International Conference on Ternary and Multinary Compounds 2018 meeting in Boulder, Colorado. September, 2018.

*Bandgap Modulation in Cs-Pt-I-O Perovskites Based on Solvent Engineering.* Oral presentation at Materials Research Society Spring Meeting in Phoenix, Arizona. April 2019.